ISTANBUL TECHNICAL UNIVERSITY ★ GRADUATE SCHOOL OF SCIENCE ENGINEERING AND TECHNOLOGY

DIRECT AND INVERSE ELECTROMAGNETIC SCATTERING PROBLEMS IN SPHERICALLY LAYERED MEDIA

Ph.D. THESIS

Egemen BİLGİN

Department of Electronics and Communications Engineering

Telecommunications Engineering Program

MAY 2016

ISTANBUL TECHNICAL UNIVERSITY ★ GRADUATE SCHOOL OF SCIENCE ENGINEERING AND TECHNOLOGY

DIRECT AND INVERSE ELECTROMAGNETIC SCATTERING PROBLEMS IN SPHERICALLY LAYERED MEDIA

Ph.D. THESIS

Egemen BİLGİN
(504102301)

Department of Electronics and Communications Engineering

Telecommunications Engineering Program

Thesis Advisor: Prof. Dr. Ali YAPAR

MAY 2016

İSTANBUL TEKNİK ÜNİVERSİTESİ ★ FEN BİLİMLERİ ENSTİTÜSÜ

KÜRESEL TABAKALI CİSİMLERE İLİŞKİN DÜZ VE TERS SAÇILMA PROBLEMLERİ

DOKTORA TEZİ

Egemen BİLGİN
(504102301)

Elektronik ve Haberleşme Mühendisliği Anabilim Dalı

Telekomünikasyon Mühendisliği Programı

Tez Danışmanı: Prof. Dr. Ali YAPAR

MAYIS 2016

Egemen Bilgin, **a Ph.D.** student of ITU **Institute of Science Engineering and Technology** student ID 504102301, successfully defended the **thesis** entitled "**DIRECT AND INVERSE ELECTROMAGNETIC SCATTERING PROBLEMS IN SPHERICALLY LAYERED MEDIA**", which he prepared after fulfilling the requirements specified in the associated legislations, before the jury whose signatures are below.

Thesis Advisor :	**Prof. Dr. Ali YAPAR**	....
	İstanbul Technical University	
Jury Members :	**Prof. Dr. İbrahim AKDUMAN**	....
	İstanbul Technical University	
	Prof. Dr. Sedef KENT PINAR	....
	İstanbul Technical University	
	Prof. Dr. İrşadi AKSUN	....
	Koç University	
	Doç. Dr. Tanju YELKENCİ	....
	Marmara University	

Date of Submission : 08 April 2016
Date of Defense :   16 May 2016

FOREWORD

I would like to thank my supervisor Professor Ali Yapar for giving me valuable advice and support throughout my research and for his guidance in writing this thesis. I would also like to thank Professors İbrahim Akduman and Tanju Yelkenci for their encouragements and suggestions. I would like to express my gratitude to the Scientific and Technological Research Council of Turkey (TÜBİTAK) for their financial support. Finally, I want to thank my family for their constant support during the time I have studied.

May 2016   Egemen BİLGİN

TABLE OF CONTENTS

ABBREVIATIONS

MoM   **:** Method of Moments
MRI   **:** Magnetic Resonance Imaging
FFT   **:** Fast Fourier Transform
CSI   **:** Contrast Source Inversion
DGF   **:** Dyadic Green's Function
SVWF   **:** Spherical Vector Wave Functions
VSH   **:** Vector Spherical Harmonics

LIST OF FIGURES

xvi

DIRECT AND INVERSE SCATTERING PROBLEMS RELATED TO THE SPHERICALLY LAYERED MEDIA

SUMMARY

The direct and inverse scattering problems related to radially inhomogeneous spheres have interesting mathematical properties alongside practical value. In the direct scattering problem, the acoustic or elecromagnetic parameters of the spherical scatterer, which are arbitrary functions of the radial distance only, are assumed to be known; and the aim of the problem is to determine the scattered field in the whole space. On the other hand, for the inverse problem, these parameters constitute the unknowns of the problem, and they are determined through the value of the scattered field supposed to be measured on a measurement surface in the outside region. For the solution of the direct scattering problem, different techniques, with certain advantages and limitations, exist in the literature. The analytical techniques such as dyadic Green's function are only valid for certain types of profile, whereas numerical solution techniques such as method of moments have limited accuracy and they are in general computationally expansive. For the inverse problem, established methods such as Newton's method or the contrast source inversion technique can be applied directly to the three dimensional problem; however, the computational effort necessary for this type of procedure will put a limit to its practical value. Therefore, it can be concluded that the problems involving radially inhomogeneous spherical scatterer is still open to contributions.

In this thesis, a method to reduce the original three dimensional acoustic and electromagnetic problems into one dimensional forms has been developed. It has been demonstrated that such a method would be compatible with the available alternatives, and it will require less computational effort than the three dimensional solution techniques. It should be noted that although the orginal problem is a three dimensional one, the homogeneity along the angular direction enables one to replace it with one dimensional object and data equations involving only radial functions. For this dimension reduction procedure, the orthogonality of the spherical harmonics over the unit spherical surface have been used.

In the acoustic case, the scalar acoustic field has been expressed as a series expansion in terms of scalar spherical harmonics. Since those are functions of the angular terms, and the geometry is spherically symmetrical, their orthogonality is preserved within the original three dimensional object equation. Therefore, it is possible to eliminate the angular terms via orthogonality relation, and to obtain one dimensional reduced integral equations involving the coefficients of the series expansion for the acoustic field. For the solution of the direct scattering problem these coefficients can be determined by a simple discretization of the one dimensional integrals along the radial direction. On the other hand, a Newton based iterative scheme has been formulated for the solution of the inverse scattering problem. In this formulation, the one dimensional equations are solved using an initial guess for the unknown parameters, and the

coefficients of the measured scattered field constitute the data that is used to update the initial guess iteratively.

The procedure for the electromagnetic case is similar to the acoustic one. However, since the problem is a vectorial one in this case, the electric field is expanded in terms of vector spherical harmonics. These vectorial functions also satisfy the orthogonality condition over a spherical surface, therefore it is possible to reduce the vectorial electric field integral equation into a system of one dimensional integral equations. The integrals once again will only contain the scalar coefficients of the series expansion for the electric field, which are functions of the radial distance only. The resulting system of equations can be solved simultaneously to obtain the coefficients. The Newton based algorithm that was used in the acoustic case can be adapted to electromagnetic inverse problem in a straightforward manner. Therefore, same technique will be applied for the solution of the electromagnetic profile inversion problem.

The results of the numerical tests demonstrate that the method is quite reliable for determining the interior and scattered field in the case of acoustic or electromagnetic direct scattering problem. It is compatible with alternative methods, and it is computationally effective. Unlike analytical techniques which can only be used for piecewise homogeneous spheres, the method can be easily adapted to any kind of profile.Moreover, its accuracy is higher compared to the computationally more expansive numerical techniques. Therefore it is safe to assume that it can be used for practical applications involving complex scatterers such as head models. The acoustic or electromagnetic scattering problems involving radially inhomogeneous spheres are frequently encountered in the research fields such as biomedical engineering or material science. The method developed in this thesis can be reliably used in these problems.

For the inverse problem, the method yielded quite satisfactory results for slowly varying continuous profiles, provided that an appropriate initial guess is chosen. Other than the initial guess for the unknown acoustic or electromagnetic parameters, the most important point that effects the outcome of the method is the initial parameters of the iterative process itself. Through various numerical tests, the optimal values of these parameters have been determined and presented in the thesis. However, it was observed that even for these values, the success of the method is considerably lower for more rapidly varying profiles. Especially for layered profiles, the method can only provide a smoothed approximation. Numerical tests also demonstrated that the method produces useful results for relatively low contrast values. It should be noted that these are well-known limitations of Newton based algorithms, and the method performs reasonably well for an iterative profile inversion technique.

KÜRESEL TABAKALI CİSİMLERE İLİŞKİN DÜZ VE TERS SAÇILMA PROBLEMLERİ

ÖZET

Yarıçap doğrultusunda inhomojen küresel cisimlere ilişkin düz ve ters saçılma problemleri matematiksel açıdan ilgi çekici olmanın yanı sıra pratik açıdan da değer taşır. Düz saçılma problemlerinde cismin akustik ya da elektromanyetik parametrelerinin bilindiği kabul edilir. Bu parametreler sadece yarıçap doğrultusunda mesafenin fonksiyonudur. Problemin amacı kürenin dışındaki bölgede saçılan alanı hesaplamaktır. Öte yandan bu parametreler ters saçılma problemi için bilinmeyenleri oluşturur. Bunların belirlenmesinde kürenin dışında bir yüzeyde gerçekleştirilen saçılan alan ölçümlerinden yararlanılır. Düz problemin çözümünde farklı avantajları ve dezavantajları olan çeşitli teknikler geliştirilmiştir. Diyadik Green fonksiyonu gibi analitik teknikler sadece belirli profiller için kullanılabilmektedir, öte yandan moment metodu gibi nümerik tekniklerde başarı daha düşüktür ve işlem yükü gereksinimi de daha yüksektir. Ters saçılma probleminin çözümü için yaygın olarak kullanılan Newton metodu veya kontrast kaynak tekniği gibi metotlar doğrudan üç boyutlu probleme uygulanabilir. Ancak bu yaklaşımın gerektirdiği işlem yükü çok yüksek olduğundan pratikte uygulanabilirliği sınırlıdır. Sonuç olarak, küresel inhomojeniteye sahip cisimlere ilişkin saçılma problemlerinin hala yeni katkılara açık bir konu olduğu söylenebilir.

Bu tezde üç boyutlu akustik veya elektromanyetik problemi bir boyutlu bir forma indirgeyecek bir metot geliştirilmiştir. Yapılan testlerde görüldüğü üzere bu metot alternatif tekniklerle uyumludur ve üç boyutlu nümerik çözüm yöntemlerine göre daha az işlem yükü gerektirmektedir. Burada dikkat edilmesi gereken nokta üç boyutlu olarak formüle edilmiş olsa da problemin aslında bir boyutlu olduğudur. İnhomojenite sadece yarıçap doğrultusunda mevcut olduğundan problemin geometrisi açısal doğrultularda homojendir, ve bu bileşenler elimine edilebilir. Bu eliminasyon işleminin temel prensibi akustik ve elektromanyetik problem için aynıdır. Her iki problem için de amaçlanan, inhomojeniteden etkilenen yarıçap doğrultusundaki bileşenler ile homojen açısal bileşenlerin birbirlerinden ayrıştırılmasıdır. Bu ayrıştırma için akustik veya elektrik alanın küresel koordinat sisteminde birer seri toplamı şeklinde ifade edilmesi gerekmektedir. Bu seri toplamının baz fonksiyonları harmonik fonksiyonlardan oluşmaktadır. Bu fonksiyonlar alan büyüklüklerinin açısal bileşenlerini temsil etmek için kullanılmıştır. Seri toplamlarının skaler katsayıları ise sadece yarıçap doğrultusunun fonksiyonlarıdır. Bilindiği üzere küresel koordinat sisteminde harmonik fonksiyonlar birim küre yüzeyinde ortogonalite koşulunu sağlar. Problemin geometrisi açısal doğrultuda homojen olduğundan bu ortogonalite her zaman korunur. İşte bu ortogonalite bağıntısından yararlanılarak açısal terimler elenebilir. Dolayısıyla üç boyutlu cisim ve data denklemleri yerine, sadece yarıçap doğrultusunda değişen bileşenler içeren bir boyutlu integral denklemler oluşturulabilir. Bu temel prensip hem akustik hem de elektromanyetik problemin çözümünde kullanılabilir. Ancak problemlerin matematiksel yapıları farklı olduğundan

çözümlerinde kullanılacak seri toplamlarının da farklı yapıda olması gerekmektedir. Skaler yapıdaki akustik problem için skaler baz fonksiyonlar kullanılmıştır. Öte yandan elektromanyetik alanı temsil etmek için vektörel baz fonksiyonlarına ihtiyaç duyulmaktadır. Bu nedenle iki problem çözümleri farklı başlıklarda incelenmiştir.

Akustik problem için skaler alan küresel harmonikler cinsinden bir seri toplamı formunda ifade edilmiştir. Teseral harmonik olarak da adlandırılan bu fonksiyonlar Legendre fonksiyonları ve trigonometrik fonksiyonlardan oluşmaktadır. Dolayısıyla açısal bileşenlerin ifade edilmesinde kullanılabilirler ve küre yüzeyinde ortogonal olduklarından seri toplamı için baz fonksiyonu görevi görebilirler. Daha sonraki eliminasyon sürecinde küresel simetrik geometriden faydalanılarak üç boyutlu denklemde ortogonalite bağıntısı vasıtasıyla sadeleştirme gerçekleştirilebilir. Böylece ortogonalite aracılığıyla açısal terimler denklemden elenir ve bir boyutlu integral denklemler elde edilmiş olur. Bu fonksiyonlardaki tüm terimler yarıçap doğrultusundaki mesafenin fonksiyonlarıdır. Bunlardan en önemlisi elektrik alanı ifade eden serinin katsayılarıdır, ve bu katsayılar integral denklemi çözerek elde edilebilir. İntegral denklemin çözümü, bir boyutlu integrasyon domeninin eşit uzunlukta hücrelere ayrıştırılması ile gerçekleştirilir. Bu hücreler yeteri kadar küçük seçildiğinde interaldeki terimlerin hücre içindeki değişimi ihmal edilebilir seviyede kalır. Bu varsayım altında integral sadeleşir ve ayrıklaştırma ile integral denklem matris formuna çevrilir. Bu ayrıklaştırılmış sistemin çözümü hücre merkezlerindeki seri katsayılarını verir. Bu seri katsayıları elde edildikten kürenin içindeki toplam akustik alan en başta tanımlanmış seri toplamı kullanılarak elde edilebilir. Saçılan alanın hesaplanması da benzer bir yöntemle gerçekleştirilebilir. Saçılan alan için katsayılar, içerideki alan katsayıları ve indirgenmiş bir boyutlu integral ile doğrudan elde edilebilir.

Ters problemin çözümü için bu bir boyuta indirgenmiş denklemler kullanılabilir. Bu çalışmada alternatif çözüm tekniklerinden biri olan klasik Newton metodu kullanılmıştır. Newton metodunun en büyük dezavantajı her adımda düz problemin çözülmesinin getirdiği işlem yüküdür. Ancak burada kullanılan bir boyutlu denklemler düz problemin işlemsel yükünü oldukça azalttığından ters problemin çözümü için Newton temelli temelli iteratif bir algoritmanın kullanılması uygundur. Geliştirilen formülasyonda integral denklemler alan büyüklüğünün kendisi yerine seri toplamı katsayılarını içerdiğinden ters problemin de buna uygun olarak çözülmesi gerekir. Buna göre kürenin dışında ölçülen saçılan alan değerleri kullanılarak saçılan alan katsayıları elde edilir. Bu amaçla küresel harmonikleri içeren bir nümerik integrasyon işlemi gerçekleştirilir. Katsayılar elde edildikten sonra klasik Newton algoritması kullanılır. Bu algoritmada bilinmeyen cisim parametreleri için bir başlangıç değeri belirlenir ve bu değer kullanılarak düz problem çözülür. Bu çözüm ile elde edilen saçılan alan katsayıları ve ölçüm sonuçlarından elde edilen katsayıların karşılaştırılması ile başlangıç değeri güncellenir. Burada kullanılan denklemler kötü koşullanmış denklemler olduğundan bir regülarizasyon tekniğinin kullanılması gerekir. Bu çalışmada en sık kullanılan tekniklerden biri olan Tikhonov regülarizasyonu kullanılmıştır. Her adımda başlangıç değerinin güncellendiği bu iteratif süreç güncelleme terimi belli bir değerin altına düşünceye kadar sürdürülür. Elektromanyetik problem için çözüm akustik duruma benzer şekilde elde edilir. Ancak elektromanyetik alanlar vektörel olduğundan seri toplamı vektör küresel hamonikler kullanılarak tanımlanır. Bu vektörel baz fonksiyonları skaler harmonik fonksiyonlar aracılığıyla tanımlanır ve skaler eşdeğerlerine benzer şekilde küresel yüzeylerde ortogonalite bağıntısını sağlar. Bu seri toplamı için de katsayılar skalerdir ve sadece yarıçap doğrultusunun fonksiyonudur. Elektrik alan bu fonksiyonlar yardımıyla seriye

açılabilir. Benzer şekilde boş uzayın dyadik Green fonksiyonu da vektörel dalga fonksiyonları kullanılarak seri toplamı şeklinde ifade edilebilir. Vektörel dalga fonksiyonları açısal bileşenleri vektör küresel harmonikler, radyal bileşenleri ise küresel Bessel fonsiyonlarından oluşan küresel fonksiyonlardır. Bu fonksiyonlar homojen uzayda elektrik alanı temsil etmek için kullanılabilirler. Ancak burada kürenin içinde yarıçap doğrultusunda inhomojenite mevcut olduğundan elektrik alan vektör küresel harmonikler ile seriye açılmıştır. Böylece inhomojeniteden etkilenen radyal bileşen ile homojen açısal bileşenler birbirlerinden ayrışmış olur. Dyadik Green fonksiyonundaki vektörel dalga fonksiyonları ile elektrik alandaki vektör küresel harmoniklerin ortogonalliğinden faydalanılarak üç boyutlu vektörel integral denklemi bir boyutlu integral denklemler sistemine indirgemek mümkündür. Bu integraller de sadece yarıçap doğrultusunda değişen terimler içerdiğinden akustik duruma benzer bir çözüm elde edilmiş olur. Buradaki en temel fark akustik problemdeki tek denklemin yerini burada bir denklem sisteminin almasıdır. Elektrik alanın katsayıları bu denklem sisteminin çözülmesiyle bulunur ve buradan elektrik alanın gerçek ifadesine geçilebilir. Ters problem için akustik durumda kullanılan Newton temelli metodun elektromanyetik probleme de uygulanabileceği görülmüştür. Dolayısıyla aynı teknik hem akustik hem de elektromanyetik ters saçılma probleminin çözümünde kullanılacaktır.

Nümerik simülasyonlardan elde edilen sonuçlara göre bu tezde geliştirilen yöntem gerek akustik gerekse elektromanyetik düz saçılma problemlerinin çözümünde güvenle kullanılabilir. Sonuçlar yöntemin alternatifleriyle uyumlu ve işlem yükü bakımından daha verimli olduğunu göstermektedir. Sadece tabakalı cisimlerde kullanılabilen analitik tekniklerin aksine bu metot her türlü profilde uygulanabilmektedir. Tabakalı cisimlerde dyadik Green fonksiyonu ve analitik çözüm ile yapılan karşılaştırmalar seri toplamına yeterli sayıda terim eklendiğinde yöntemin yüksek bir doğruluğa sahip olduğunu göstermektedir. Sürekli bir fonksiyona sahip saçıcılarda karşılaştırma, moment metodu gibi nümerik tekniklerle yapılmıştır. Buradaki karşılaştrımalarda elde edilen sonuçlara göre yöntemin doğruluğu nümerik alternatiflere göre daha yüksektir. Daha önemlisi, tek boyuta indirgeme sayesinde üç boyutlu ayrıştırmaya dayalı moment metoduna göre verimlilik çok daha yüksektir. Dolayısıyla, kafa modelleri gibi daha karmaşık saçıcılar içeren pratik uygulamalarda burada geliştirilen yöntemin güvenle kullanılabileceği sonucuna varılabilir. Küresel yapılara ilişkin akustik ve elektromanyetik saçılma problemleri biyomedikal mühendisliği gibi araştırma alanlarında sıklıkla karşılaşılan problemlerdendir, ve burada geliştirilen metot rahatlıkla bu alanlarda kullanılabilir.

Ters saçılma problemlerinde yöntemin özellikle değişim hızı düşük, sürekli profiller için oldukça başarılı sonuçlar verdiği görülmüştür. Ancak bu başarı büyük ölçüde bilinmeyen parametreler için kullanılan başlangıç değerine bağlıdır. Başlangıç değeri ideal değerden saptığında yöntemin başarısı düşmektedir. Bunun dışında yöntemin regülarizasyon parametresi, sonlandırma eşiği, çalışma frekansı gibi diğer temel parametreleri de sonuca büyük oranda etki etmektedir. Newton metodunun bu standart parametreleri dışında burada geliştirilen yöntemde kullanılan seri toplamlarına eklenecek terim sayısı da performans üzerinde belirleyici etki yapmaktadır. Çeşitli simülasyonlar sonucu bu parametrelerin optimal değerleri tespit edilmiş ve tezin içerisinde belirtilmiştir. Bu incelemelerden görüleceği üzere cismin elektriksel boyutu belli bir sınırın üstüne çıktığında yöntem sonuç üretmekte zorlanmaktadır. Bu durum incelenecek cismin boyutlarına snırlama getirmektedir. Ayrıca optimal değerler kullanılsa da değişim hızı yüksek profiller için başarı oranının düşük kaldığı gözlemlenmiştir. Özellikle tabakalı cisimler için yöntem keskin geçişleri tespit

edemeyip ancak yumuşatılmış yaklaşık bir değer üretebilmektedir. Yöntemin bir diğer sıkıntısı da küre ile dış ortam parametreleri arasındaki kontrast değeri yükseldikçe sonuçlardaki hata oranının artmasıdır. Öte yandan bütün bu sayılanlar Newton temelli bir teknik için beklenebilecek eksikliklerdir, dolayısıyla yöntemin bu tarz bir iteratif tekniğe göre yeterli doğrulukta sonuçlar ürettiğini söylemek mümkündür. Burada geliştirilen indirgeme tekniğiyle elde edilen bir boyutlu denklemler farklı ters problem çözüm teknikleri ile çözülebilir. Bu şekilde Newton temelli yöntemlerin getirdiği kısıtlamalar aşılabilir.

1. INTRODUCTION

Inverse scattering problems aiming to determine the acoustical or electromagnetic parameters of a scatterer via the measurement of the scattered field is a major part of various research fields such as biomedical engineering, non-destructive material testing, or remote sensing. In these problems, the scatterer is illuminated by an incoming field, and the scattered field is measured on a domain outside the scatterer. The effect of the scattering object on the acoustic or electromagnetic field is analysed by using the related wave equation to model the incoming and scattered field [1]. The unknown parameters, which characterize the shape and the material of the scatterer, are obtained through one of the numerious solution techniques available in the literature for inverse problems [2]. The non-linearity of the wave equation causes the inverse problems to include non-linearity, and therefore all solution methods proposed in the literature involve a linearization technique.

One of the first application of the linear approximation is the Born approximation method, which provides an approximation of the unknown profile by substituting an initial guess for the acoustic or electromagnetic parameters into the integral equation involving the scattered field, namely the data equation [3]. While this approach is effective for the profiles having low contrast values, other methods are needed for most practical applications. To this end, iterative methods that can reconstruct profiles with relatively higher contrast values have been developed [4,5]. A widely used iterative procedure is the Newton-Kantorovich method, in which the direct scattering problem is solved in each step using the initial guess updated in the previous step [6-8]. The need to solve the direct scattering problem in each update considerably increases the computational effort, especially for 2-D and 3-D problems. The contrast source inversion method, a modified gradient method, has been developed in order to remove that requirement [9,10].

The brief review of the inversion techniques presented above, demonstrates that all the methods involves the solution of the related direct scattering problem. In addition, for most applications, the scattering field, used as data in the inverse problem, is produced

synthetically, therefore the related direct scattering problem must be solved before the inverse problem. The aim of the direct scattering problems is to determine the field scattered by an object, whose shape and material parameters are known. For the case of an arbitrarily shaped scatterer, one of the most commonly employed method is the method of moments [11-13]. In [14], the electric field scattered by a 3-D dielectric object is calculated by a discretization of the scatterer into cubic cells, and the evaluation of the interior electric field using point matching technique. This approach can also be adapted to the acoustic scattering problem in a straightforward manner. However, for electrically large, inhomogeneous 3-D scatterers, MoM becomes computationally intensive. Hybrid methods, combining MoM with finite element method, which is more suitable for handling inhomogeneities, are proposed to reduce computational time [15,16]. Another frequently used approach to create a computationally effective numerical technique is to employ conjugate gradient method combined with fast Fourier transform to solve linear equations obtained via MoM discretization.

The techniques for inverse and direct problems mentioned above can be used for different type of geometries. For each problem, the form of the equations and the parameters vary according to the specific geometrical configuration. Therefore, choosing an appropriate method and adapting it to the problem at hand is of crucial importance for the solution of the inverse problem. Especially for canonical structures such as cylindirical or spherical objects, special solutions might be formulated by taking advantage of the wave form in that geometry. These special solutions are in general obtained by modifying the equations of the direct and inverse scattering techniques via analytical or semi-analytical methods available for the related canonical structures. The details and the advantages of this approach will be presented in the subsequent sections. The emphasis will be on the geometries with spherical symmetry, since the main contribution of this work is the development of novel techniques for the solution of the direct and inverse scattering problems related to radially inhomogeneous spherical objects.

1.1 Purpose of Thesis

The direct and inverse scattering problems involving canonical structures have been the subject of numerious publications for their theoretical features, and their usage in

various practical engineering applications. One of the main source of interest is that for the most problems, the computationally intensive numerical methods cited above can be replaced by semi-analytical methods. For practical applications, these objects can be used as models for scatterers that are more complex. Radially inhomogeneous spherical scatterers constitute an especially important research topic for this matter. In various works on medical imaging, the human head is modeled as a layered sphere [17-20]. This approach has been successfully used in the studies on human head interaction with electromagnetic sources, MRI, impedance tomography, microwave imaging, and electroencephalography [21-27]. On the other hand, radially inhomogeneous spheres with continuous profiles are used in the design of dielectric lenses and metamaterials [28-32]. From these examples, it can be concluded that direct and inverse problems related to radially inhomogeneous spheres have great value for practical applications.

Therefore, in this thesis, novel techniques have been developed in order to solve direct and inverse scattering problems for the radially inhomogeneous spheres. In the first part, the acoustical problem has been investigated. The sphere is assumed to have arbitrarily varying compressibility along the radial direction only. The purpose of the direct scattering problem is to determine the scattered acoustic field outside the sphere, in the case of a time harmonic point source or plane wave excitation. By taking advantage of the spherically symmetrical geometry, and the structure of the integral equations; one can replace the 3-D problem with a 1-D formulation, and therefore greatly reduce the time consuming complexity of the original problem. The solution of the related inverse scattering problem is based on the 1-D integral equation formulation used in the direct scattering problem. This 1-D integral equation is solved in an iterative fashion via the Newton method. The Newton method is especially suitable for the 1-D profile inversion problem since the computational complexity caused by the need to solve the direct scattering problem in each step is significantly lower compared to the original 3-D structure.

The analysis of the electromagnetic case follows the same plan. First, the direct scattering problem involving a dielectric sphere with a permittivity and conductivity varying in the radial direction only, has been solved in a similar fashion. However, since for the electromagnetic case the field function is vectorial, obtaining the 1-D formulation is much more challenging compared to the acoustic case. For the solution

of this problem, the spherical vector wave functions, which are the solution of the vector wave equation in the spherical coordinates, have been used to obtain a system of a 1-D integral equations. The inverse problem has been solved similarly via Newton method using this system of integral equations. Finally, for both acoustic and electromagnetic cases, the accuracy and the performance of the method have been tested via numerical simuations.

In conclusion, it can be stated that the main purpose of the thesis is, first, to formulate an efficient semi-analytical method that can be used in the solution of direct scattering problems for the radially inhomogeneous geometry; and second, to transform the related 3-D inverse problem into a 1-D profile inversion problem using the same formulation. The solution of the resulting 1-D inversion problem will then be obtained via a classical technique such as the Newton method.

1.2 Literature Review

Numerous publications on the direct scattering problems related to the spherical scatterers can be found in the literature. For the acoustic case, a formulation based on the integro-differential equation for the field scattered by 3-D inhomogeneous objects has been given in [33]. The effect of variable density, which is an important factor for acoustic scattering formulations, has been analysed in this work, and it has been concluded that the problem cannot be reduced to a classical Schwinger-Lippmann integral equation in the case of variable density. Because of this condition, most of solutions proposed for the acoustic scattering problems involve scatterers with constant density. Similarly, in this thesis, the spherical scatterer is assumed to have only variable compressibility along the radial direction. An FFT based adaptive integral method has been developed for large inhomogeneous scatterers in [34]. In this work the formulation is once again is based on 3-D integral equations. A method to reduce the scalar wave equation into a 1-D form by the use of scalar harmonics and the Dini series has been presented in [35]. The solution is obtained under the assumption of constant density throughout the whole space. It has been shown in this work that the acoustic field can be expressed as series expansion in terms of spherical harmonics, and a 1-D formulation can be obtained by using the orthogonality of these functions. The mathematical properties of the spherical harmonics and the scalar wave function can be found in [36]. The extension of the solution presented in [35] to the

4

case of inhomogeneous density in given in [37]. Another important tool for the direct scattering problem related to the canonical structures are Green's functions related to the particular geometry. For spherical scatterers, the Green's function of the scalar wave equation for the radially inhomogeneous sphere has been obtained in [38]. In this work the closed form expressions are obtained for special compressibility functions such as Nomura-Takaku distributions. On the other hand, the closed form of the Green's function for linearly inhomogeneous medium is given in [39]. It is clear from this analysis that the different solutions for the direct scattering problem for radially inhomogeneous spheres is available in the literature. In this thesis, a novel formulation, which is easy to implement, and more suitable to be applied in the inverse scattering problems, will be developed.

The number of works on the subject of acoustic inverse scattering problem for the inhomogeneous spheres is much more limited compared to the direct scattering case. For the planarly stratified media, a method to reconstruct the density profile has been presented in [40]. In this work, the solution is obtained using the classical Born approximation. Similarly, in [41], the 1-D inverse scattering problem for a radially inhomogeneous sphere has been solved in order to reconstruct the density profile. The solution is obtained using Gelfand-Levitan method for the equations of Born approximation. In [42], the method of near field acoustical tomography has been applied in order to reconstruct the 3-D acoustical parameters. On the other hand, in [43], the CSI method has been used to determine the variation of the density and compressibility within a 3-D scatterer. A general review of the techniques used in the acoustic inverse scattering problems can be found in [44]. Considering the limitation of the Born approximation regarding the contrast values, it can be concluded that the 1-D profile inversion problem related to the radially inhomogeneous spheres is still open to contributions. It should be noted that the 3-D solutions require an unnecessary computational effort, which can be avoided by transforming the problem into a 1-D form. Therefore, the main goal of the thesis regarding the acoustic case is to obtain an effective inversion scheme base on the solution of the related direct scattering problem.

For the electromagnetic direct scattering problem related to radially inhomogeneous sphere, various analytical or semi-analytical methods are available in the literature for the solution of the problem. In the case of piecewise homogeneous layered spheres, the dyadic Green's function constitute a powerful technique that can be used in order

to obtain the scattered or interior electric field [45]. These functions are constructed as series expansions in terms of spherical vector wave functions, and the coefficients of these expansions are obtained using the boundary conditions. Construction of the dyadic Green's functions for the chiral or bianisotropic media can also be found in the literature [46,47]. On the other hand, as it is demonstrated in [48], the construction of the dyadic Green's function for the spheres with continuously varying radial profile is much more challenging. In [49], for continuous profiles, two differential equations have been formulated to determine the radial component of the electric field. However, only for a few special profiles, these differential equations can be solved analytically. Therefore, for most of the cases, numerical differentiation techniques must be employed to supplement the analytical method. In addition, as these differential equations involve the derivative of the electromagnetic parameters, the method developed in [48,49] can only be applied for the differentiable profiles. Therefore, a method that can be used for the spheres with arbitrarily varying profiles cannot be based on dyadic Green's functions. On the other hand, different semi-analytical methods using similar series expansions is available in the literature. In [50], a method based on the expension of the scalar free-space Green's function in terms of spherical vector wave functions is presented. Similar to the acoustic case, this expansion is combined with a radial expansion in terms of the Dini series. As stated above, the spherical vector wave functions are the solution of the vector wave equation in the spherical coordinate system, and they are orthogonal over the unit spherical surface [51-53]. In this thesis, these functions and their angular parts, the vector spherical harmonics, have been used to formulate a 1-D integral equation system for the solution of the electromagnetic direct scattering problem. The detailed mathematical analysis of the vector spherical harmonics can be found in [54].

For the 1-D electromagnetic profile inversion problems, different techniques have been used to reconstruct 1-D variation of the profile. Especially for planar and cylindrical profiles, various works can be found in the literature. For the planar profiles, the Riccati type differential equation has been used to develop an analytical reconstruction technique [55,56]. However, this technique cannot be adapted to the other corrdinate systems in a straightforward manner [57]. Therefore as an alternative, Born approximation has been used for stratified cylindrical medium in [58]. As expected for a method based on Born approximation, the solution is valid only for low

contrast values. For relatively higher contrast values, solutions based on renormalized source type integral equation approach, and distorted Born approximation have been developed for cylindrical medium [59,60]. Finally, a more effective approach based on iterative Newton method is presented in [61], to reconstruct an arbitrarily varying radial profile. Publications related to spherical profile inversion are less numerous in the literature. A technique based on the inversion of the Riccati-similar non-linear differential equations has been developed in [62], in order to reconstruct continuously varying radial profile. On the other hand, a method to determine the electromagnetic parameters and the radii of a layered sphere has been proposed in [63]. Therefore, it can be concluded that the inverse problem involving the reconstruction of arbitrarily varying spherical profile is still open to contribution. In this thesis, a Newton type method based on the 1-D integral equation system has been developed in order to reconstruct moderately high contrast values.

1.3 Hypothesis and Main Contributions

Considering the analysis presented in the previous sections, the hypothesis of this thesis can be stated as follows: The 3-D direct and inverse scattering problems related to the radially inhomogeneous spheres can be transformed into a 1-D form by taking advantage of the spherical symmetry, and using appropriate series expansions for the interior and scattered field. Through this 1-D equation system, efficient techniques for the solution of direct and inverse problems might be formulated. Although this approach can be applied to both acoustic and electromagnetic problems, the process of dimension reduction must be different for the two cases, considering the mathematical structures of related wave equations. Therefore, in this thesis, the acoustic and the electromagnetic problems will be analysed separately. However, it should be noted that the general principles of the solutions for both cases are of similar nature.

For the scalar acoustic case, the direct scattering problem involve determining the scalar scattered field in the presence of the time harmonic point source excitation. The problem is originally formulated by the use of the 3-D integral equation. The density is considered constant throughout the whole space, and the compressibility of the sphere is assumed to vary along the radial direction only. Although it limits the practical value of the method, the assumption of the constant density is a necessary condition for the goal of dimension reduction. It can be shown that the 3-D integral

equation can be reduced to a 1-D form by expressing the angular dependency of the field quantities in terms of the spherical harmonics. The orthogonality of the spherical harmonics over the unit spherical surface enables one to form a series expansion for any function that is integrable over the spherical domain. Note that as a result of the spherical symmetry, the orthogonality of the spherical harmonics is preserved throughout the entire space. Therefore, the resulting system constitutes of 1-D integral equations containing the series coefficients of the field quantities and the acoustical profile. This system is solved via a simple discretization of the integration domain along the radial direction to determine the coefficients for the scattered field, and then the scattered field itself. The performance of the method is tested by comparing the results with alternative techniques such Green's function for the layered spheres, and the MoM for continuous profiles. These numerical simulations demonstrate that the method is suitable for various profiles, and can also be used in the inverse scattering problems reliably.

For the formulation of the acoustic inverse problem, same 1-D reduced integral equations will be used. Note that since the acoustical profile is a function of the radial distance only, it is not effected by this reduction, and remains unchanged throughout the entire formulation. The two integral eqautions can be named as the reduced object and the reduced data equations. For the inverse problem the acoustical profile is the unknown, the aim is to reconstruct this function via measurement of the scattered field outside the sphere. The coefficients of the measured scattered field constitute the data of the inverse problem. The resulting inverse problem is solved in an iterative fashion via Newton method, by starting from an initial estimate of the acoustical profile. In each step of the iteration, the coefficients of the interior field is updated using the object equation. Since this step is similar to the direct scattering problem, it is a well-posed problem. However, the update of the object function via the data equation is severely ill-posed, and the inversion can be achieved via a regularization technique. In this work, the well-known Tikhonov regularization has been employed to obtain a stable update amount for the acoustical profile [64]. The proposed method has ben tested using various continuous and layered profiles. The results show that the method is capable of reconstructing continuous and layered profiles, provided that an appropriate initial guess is chosen for the unknown profile.

The electromagnetic direct scattering problem is similarly formulated by the 3-D electric field integral equation involving the free space dyadic Green's function. The interior electric field and the scattered field are then expanded in terms of the vector spherical harmonics, which form the angular components of the vector wave functions, and therefore, are also orthogonal over unit spherical surface [54]. The main reason to choose these functions as basis for series expansion is to separate angular parts from the radial one, which is affected by the inhomogeneity. On the other hand, the free space dyadic Green's function is expanded in terms of the vector wave functions [53]. By substituting these expansions into to 3-D integral equation, and using the orthogonality of the basis functions, one can obtain a system of 1-D integral equations containing only radial functions. These integral equations are well-posed, and the kernels of the integrals are smooth functions. Therefore, similar to the acoustic case they can be solved via a discretization along the radial direction. The solution of this sytem provides the coefficients of the interior electric field. The scattered field can be obtained in a similar fashion by transforming the related integral equation outside the sphere. The dimension reduction greatly reduce the computational complexity of the original problem. The comparison of the method with 3-D alternatives such as MoM demonstrates that the method provides higher accuracy and efficiency for the solution of scattering problems related to the radially inhomogeneous spheres. Also the mathematical structure of the 1-D integral equations makes the method suitable for various applications including inverse scattering problems.

It should be noted that the main advantage of the formulation developed in this thesis compared to the existing 1-D formulations given in [49,50] lies in the fact that the electromagnetic parameters remain unaffected from the reduction process. The 1-D integral equations have the same form for any type of profiles, and they do not contain any differential operator applied on the electromagnetic parameters. Furthermore, the series expansion do not involve any of the electromagnetic parameters. Therefore, the method is especially suitable for the inverse scattering problems. The reduced 1-D integral equations once again constitute the reduced object and data equations. Similar to the acoustic case, the inverse problem is solved via iterative Newton method. First, using the initial guess for the profile, the system designated as the reduced object equations is solved to obtain the coefficients of the approximate interior electric field. For 3-D problems, this step is the most computationally intensive part of the iterative

process; however, the necessary computational effort is significantly decreased through the dimension reduction. Hence, the Newton method is especially suitable for the 1-D profile inversion problems. In the next step, the non-linear data equations, which involves the coefficients of the series expansion instead of the scattered field itself, are linearized. As the linearized data equations contain compact operators, they are ill-posed. Therefore, they are solved using the Tikhonov regularization to update the unknown profile. The numerical simulations demonstrate that the method can be effectively used in the reconstruction of the continuous profiles, and although it fails to detect sharp transitions, still provides an approximation for the piecewise homogeneous layered profiles. However, as expected for a Newton based method, the success clearly depends on the choice of initial parameters.

2. ACOUSTIC CASE

2.1 Purpose

In this section, the acoustic direct and inverse scattering problem related to radially inhomogeneous spheres will be analysed. First, the direct scattering problem will be solved through a dimension reduction process. The main goal of this process, as stated before, is to obtain 1-D integral equations instead of the original 3-D formulation of the problem. To this end, the orthogonality properties of the spherical harmonics will be used. In the second part, the solution of the related inverse problem will be developed using the aforementioned reduced 1-D integral equations. For the inversion process the classical Newton algorithm will be used, that is an iterative process, starting by an initial guess, will reconstruct the unknown acoustic profile. The content of this section has been presented in a more compact form in [65]. Here, the formulation of the method will be demonstrated in a more detailed manner. A time dependence $e^{-i\omega t}$ is assumed and omitted throughout the entire section.

2.2 Direct Scattering Problem

In this sub-section, we will first present a brief analysis of the spherical harmonics. The dimension reduction process is based on the mathematical properties of these functions, and therefore a theoretical background should be presented before the demonstration of the formulation. The second part will be the main body of this sub-section, and will include the formulation of the problem. After the scattering problem is first formulated, the dimension reduction process will be developed using the spherical harmonics. Via this reduction process, one can replace the 3-D integral equation with reduced 1-D integral equations by expressing the interior and scattered field in terms of the appropriate spherical harmonic function. The solution of the direct scattering problem will be obtained using these integral equations. Finally, in the third part, the success of the method developed in the previous section will be tested via numerical simulations. The results will be compared with alternative methods such as

Green's function or MoM. Furthermore, through these simulations, the effects of the essential parameters of the method, such as truncation number for series expansions, will be analysed.

2.2.1 Spherical harmonics

In this sub-section, the basis functions that will be used in the series expansions for the field values will be introduced. These functions compose the solution of the scalar Helmholtz equation in the spherical coordinate system. Therefore in the first part, the expression of the wave functions in the spherical coordinates will be given. In the next part, the orthogonality of these spherical functions will be demonstrated. The orthogonality of these functions enables one to form series expansions over the unit spherical surface. The mathematical properties of the series expansions will also be presented in the same sub-section. Finally, in the last part, some wave transformations that will be needed in the subsequent sections will be presented. The mathematical demonstration of this sub-section summarizes the detailed analysis given in [36] with a slightly modified notation.

2.2.1.1 The wave functions

The scalar Helmholtz equation is written in the spherical coordinates as:

$$\frac{1}{r^2}\frac{\partial}{\partial r}\left(r^2\frac{\partial\psi}{\partial r}\right) + \frac{1}{r^2\sin\theta}\frac{\partial}{\partial\theta}\left(\sin\theta\frac{\partial\psi}{\partial\theta}\right) + \frac{1}{r^2\sin^2\theta}\frac{\partial^2\psi}{\partial\phi^2} + k^2\psi = 0 \tag{2.1}$$

Typically the solution of (2.1) is obtained via the method of seperation of variables. Therefore, the wave function is expressed in terms of elementary functions:

$$\psi = R(r)H(\theta)\Phi(\phi) \tag{2.2}$$

By substituting this expression into (2.1), and proceeding with the seperation procedure, one can obtain three seperated equations for the variables.

$$\frac{d}{dr}\left(r^2\frac{\partial R}{\partial r}\right) + \left[k^2r^2 - n(n+1)\right]R = 0 \tag{2.3}$$

$$\frac{1}{\sin\theta}\frac{\partial}{\partial\theta}\left(\sin\theta\frac{\partial H}{\partial\theta}\right)+\left[n(n+1)-\frac{m^2}{\sin^2\theta}\right]H=0 \tag{2.4}$$

$$\frac{d^2\Phi}{d\phi^2}+m^2\Phi=0 \tag{2.5}$$

The solutions of (2.3) are called spherical Bessel functions, and they are defined in terms of the ordinary Bessel functions as

$$b_n(kr)=\sqrt{\frac{\pi}{2kr}}B_{n+\frac{1}{2}}(kr) \tag{2.6}$$

To represent a field inside the sphere, the functions $j_n(kr)$ must be used because this is the only spherical Bessel function which is finite at $r=0$. On the other hand, the spherical Hankel functions of the first kind $h_n^{(1)}(kr)$ must be used to represent an outward travelling field to satisfy radiation condition for $r\rightarrow\infty$.

The solutions of (2.4) are the associated Legendre functions $P_n^m(\cos\theta)$ and $Q_n^m(\cos\theta)$ Since all other associated Legendre functions have singularities at $\theta=0$ and $\theta=\pi$; in order to have a finite wave function on the interval $\theta\in[0,\pi]$, the functions $P_n^m(\cos\theta)$, with n being an integer, must be used in the final form of ψ. Finally, (2.5) is the well known harmonic equation, and the solution will be expressed in this thesis as a linear combination of $e^{im\phi}$ and $e^{-im\phi}$, with m being an integer.

Therefore, the final form of the wave functions that can be used in the representation of the scalar fields in the spherical coordinates can now be written. For the fields inside the spheres including the origin, the elementary wave function is given as

$$\psi_{nm}=j_n(kr)P_n^m(\cos\theta)e^{im\phi} \tag{2.7}$$

whereas for outward travelling waves the proper form is

$$\psi_{nm}=h_n^{(1)}(kr)P_n^m(\cos\theta)e^{im\phi} \tag{2.8}$$

Here, m and n are integers. Therefore, the general solution of the Helmholtz equation in the spherical coordinates system can be written as a linear combination of the elementary wave functions as

$$\psi = \sum_n \sum_m C_{nm} \psi_{nm} \qquad (2.9)$$

with C_{nm} being scalar constants. The expressions presented in (2.7) and (2.8) demonstrate that the angular components of any scalar field in a spherically symmetrical geometry can be expressed as a series expansion in terms of the functions $P_n^m(\cos\theta)$ and $e^{\pm im\phi}$, which will be the subject of the next sub-section.

2.2.1.2 The orthogonality relationships

In this sub-section, we will first state the orthogonality relationship regarding the associated Legendre functions and the harmonic functions. The proof of these relationships can be found in [36]. Then we will define the form of the series expansion that will be used in the dimension reduction procedure. The proof of these relationships can be found in [36].

First, the harmonic functions $e^{\pm im\phi}$ satisfy the well known orthogonality relationship on the domain $\phi \in [0, 2\pi]$:

$$\int_0^{2\pi} e^{im\phi} \cdot e^{in\phi} \, d\phi = \begin{cases} 0 & m \neq -n \\ 2\pi & m = -n \end{cases} \qquad (2.10)$$

Similar to the harmonic functions, the Legendre polynomials form an orthogonal set in the interval $\theta \in [0, \pi]$. The orthogonality relationship for these polynomials are given as

$$\int_0^{\pi} P_n(\cos\theta) \cdot P_l(\cos\theta) \sin\theta d\theta = \begin{cases} 0 & n \neq l \\ \dfrac{2}{2n+1} & n = l \end{cases} \qquad (2.11)$$

Finally, to form a complete orthogonal set over the unit spherical surface a combination of associated Legendre functions and the harmonic functions must be used. First, let us state the orthogonality relationship for the Legendre functions:

$$\int_0^\pi P_n^m(\cos\theta) \cdot P_p^q(\cos\theta)\sin\theta d\theta = \begin{cases} 0 & n,m \neq p,q \\ \dfrac{2}{2n+1}\dfrac{(n+m)!}{(n-m)!} & n,m = p,q \end{cases} \tag{2.12}$$

The combination $P_n^{|m|}(\cos\theta)e^{\pm im\phi}$ are called spherical harmonics or tesseral harmonics, and the related orthogonality relationship can be determined by combining (2.10) and (2.12) as

$$\int_0^{2\pi}\int_0^\pi P_n^{|m|}(\cos\theta) P_p^{|q|}(\cos\theta) e^{im\phi} e^{iq\phi}\sin\theta\, d\theta d\phi = \begin{cases} 0 & n,m \neq p,-q \\ \dfrac{4\pi}{2n+1}\dfrac{(n+|m|)!}{(n-|m|)!} & n,m = p,-q \end{cases} \tag{2.13}$$

It is clear from (2.13) that any function $f(\theta,\phi)$ that is integrable over the domain $[0,\pi]\times[0,2\pi]$ can be expressed as a series expansion in terms of spherical harmonics as

$$f(\theta,\phi) = \sum_{n=0}^{\infty}\sum_{m=-n}^{n}\hat{f}_{nm}\frac{2n+1}{4\pi}\frac{(n-|m|)!}{(n+|m|)!}P_n^{|m|}(\cos\theta)e^{im\phi} \tag{2.14}$$

Here, $\hat{f}_{nm}$ are the scalar coefficients of the series expansion. These coefficients can be determined using the orthogonality relationship (2.13). By multiplying both side with $P_p^{|q|}(\cos\theta)e^{iq\phi}$, and integrating over the unit spherical surface, one obtains

$$\hat{f}_{nm} = \int_0^{2\pi}\int_0^\pi f(\theta,\phi) P_n^{|m|}(\cos\theta) e^{-im\phi}\sin\theta\, d\theta d\phi \tag{2.15}$$

The series expansion defined by (2.14) and (2.15) can be used to express the angular dependence of the scalar fields in the spherical coordinate system.

2.2.1.3 The wave transformations

In this sub-section, we will first obtain the acoustic plane wave as a series expansion in terms of the spherical wave functions. This expression will be used as an alternative for the point source excitation. Secondly, a similar expansion for the acoustic field created by a point source will be presented. The addition theorem for the spherical

15

Hankel functions will also be derived through the procedure. This theorem constitutes an important part of the dimension reduction process. The more detailed presentation of the derivation procedures can be found in [36].

First, for the acoustic plane wave travelling in the negative z direction, expressed as e^{-ikz}, the series expansion have the form

$$e^{-ikz} = e^{-ikr\cos\theta} = \sum_{n=0}^{\infty} a_n j_n(kr) P_n(\cos\theta)$$

(2.16)

Here, a_n are scalar coefficients of the series expansion. The radial dependence should be expressed in terms of spherical Bessel functions $j_n(kr)$ to avoid having singularity at $r = 0$. Moreover, since the plain wave is independent of ϕ, the harmonic functions are excluded from the series expansion. To obtain the coefficients a_n, both sides of the (2.15) is multiplied by $P_q(\cos\theta)$, and integrated over the interval $\theta \in [0, \pi]$. Then considering the orthogonality relationship given in (2.11), we obtain

$$\int_0^{\pi} e^{-ikr\cos\theta} P_n(\cos\theta) \sin\theta \, d\theta = \frac{2a_n}{2n+1} j_n(kr)$$

(2.17)

By evaluating this integral, the coefficients are determined as

$$a_n = (-i)^n (2n+1)$$

(2.18)

Substituting this expression into (2.16) yields the series expansion for the acoustic plane wave travelling in the negative z direction:

$$e^{-ikz} = \sum_{n=0}^{\infty} (-i)^n (2n+1) j_n(kr) P_n(\cos\theta)$$

(2.19)

Secondly, the series expansion for the field created by a point source located at $\mathbf{r}_s$, defined as

$$\frac{e^{ik|\mathbf{r}-\mathbf{r}_s|}}{ik|\mathbf{r}-\mathbf{r}_s|}$$

(2.20)

16
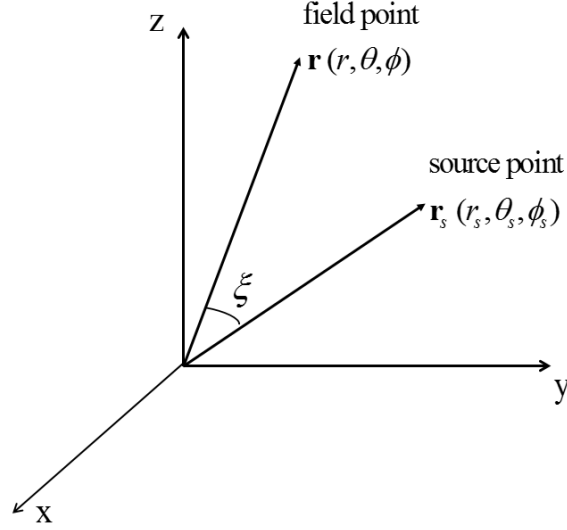
Figure 2.1 : The source and the field points in the spherical coordinates.

will be expanded in terms of the spherical wave functions. Considering the asymptotic formula for the spherical Hankel functions

$$h_n^{(1)}(kr) = \frac{(-i)^{n+1}}{kr} e^{ikr} \tag{2.21}$$

it is clear that the field given by (2.20) can also be expressed via spherical Hankel functions as

$$\frac{e^{ik|\mathbf{r}-\mathbf{r}_s|}}{ik|\mathbf{r}-\mathbf{r}_s|} = h_0^{(1)}(k|\mathbf{r}-\mathbf{r}_s|) \tag{2.22}$$

Now, consider the geometry given in Fig. 2.1. Since the field created by the point source is symmetric around the vector $\mathbf{r}_s$, the angular wave functions, the Legendre polynomials, can be expressed in terms of the angle ξ which is defined as

$$\cos\xi = \cos\theta\cos\theta_s + \sin\theta\sin\theta_s\cos(\phi - \phi_s) \tag{2.23}$$

To avoid singularity at $r = 0$, and to satisfy the radiation condition for $r \to \infty$, the radial dependence for the series expansion should be of the form $j_n(kr)h_n^{(1)}(kr_s)$ for $r < r_s$, and $j_n(kr_s)h_n^{(1)}(kr)$ for $r > r_s$. The angular dependence will be expressed by the Legendre polynomials. Therefore, the expansion have the form

$$
h_0^{(1)}(k|\mathbf{r}-\mathbf{r}_s|) =
\begin{cases}
\displaystyle\sum_{n=0}^{\infty} C_n h_n^{(1)}(kr_s) j_n(kr) P_n(\cos\xi) & r < r_s \\[3mm]
\displaystyle\sum_{n=0}^{\infty} C_n h_n^{(1)}(kr) j_n(kr_s) P_n(\cos\xi) & r > r_s
\end{cases}
\tag{2.24}
$$

Here, C_n are the scalar coefficients. By receding the source to infinity, the field can be made equivalent to a plane wave. Therefore, replacing the spherical Hankel functions by the asymptotic formula (2.21), and comparing the resulting expression with (2.19) yields the coefficients as determined as

$$
C_n = 2n+1
\tag{2.25}
$$

Finally, the Legendre polynomials $P_n(\cos\xi)$ can be expressed in terms spherical harmonics $P_n^m(\cos\theta)e^{\pm im\phi}$ as

$$
P_n(\cos\xi) = \sum_{m=-n}^{n} \frac{(n-|m|)!}{(n+|m|)!} P_n^{|m|}(\cos\theta) P_n^{|m|}(\cos\theta_s) e^{im(\phi-\phi_s)}
\tag{2.26}
$$

The final form of the addition theorem for the spherical Hankel functions is obtained by substituting (2.25) and (2.26) into (2.24):

$$
h_0^{(1)}(k|\mathbf{r}-\mathbf{r}_s|) =
\begin{cases}
\displaystyle\sum_{n=0}^{\infty} \sum_{m=-n}^{n} \frac{(2n+1)(n-|m|)!}{(n+|m|)!} h_n^{(1)}(kr_s) j_n(kr) \\[3mm]
\displaystyle\sum_{n=0}^{\infty} \sum_{m=-n}^{n} \frac{(2n+1)(n-|m|)!}{(n+|m|)!} h_n^{(1)}(kr) j_n(kr_s)
\end{cases}
\tag{2.27}
$$

$$
\times P_n^{|m|}(\cos\theta) P_n^{|m|}(\cos\theta_s) e^{im(\phi-\phi_s)} \qquad r < r_s
$$
$$
\times P_n^{|m|}(\cos\theta) P_n^{|m|}(\cos\theta_s) e^{im(\phi-\phi_s)} \qquad r > r_s
$$

2.2.2 Solution of the direct scattering problem

In the first part of this sub-section, the general formulation of the direct scattering problem will be presented. After the introduction of the acoustic wave equation in the original form, the necessary simplifications will be stated. After the formulation, in the second part, the dimension reduction process will be explained in detail. The 3-D integral equation, introduced in the first part, will be reduced to a 1-D integral equation

18

along the radial direction. The solution of the direct scattering problem is obtained by a simple discretization of these reduced integral equations.

2.2.2.1 Formulation of the problem

Consider the sphere with radius a, denoted by D in Fig. 2.2, whose acoustic parameters, the density $\rho(r)$ and the compressibility $b(r)$, are functions of radial distance r only. The sphere is illuminated by a time harmonic point source of strength P_0, situated at the point (r_s, θ_s, ϕ_s), $r_s > a$. The region outside the sphere is characterized by a constant wave number $k_0 = \omega\sqrt{\rho_0 b_0}$, ρ_0 and b_0 being the density and the compressibility of the outside region respectively. Here, ω is the operating angular frequency of the point source.
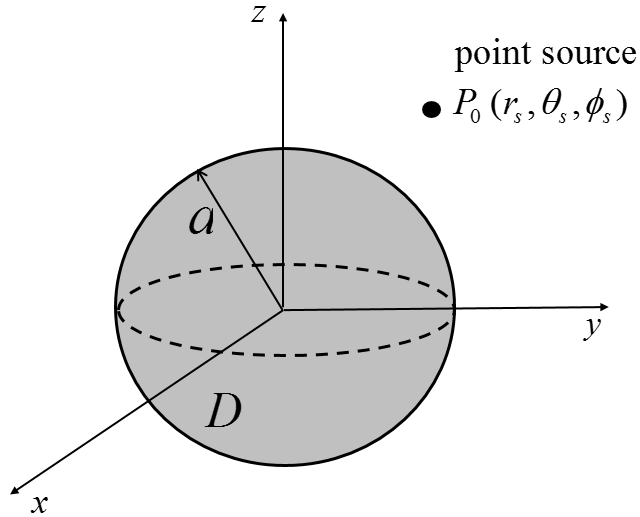
Figure 2.2 : The geometry of the direct scattering problem.

The incident field $u^i(\mathbf{r})$ satisfies the scalar wave equation

$$\Delta u^i(\mathbf{r}) + k_0^2 u^i(\mathbf{r}) = -P_0 \delta(\mathbf{r} - \mathbf{r}_s) \tag{2.28}$$

Taking (2.22) into account, the solution of (2.28) can be written as

$$u^i(r, \theta, \phi) = \frac{ik_0 P_0}{4\pi} \frac{e^{ik_0|\mathbf{r} - \mathbf{r}_s|}}{ik_0|\mathbf{r} - \mathbf{r}_s|} = \frac{ik_0 P_0}{4\pi} h_0^{(1)}(k|\mathbf{r} - \mathbf{r}_s|) \tag{2.29}$$

The total field $u(\mathbf{r})$, on the other hand, satisfies the following wave equation:

$$\Delta u(\mathbf{r}) - \frac{1}{\bar{\rho}(r)} \nabla \bar{\rho}(r) \cdot \nabla u(\mathbf{r}) + \bar{k}^2(r)u(\mathbf{r}) = -P_0 \delta(\mathbf{r} - \mathbf{r}_s) \tag{2.30}$$

Here, the density $\bar{\rho}(r)$ and the wave number $\bar{k}(r)$ are defined as

$$\bar{\rho}(r) = \begin{cases} \rho_0 & r > a \\ \rho(r) & r < a \end{cases} \tag{2.31}$$

and

$$\bar{k}(r) = \begin{cases} k_0 & r > a \\ \omega\sqrt{\rho(r)b(r)} & r < a \end{cases} \tag{2.32}$$

respectively. The aim of the direct scattering problem is to determine the total field $u(\mathbf{r})$ by solving (2.30), for the given functions of $\rho(r)$ and $b(r)$. The main purpose of this thesis is to solve this problem by first formulating Schwinger-Lippmann type integral equations, and then reducing these equations into a 1-D form. However, as stated in [33], in the case of variable density, the problem cannot be easily reduced to Schwinger-Lippmann integral equations. Therefore, to make the problem more manageable, the density will be considered constant throughout the whole space, that is $\rho(r) = \rho_0$. Although it limits the practicality of the solution, this assumption makes the dimension reduction process possible. For constant density, the term $\nabla \bar{\rho}(r)$ in (2.30) vanishes, and the equation becomes similar to (2.28).

At this point, we can define the scattered field as the difference of the total field and the incoming field:

$$u^s(\mathbf{r}) = u(\mathbf{r}) - u^i(\mathbf{r}) \tag{2.33}$$

Using this expression in (2.30) under the assumption of constant density yields

$$\Delta\left[u^i(\mathbf{r}) + u^s(\mathbf{r})\right] + k_0^2\left[u^i(\mathbf{r}) + u^s(\mathbf{r})\right] = -P_0\delta(\mathbf{r} - \mathbf{r}_s) - \left[\bar{k}^2(r) - k_0^2\right]u(\mathbf{r}) \tag{2.34}$$

Considering the wave equation for the incoming field given in (2.28), the equation for the scattered field can be obtained via (2.34) as

$$\Delta u^s(\mathbf{r}) + k_0^2 u^s(\mathbf{r}) = -k_0^2 v(r)u(\mathbf{r})$$

(2.35)

Here, the function $v(r)$ is the object function, and it is defined as

$$v(r) = \frac{\overline{k}^2(r)}{k_0^2} - 1$$

(2.36)

It is clear from (2.36) that $v(r)$ takes the value of zero outside the sphere. The solution of (2.35) can be formulated using the related Green's function $g(\mathbf{r}, \mathbf{r}')$, which is the fundamental solution of the equation:

$$\Delta g(\mathbf{r}, \mathbf{r}') + k_0^2 g(\mathbf{r}, \mathbf{r}') = -\delta(\mathbf{r} - \mathbf{r}')$$

(2.37)

The solution of (2.37) yields

$$g(\mathbf{r}, \mathbf{r}') = \frac{e^{ik_0|\mathbf{r} - \mathbf{r}'|}}{4\pi |\mathbf{r} - \mathbf{r}'|}$$

(2.38)

Comparing (2.35) with (2.37) demonstrates that the scattered field $u^s(\mathbf{r})$ can be expressed as a convolution integral containing the Green's function $g(\mathbf{r}, \mathbf{r}')$:

$$u^s(\mathbf{r}) = k_0^2 \int_D g(\mathbf{r}, \mathbf{r}')v(r')u(\mathbf{r}')dv' \qquad |\mathbf{r}| > a$$

(2.39)

This equation shows that when the total field $u(\mathbf{r})$ inside the sphere is known, the scattered field at any point outside the sphere can be determined. (2.39) is known as data equation in the inverse scattering problems, where the measured value of the scattered field constitutes the data of the problem. Now, in order to determine the equation for the total field inside the sphere, let us substitute (2.39) into (2.33) to obtain

$$u(\mathbf{r}) = u^i(\mathbf{r}) + k_0^2 \int_D g(\mathbf{r}, \mathbf{r}')v(r')u(\mathbf{r}')dv' \qquad |\mathbf{r}| \in D$$

(2.40)

This equation is a Fredholm integral equation of the second type, that should be solved to determine the total field inside the sphere. This equation is called the object equation. The solution of the direct scattering problem involves the solution of (2.40) for a given object function (acoustic profile). The scattered field is then evaluated at a measurement region outside the sphere using (2.39). A commonly used solution technique is MoM, where the 3-D spherical scatterer is discretized into smaller cells, and the integral equation is evaluated using point matching technique [14]. However, it should be noted that, because of the spherically symmetrical geometry, the problem can be reduced to a 1-D form along the radial direction. Such a reduction would decrease the necessary computational effort, and would also simplify the solution of both direct and inverse scattering problem. Therefore, in the next sub-section, the 3-D object and data equations, given in (2.40) and (2.39) respectively, will be reduced to a 1-D form using the mathematical properties of the spherical harmonics introduced in the previous sub-section.

2.2.2.2 Dimension reduction for the integral equations

In this sub-section the reduced object and data equations will be obtained. To this end, the series expansion defined by (2.14) and (2.15) will be used to express the total field and the incoming field. The main aim of this sub-section is to obtain integral equations involving the series expansion coefficients instead of the field values themselves. Therefore, we first introduce the series expansions of similar form as (2.14) for the fields $u(\mathbf{r})$, $u^s(\mathbf{r})$ and $u^i(\mathbf{r})$:

$$u(r,\theta,\phi) = \sum_{n=0}^{\infty} \sum_{m=-n}^{n} \hat{u}_{nm}(r) \frac{2n+1}{4\pi} \frac{(n-|m|)!}{(n+|m|)!} P_n^{|m|}(\cos\theta) e^{im\phi} \tag{2.41}$$

$$u^s(r,\theta,\phi) = \sum_{n=0}^{\infty} \sum_{m=-n}^{n} \hat{u}_{nm}^s(r) \frac{2n+1}{4\pi} \frac{(n-|m|)!}{(n+|m|)!} P_n^{|m|}(\cos\theta) e^{im\phi} \tag{2.42}$$

$$u^i(r,\theta,\phi) = \sum_{n=0}^{\infty} \sum_{m=-n}^{n} \hat{u}_{nm}^i(r) \frac{2n+1}{4\pi} \frac{(n-|m|)!}{(n+|m|)!} P_n^{|m|}(\cos\theta) e^{im\phi} \tag{2.43}$$

Note that the coefficients of the series expansions $\hat{u}_{nm}(r)$, $\hat{u}_{nm}^s(r)$, and $\hat{u}_{nm}^i(r)$ are functions of radial distance only, since the angular dependence is expressed by the

spherical harmonics. These coefficients will appear in the final form of the reduced integral equations. We also expand the Green's function $g(\mathbf{r}, \mathbf{r}')$ using the addition theorem given in (2.27), and by taking (2.22) into account:

$$g(\mathbf{r},\mathbf{r}') = \frac{ik_0}{4\pi} \sum_{n=0}^{\infty} \sum_{m=-n}^{n} \frac{(2n+1)(n-|m|)!}{(n+|m|)!} j_n(k_0 r_<) h_n^{(1)}(k_0 r_>)$$
$$\times P_n^{|m|}(\cos\theta) P_n^{|m|}(\cos\theta') e^{im(\phi-\phi')}$$

(2.44)

Here, $r_<$ and $r_>$ stand for the smaller and larger term of the pair r, r' respectively. In order to reduce the object equation (2.40) into a 1-D form, let us multiply both sides of the equation by $P_n^m(\cos\theta) e^{-im\phi} \sin\theta$, and integrate over the unit spherical surface. Since this operation is equivalent to the integration defined in (2.15), the resulting equation involves the coefficients $\hat{u}_{nm}(r)$ and $\hat{u}_{nm}^i(r)$:

$$\hat{u}_{nm}(r) = \hat{u}_{nm}^i(r) + k_0^2 \int_0^{2\pi}\int_0^{\pi} \left[\int_D g(\mathbf{r},\mathbf{r}') v(r') u(\mathbf{r}') dv' \right]$$
$$\times P_n^{|m|}(\cos\theta) \sin\theta e^{-im\phi} d\theta d\phi$$

(2.45)

It is clear from (2.45) that, to complete the series expansion, the terms $g(\mathbf{r},\mathbf{r}')$ and $u(\mathbf{r}')$ in the volume integral should also be expanded. Therefore, we substitute the expression given for $g(\mathbf{r},\mathbf{r}')$ in (2.44) into (2.45) to transform the integral in the equation into the form

$$k_0^2 \int_0^{2\pi}\int_0^{\pi} \left\{ \int_D \frac{ik_0}{4\pi} \sum_{\bar{n}=0}^{\infty} \sum_{\bar{m}=-\bar{n}}^{\bar{n}} \frac{(2\bar{n}+1)(\bar{n}-|\bar{m}|)!}{(\bar{n}+|\bar{m}|)!} j_{\bar{n}}(k_0 r_<) h_{\bar{n}}^{(1)}(k_0 r_>) P_{\bar{n}}^{|\bar{m}|}(\cos\theta) \right.$$
$$\left. \times P_{\bar{n}}^{|\bar{m}|}(\cos\theta') e^{i\bar{m}(\phi-\phi')} v(r') u(r',\theta',\phi') dv' \right\} P_n^{|m|}(\cos\theta) \sin\theta e^{-im\phi} d\theta d\phi$$

(2.46)

Here, the subscripts $\bar{n}$ and $\bar{m}$ are used to distinguish the expansion for the Green's function from the previous integration with the spherical harmonics denoted by n and m. The volume integral within the braces can be written in a more open form as

$$\int_0^a \int_0^{2\pi} \int_0^{\pi} \frac{ik_0}{4\pi} \sum_{\bar{n}=0}^{\infty} \sum_{\bar{m}=-\bar{n}}^{\bar{n}} \frac{(2\bar{n}+1)(\bar{n}-|\bar{m}|)!}{(\bar{n}+|\bar{m}|)!} j_{\bar{n}}(k_0 r_<) h_{\bar{n}}^{(1)}(k_0 r_>) P_{\bar{n}}^{|\bar{m}|}(\cos\theta)$$
$$\times P_{\bar{n}}^{|\bar{m}|}(\cos\theta') e^{i\bar{m}\phi} e^{-i\bar{m}\phi'} v(r') u(r',\theta',\phi') r'^2 \sin\theta' d\theta' d\phi' dr'$$

(2.47)

Note that the integration of the terms involving θ', ϕ' over the unit spherical surface, that is, over the domain $[0, \pi] \times [0, 2\pi]$, yields the coefficients $\hat{u}_{nm}(r)$, since the kernel of the integral has the same form as (2.15). Therefore, (2.47) becomes

$$
\int_0^a \frac{ik_0}{4\pi} \sum_{\bar{n}=0}^{\infty} \sum_{\bar{m}=-\bar{n}}^{\bar{n}} \frac{(2\bar{n}+1)(\bar{n}-|\bar{m}|)!}{(\bar{n}+|\bar{m}|)!} j_{\bar{n}}(k_0 r_<) h_{\bar{n}}^{(1)}(k_0 r_>) v(r') \hat{u}_{\bar{n}\bar{m}}(r') r'^2 dr'
$$
$$
\times P_{\bar{n}}^{|\bar{m}|}(\cos\theta) e^{i\bar{m}\phi}
$$
(2.48)

Through this procedure the integral has been reduced to a 1-D form. However, to complete the reduction process, all angular terms must be eliminated from the original object equation. To this end, we subsititute (2.48) into (2.45) to further take advantage of the orthogonality relationship. At this point, the object equation has the form

$$
\hat{u}_{nm}(r) = \hat{u}_{nm}^i(r) + \sum_{\bar{n}=0}^{\infty} \sum_{\bar{m}=-\bar{n}}^{\bar{n}} \frac{(2\bar{n}+1)(\bar{n}-|\bar{m}|)!}{(\bar{n}+|\bar{m}|)!}
$$
$$
\times \left\{ \int_0^a \frac{ik_0^3}{4\pi} j_{\bar{n}}(k_0 r_<) h_{\bar{n}}^{(1)}(k_0 r_>) v(r') \hat{u}_{\bar{n}\bar{m}}(r') r'^2 dr' \right.
$$
$$
\left. \times \int_0^{2\pi} \int_0^{\pi} P_{\bar{n}}^{|\bar{m}|}(\cos\theta) e^{i\bar{m}\phi} P_n^{|m|}(\cos\theta) e^{-im\phi} \sin\theta d\theta d\phi \right\}
$$
(2.49)

The last integral in (2.49) is a direct application of the orthogonality relationship for the spherical harmonics given in (2.13):

$$
\int_0^{2\pi} \int_0^{\pi} P_{\bar{n}}^{|\bar{m}|}(\cos\theta) P_n^{|m|}(\cos\theta) e^{i\bar{m}\phi} e^{-im\phi} \sin\theta d\theta d\phi = \begin{cases} 0 & n,m \neq \bar{n}, \bar{m} \\ \dfrac{4\pi}{2\bar{n}+1} \dfrac{(\bar{n}+|\bar{m}|)!}{(\bar{n}-|\bar{m}|)!} & n,m = \bar{n}, \bar{m} \end{cases}
$$
(2.50)

It should be noted that, since for any $n,m \neq \bar{n}, \bar{m}$ the integral takes the value of zero, all the terms of the series expension in (2.49) are zeros except for $\bar{n}, \bar{m} = n, m$. Therefore, the series expansion on $\bar{n}, \bar{m}$ can be removed from the final form of the object equation which is obtained as

$$
\hat{u}_{nm}(r) = \hat{u}_{nm}^i(r) + ik_0^3 \int_0^a j_n(k_0 r_<) h_n^{(1)}(k_0 r_>) v(r') \hat{u}_{nm}(r') r'^2 dr' \qquad r < a
$$
(2.51)

(2.51) can be considered as the reduced object equation. The dimension reduction for the data equation (2.39) follows the same procedure, and can be achieved in a

straightforward manner. Therefore, we give the final form of the coefficients of the scattered field as

$$\hat{u}_{nm}^s(r) = ik_0^3 h_n^{(1)}(k_0 r) \int_0^a j_n(k_0 r') v(r') \hat{u}_{nm}(r') r'^2 dr' \qquad r > a \tag{2.52}$$

Note that, in the region outside the sphere, the field point r has greater value than the source point r'. Therefore, the radial dependence of the scattered field is always expressed in terms of spherical Hankel functions of the first kind.

Through the dimension reduction process, the original system, formed by (2.39) and (2.40), is replaced by the reduced integral equations (2.51) and (2.52). By solving these reduced integral equations, one can obtain the series expansion coefficients for the interior field and the scattered field. The actual field values can be then determined by substituting these coefficients into the series expansions defined in (2.40) and (2.41). Note that the solution of the system formed by (2.51)-(2.52) can be achieved via a simple discretization of the interval $r \in [0, a]$, since the kernels of the integrals are smooth functions. The details of the discretization procedure is presented in Appendix A. In the next sub-section, some numerical simulations will be presented to assess the performance of the proposed solution. However, before concluding this sub-section, we will present the open expression of the coefficients for the incoming field $\hat{u}_{nm}^i(r)$, to complete the dimension reduction formulation.

The coefficients of the incoming field

First, the coefficients for the point source located at the point (r_s, θ_s, ϕ_s), as indicated in Fig. 2.1, will be determined. The field created by this source is expressed as

$$\begin{aligned}
u^i(\mathbf{r}, \mathbf{r}') = u^i(r, \theta, \phi) &= \frac{ik_0 P_0}{4\pi} \sum_{n=0}^{\infty} \sum_{m=-n}^{n} \frac{(2n+1)(n-|m|)!}{(n+|m|)!} j_n(k_0 r_<) h_n^{(1)}(k_0 r_>) \\
&\times P_n^{|m|}(\cos\theta) P_n^{|m|}(\cos\theta_s) e^{im(\phi-\phi_s)}
\end{aligned} \tag{2.53}$$

Here, P_0 is the strength of the source, and $r_<$, $r_>$ stand for the smaller and larger term of the pair r, r_s respectively. Expectedly, this expression has the same form as the Green's function $g(\mathbf{r}, \mathbf{r}')$. The coefficients $\hat{u}_{nm}^i(r)$ are defined by the integral

$$\hat{u}^i_{nm}(r) = \int\limits_0^{2\pi}\int\limits_0^{\pi} u^i(r,\theta,\phi)\, P_n^{|m|}(\cos\theta)\, e^{-im\phi} \sin\theta\, d\theta d\phi \tag{2.54}$$

Substituting (2.53) into (2.54) yields

$$\hat{u}^i_{nm}(r) = \frac{ik_0 P_0}{4\pi} \sum_{\bar{n}=0}^{\infty} \sum_{\bar{m}=-\bar{n}}^{\bar{n}} \frac{(2\bar{n}+1)(\bar{n}-|\bar{m}|)!}{(\bar{n}+|\bar{m}|)!}\, j_{\bar{n}}(k_0 r_<)h_{\bar{n}}^{(1)}(k_0 r_>)P_n^{|m|}(\cos\theta_s)e^{-im\phi_s}$$
$$\times \int\limits_0^{2\pi}\int\limits_0^{\pi} P_{\bar{n}}^{|\bar{m}|}(\cos\theta)e^{i\bar{m}\phi} P_n^{|m|}(\cos\theta)\, e^{-im\phi} \sin\theta\, d\theta d\phi \tag{2.55}$$

The subscripts $\bar{n}$ and $\bar{m}$ are used once again to distinguish the series expension from the integration of (2.54). It is clear that (2.55) has the same form as (2.49), and the angular integral is identical to the orthogonality relationship (2.50). Therefore, the final form of the coefficients $\hat{u}^i_{nm}(r)$ for the point source can be written as

$$\hat{u}^i_{nm}(r) = ik_0 P_0\, j_n(k_0 r_<)h_n^{(1)}(k_0 r_>)P_n^{|m|}(\cos\theta_s)e^{-im\phi_s} \tag{2.56}$$

where $r_< = \min(r,r_s)$ and $r_> = \max(r,r_s)$.

Another widely used form for the incoming field is the acoustic plane wave. Therefore, we will also obtain the coefficients for the plane wave travelling in the negative z direction. The expression of this field was already given as a series expansion in (2.19) as

$$u^i(r,\theta,\phi) = e^{-ik_0 z} = \sum_{n=0}^{\infty}(-i)^n\,(2n+1)\,j_n(k_0 r)P_n(\cos\theta) \tag{2.57}$$

Multiplying both sides of (2.57) by $P_n^{|m|}(\cos\theta)e^{-im\phi}$, and integrating over the unit spherical surface yields

$$\hat{u}^i_{nm}(r) = \int\limits_0^{2\pi}\int\limits_0^{\pi}\{ \sum_{\bar{n}=0}^{\infty}(-i)^{\bar{n}}\,(2\bar{n}+1)\,j_{\bar{n}}(k_0 r)P_{\bar{n}}(\cos\theta)\, P_n^{|m|}(\cos\theta)$$
$$\times e^{-im\phi} \sin\theta\, d\theta d\phi\ \} \tag{2.58}$$

Considering the identity

$$P_n(u) = P_n^0(u) \tag{2.59}$$

and the orthogonality relationship for the Legendre functions given in (2.12), the integration on the interval $\theta \in [0, \pi]$ in (2.58) can be determined as

$$\int_0^\pi P_{\bar{n}}(\cos\theta) \, P_n^m(\cos\theta)\sin\theta d\theta = \begin{cases} 0 & \bar{n} \neq n, m \neq 0 \\ \dfrac{2}{2n+1} & \bar{n} = n, m = 0 \end{cases} \tag{2.60}$$

It is clear from (2.60) that, as a result of the orthogonality, the series terms for $\bar{n} \neq n$ in (2.58) will not have any contribution to the integration. Also for $m \neq 0$, the coefficients $\hat{u}_{nm}^i(r)$ will be zeros. As the integration on the interval $\phi \in [0, 2\pi]$ yields

$$\int_0^{2\pi} e^{-im\phi} d\phi = \begin{cases} 0 & m \neq 0 \\ 2\pi & m = 0 \end{cases} \tag{2.61}$$

the final form of the coefficients for the acoustic plane wave travelling in the negative z direction is obtained as

$$\hat{u}_{nm}^i(r) = \begin{cases} 0 & m \neq 0 \\ (-i)^n 4\pi j_n(k_0 r) & m = 0 \end{cases} \tag{2.62}$$

2.2.3 Numerical simulations

In this sub-section, we will represent the results of the numerical simulations in order to validate the accuracy of the method proposed in the previous sections. These simulations will involve comparisons with alternative techniques available in the literature for different configurations. Since the analytical method can be considered as the gold standard among these alternatives, it will be frequently employed in the comparisons. However, an analytical solution is only available for piecewise homogeneous layered spheres. Therefore, for continuous profiles, the comparisons will be made using the results already published in the literature, and the frequently used numerical technique MoM. In the first part of the sub-section, the calculation of the values of the total field inside the sphere by (2.51) will be compared with the alternatives. The effect of the change in the operating frequency, and the number of the terms involved in the series expansions (2.41)-(2.43) will also be analysed. In the

27

second part, the simulations will involve the calculation of the scattered field outside the sphere using (2.52), for continuous and layered profiles. The accuracy of the results presented in that section also demonstrates that the method can be reliably used in the inverse scattering problems that will be investigated in the next part of the thesis.

2.2.3.1 Comparisons for the total field inside the sphere

For the comparison with the analytical expression, first a two layered piecewise homogeneous sphere described by

$$\frac{b(r)}{b_0} = \begin{cases} 1.5 & 0 \le \dfrac{r}{a} \le 0.5 \\[2mm] 1.2 & 0.5 < \dfrac{r}{a} \le 1 \end{cases} \tag{2.63}$$

will be considered. Here, b_0 is the compressibility of the surrounding medium which is characterized by a constant wave number $k_0 = \omega\sqrt{b_0\rho_0} = 20$. The radius of the sphere is chosen as $a = 0.1m$, and it is illuminated by a time harmonic point source situated at the point defined by $r_s = 0.2m$, $\theta_s = \pi/3$, $\phi_s = \pi/2$. The total field inside the sphere, as a function of the radial distance r, is assumed to be measured on the line defined by $\theta = \phi = \pi/6$. The field values are calculated by the reduced integral equation (2.51), and the analytical solution explained in Appendix B. For the solution, the integral in (2.51) is discretized by 30 points. The results presented in Fig. 2.3 demonstrate excellent agreement between two methods.

It is clear from the results that, the field inside the sphere is slowly varying along the radial direction. It is an expected result, since the value $k_0 a$, which represents the electrical size of the sphere, is rather small for this example. Therefore, in this example number of terms included in the series expansions (2.41) and (2.43) is chosen as $N_{max} = 5$. The higher order terms, which correspond to more rapidly varying harmonics, do not have a significant contribution to the total field. Accordingly, adding more terms do not change the final solution, since the related coefficients have considerably smaller values compared to the lower order terms. In the next example, the results for the cases with significantly larger k_0 values will be considered to further demonstrate this point.
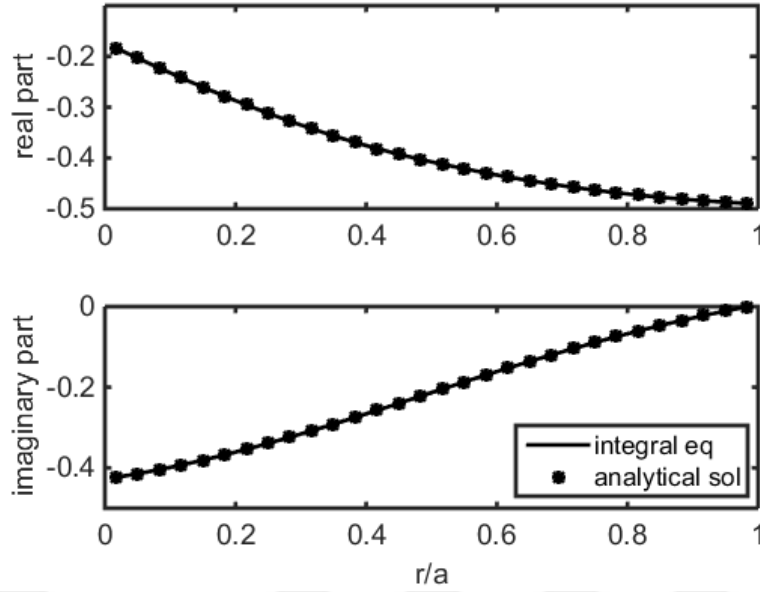
Figure 2.3 : Real and imaginary parts of the total field inside a two layered sphere, solution with the reduced integral equation and the analytical expression ($k_0 = 20$).

First, for the same configuration analysed in the previous example, the wave number of the outside region will be increased to $k_0 = 100$. The results presented in Fig. 2.4 demonstrate that, since the variation of the field would be greater for an electrically larger sphere, more terms should be added to the series expansion. Comparing the results obtained by the analytical solution, with those obtained by the integral equations for $N_{max} = 5$ proves that the number of terms included in the previous example is inadequate for this example. Increasing the number of terms to $N_{max} = 10$ significantly reduces the difference, however a perfect match does not occur for this case either. On the other hand, as seen in Fig. 2.5, the agreement between two methods is once again established when the number of terms is increased to $N_{max} = 15$. Moreover, note that adding further terms do not effect the outcome, since the results for $N_{max} = 20$ also displays an excellent agreement with the analytical result. Therefore, it can be concluded that the method produces stable results when the number of terms included in the series expansion is sufficiently large. As final example to illustrate this point, and to assess the performance of the method, the same problem is solved for $k_0 = 200$. The simulations presented in Fig. 2.6, demonstrate that for this wave number value, the agreement is reached when the limit is chosen as $N_{max} = 25$. It is clear from the analysis that the method developed in this thesis shows good

agreement with the analytical solution in the case of layered spheres. Moreover, it is suitable to be used in the direct scattering problems involving electrically large spheres, provided that appropriate parameters are chosen.
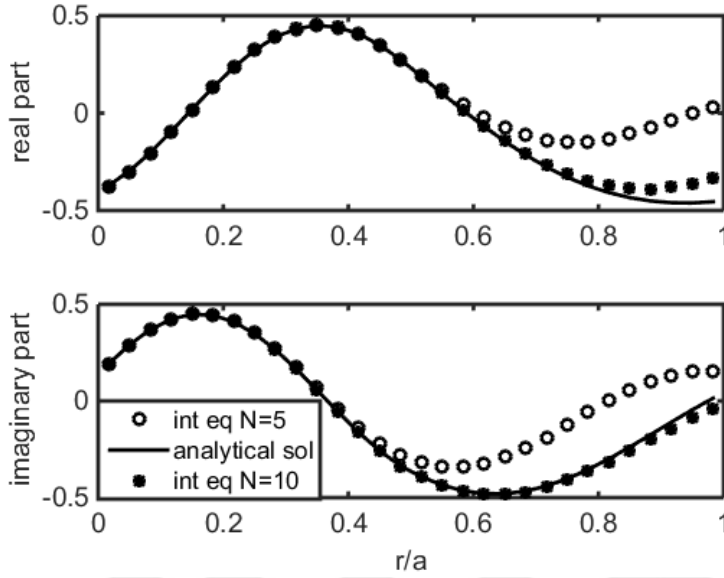
Figure 2.4 : Real and imaginary parts of the total field inside a two layered sphere, solution with the reduced integral equation for $N_{max} = 5$ and $N_{max} = 10$ ($k_0 = 100$).
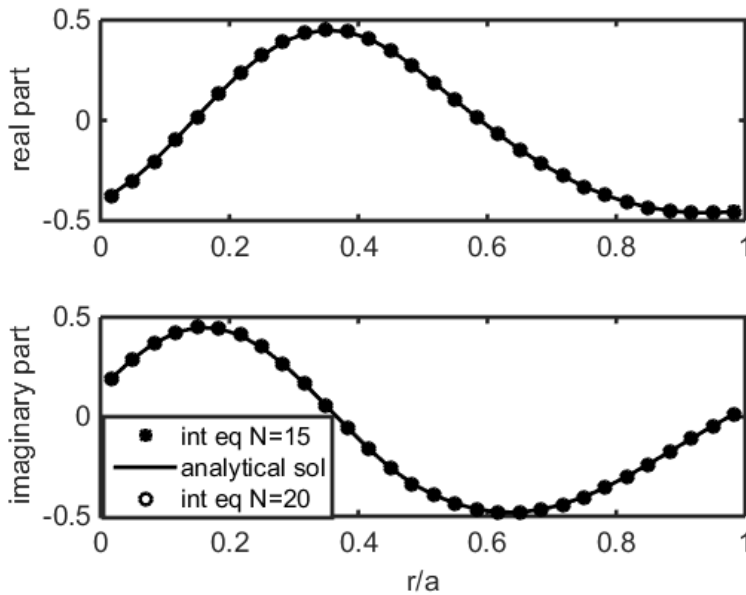
Figure 2.5 : Real and imaginary parts of the total field inside a two layered sphere, solution with the reduced integral equation for $N_{max} = 15$ and $N_{max} = 20$ ($k_0 = 100$).
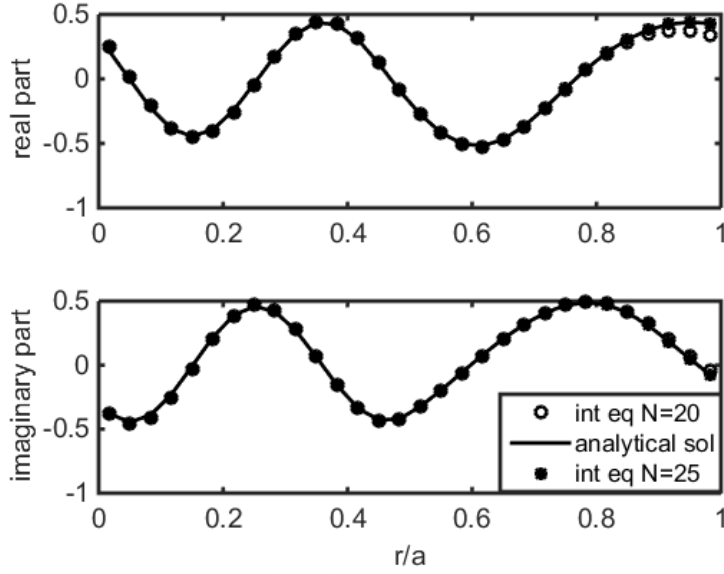
Figure 2.6 : Real and imaginary parts of the total field inside a two layered sphere, solution with the reduced integral equation for $N_{max} = 20$ and $N_{max} = 25$ ($k_0 = 200$).

For the continuous profiles, an analytical solution does not exist. Therefore, the accuracy of the method for these types of the profiles is tested by comparisons with the results presented in the available publications. In [35], the magnitude of the total field inside a sphere described by

$$\frac{b(r)}{b_0} = 5 + 5\frac{r}{a} \tag{2.64}$$

has been calculated for different $k_0 a$ values. The sphere is illuminated by an acoustic plane wave propagating along the negative z direction, and the field inside the sphere is assumed to be measured on a line in the xy plane. Here, we have produced the results for the same configuration, using the integral equation (2.51). For all $k_0 a$ values, the wave number is chosen as $k_0 = 21$, and the radius a is changed accordingly. The number of terms included in the series expansion is identical for all cases to the number chosen in [35]; for example, the number is chosen as $N_{max} = 27$ for $k_0 a = 16.8$. For larger $k_0 a$ values of 8.4 and 16.8, the integrals are discretized by 60 points to further increase the accuracy. The results presented in Fig. 2.7 show a quite good agreement with those presented in [35]. Therefore, it can be concluded that the method can also be reliably used for the spheres with continuously varying profiles.
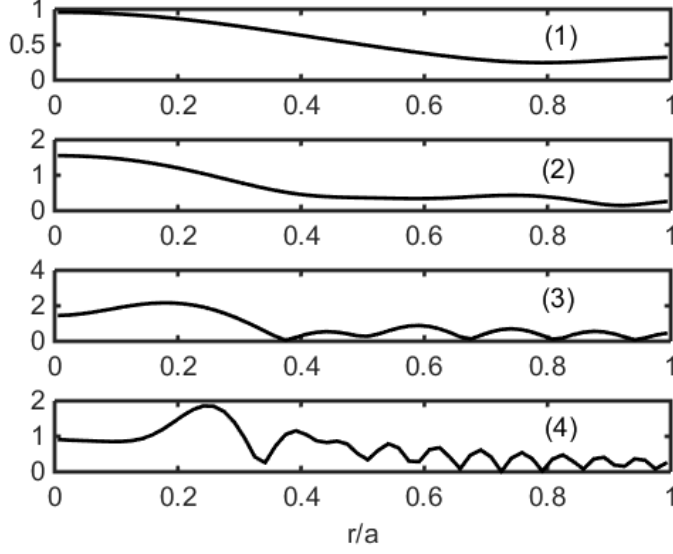
Figure 2.7 : The field variation inside the sphere described by $b(r)/b_0 = 5+5(r/a)$, for different $k_0 a$ values: (1) $k_0 a = 2.1$; (2) $k_0 a = 4.2$; (3) $k_0 a = 8.4$; (4) $k_0 a = 16.8$.

2.2.3.2 Comparisons for the scattered field outside the sphere

After determining the total interior field via (2.51), the scattered field can be evaluated at any point outside the sphere using (2.52). The comparisons for the scattered field can be made using the analytical expression as well as numerical techniques. In this sub-section, we will use the MoM solution developed in [14] as an alternative technique alongside the analytical solution. In this method, the 3-D object equation (2.40) is solved by a discretization of the inhomogeneous 3-D scatterer into cubic cells. A brief presentation of the MoM formulation for the acoustic case can be found in Appendix C.

As a first example, the field scattered by the two-layed sphere defined in (2.63) will be considered. The point source is supposed to be located at the point by $r_s = 0.25m$, $\theta_s = \pi/3$, $\phi_s = \pi/2$, and the measurement line is defined by $r_{obs} = 0.2m$, $\theta_{obs} = \pi/2$, $\phi_{obs} \in [0, 2\pi]$. The sphere has a radius of $a = 0.1m$, and the wave number of the outside region is chosen as $k_0 = 8\pi$. The scattered field is calculated by three different methods: the reduced integral equation (2.52), the analytical expression and MoM. The results presented in Fig. 2.8 show good agreement between three methods, although a perfect match does not occur. For this simulation, the integral in (2.52) is discretized by 30 points, and the number of terms for the series expansions in (2.41)-(2.43) is

32

chosen as $N_{max} = 10$, considering the electrical size of the sphere. On the other hand, for MoM, the sphere is discretized into $15 \times 15 \times 15$ cubic cells. The agreement between analytical solution and the integral equation method is expected, considering previously demonstrated agreement for the interior field. The results show that for moderate size and contrast values, MoM also provides a reliable alternative. The limits of the agreement with MoM will be tested in the next example.
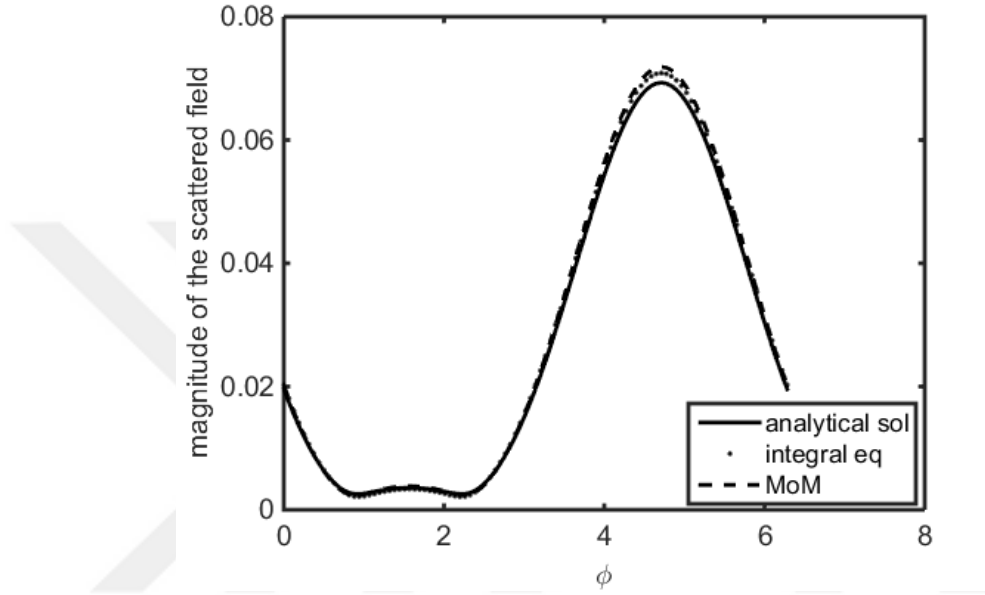
Figure 2.8 : The magnitude of field scattered by a two layered sphere, calculated by three methods. Measurement region: $r_{obs} = 0.2\,m$, $\theta_{obs} = \pi/2$, $\phi_{obs} \in [0, 2\pi]$; $k_0 = 8\pi$.

However, before analysing different configurations, the behaviour of the coefficients for the series expansions should be discussed. Since the measurement have been made at a constant radial distance $r = r_{obs}$, the variation of the coefficients for the scattered field, $\hat{u}_{nm}^s(r_{obs})$, can be observed more easily compared to case involving calculations of the interior field as a function of radial distance. Therefore, in Fig 2.9, the magnitude of the coefficients for $m = 0$; that is $\left| \hat{u}_{n0}^s(r_{obs}) \right|$ for $n = 1, 2, .., 10$; has been presented. The terms with $m = 0$ are chosen over remaining coefficients because those are the most dominant terms that form the scattered field. It is clear from the results that the contribution of the terms decreases rapidly as the index term n grows, and for $n > 5$, the effect of the related term becomes negligeable. This observation is in accord with the results for the interior field presented in the previous sub-section.
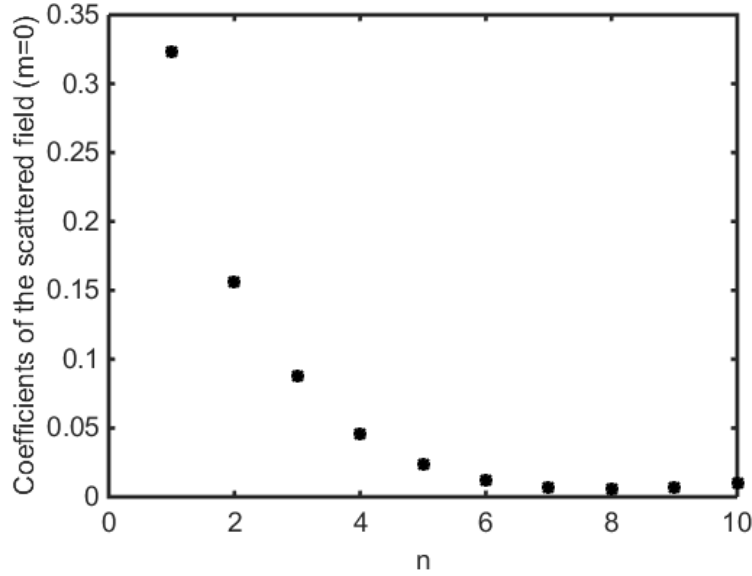
Figure 2.9 : $\left|\hat{u}_{n0}^{s}(r_{obs})\right|$: The coefficients of the series expansion for the scattered field

Now, to test the performances of the methods in the case of electrically larger sphere, the same configuration as the previous example will be analysed after changing the wave number of the outside region to $k_0 = 200$. Similar to the case of interior field, the number of terms in the series expansions is increased to $N_{max} = 30$ in order to handle the relatively rapid variation of the field inside and outside the sphere. In Fig 2.10, the results obtained via three different methods are compared. It is clear from the results that, while the solution with the integral equation and the analytical expression display considerable agreement, the solution with MoM diverges substantially from other calculations. This result shows that the discretization into $15{\times}15{\times}15$ cubic cells is not adequate to obtain a reliable solution for a sphere of this size. Therefore, for the results presented in Fig 2.11, a discretization into $25{\times}25{\times}25$ cubic cells has been used for the solution with MoM. The comparison with the previous results of the remaining methods demonstrate a significant improvement; however, the level of agreement is still lower compared to the other two methods. This is an expected result, considering that the analytical solution and the solution with the integral equations are designed specifically for the spherical geometry, whereas the cubic cell discretization of MoM can only approximately represent the spherical scatterer. In conclusion, the agreement between the method developed in this thesis, and the analytical solution shows that the method can be reliably used in order to determine the field scattered by spheres with layered profiles. On the other hand, MoM, which is the only alternative to

34

be used in the comparisons for continuous profiles, have a relatively limited accuracy, especially for electrically larger scatterers. Therefore, in the examples involving continuous profiles, a general agreement should be expected instead of a perfect match.
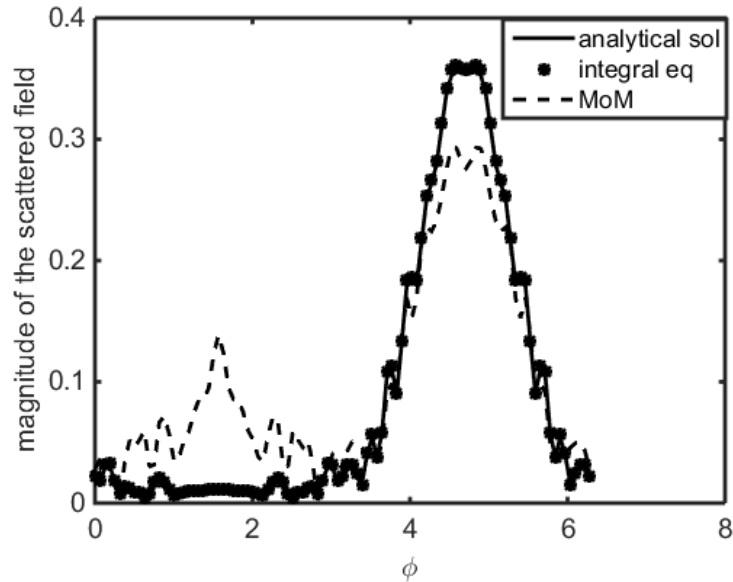
Figure 2.10 : The magnitude of field scattered by a two layered sphere, calculated by three methods ($k_0 = 200$). The number of terms for the solution with the integral equations is $N_{max} = 30$, the discretization for MoM involves $15 \times 15 \times 15$ cubic cells.
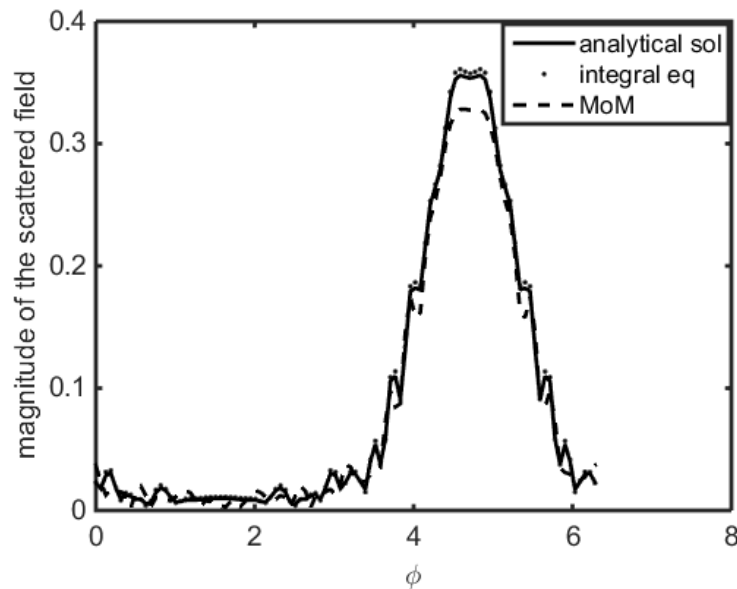
Figure 2.11 : The magnitude of field scattered by a two layered sphere, calculated by three methods ($k_0 = 200$). The number of terms for the solution with the integral equations is $N_{max} = 30$, the discretization for MoM involves $25 \times 25 \times 25$ cubic cells.

As a first example for the continuous profiles, the linearly varying profile defined in (2.64) will be analysed. In order to make the comparison with MoM feasible, the wave number of the outside region is chosen as $k_0 = 8\pi$, and the radius of the sphere is determined as $a = 0.1m$. For the solution with integral equation, the number of included terms is chosen as $N_{max} = 10$, and $15 \times 15 \times 15$ cubic cell discretization is used for MoM. The measurement region is the arc defined by $r_{obs} = 0.2m$, $\theta_{obs} \in [0, \pi]$, $\phi_{obs} = 0$. Two different sources have been used for the excitation of the scattered field. In Fig 2.12, the scattered field in the case of point source excitation has been calculated via the integral eqautions and MoM. The point source is situated at the point $r_s = 0.25m$, $\theta_s = \pi/3$, $\phi_s = \pi/2$. On the other hand, the results for the case of plane wave excitation is presented in Fig 2.13. The plane wave is assumed to be travelling along the negative z direction. For both cases, the results show good agreement, however, a perfect match does not occur. Although the sphere is electrically small, this divergence can be expected, considering the relatively high contrast between the sphere and the outside region. Therefore, relatively low contrast values should be used to obtain better matching results.
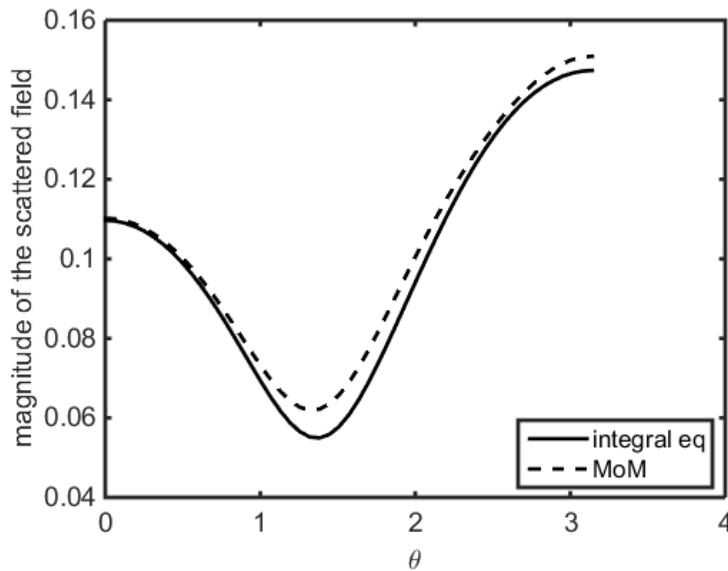
Figure 2.12 : The field scattered by the sphere described by $b(r)/b_0 = 5 + 5(r/a)$ in the case of point source excitation, calculated by the integral equations and MoM. Measurement region: $r_{obs} = 0.2m$, $\theta_{obs} \in [0, \pi]$, $\phi_{obs} = 0$; ($k_0 = 8\pi$).
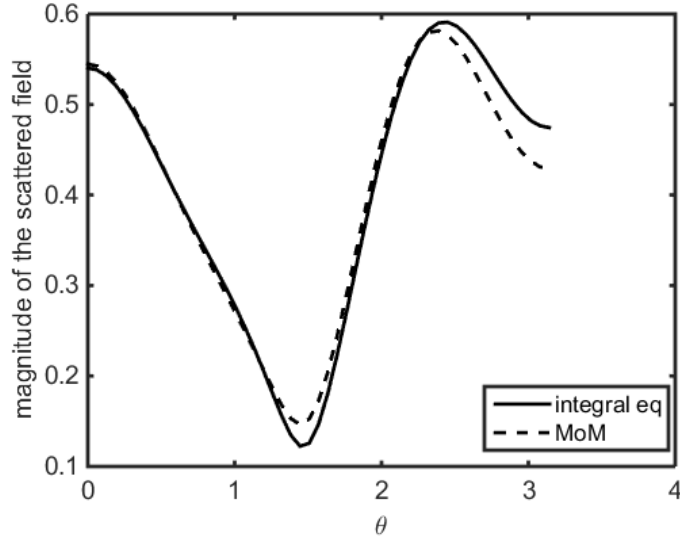
Figure 2.13 : The field scattered by the sphere described by $b(r)/b_0 = 5 + 5(r/a)$ in the case of plane wave excitation, calculated by the integral equations and MoM. Measurement region: $r_{obs} = 0.2\,m$, $\theta_{obs} \in [0, \pi]$, $\phi_{obs} = 0$; ($k_0 = 8\pi$).

Since the data for the inverse scattering problems, i.e. the scattered field, will be produced using MoM in order to prevent inverse crime, obtaining accurate results for the scattered field is crucially important. Therefore, profiles with relatively lower contrast values should be used in order to increase the accuracy and the level of agreement between two methods. To this end, we will first consider the well-known Luneburg lens described by $b(r)/b_0 = 2 - (r/a)^2$ which has a slowly varying smooth profile. The sphere with a radius $a = 0.1\,m$ is illuminated by the point source located at the point $r_s = 0.25\,m$, $\theta_s = \pi/3$, $\phi_s = \pi/2$. The outside region is characterized by the wave number $k_0 = 8\pi$, and the scattered field is assumed to be measured on the line is defined by $r_{obs} = 0.2\,m$, $\theta_{obs} = \pi/2$, $\phi_{obs} \in [0, 2\pi]$. Same parameters as the previous example with the linear profile have been used for the solutions with the integral equations and MoM. The results presented in Fig. 2.14 demonstrate that for slowly changing smooth profiles, the methods show perfect agreement.

Secondly, an oscillating profile described by $b(r)/b_0 = 1.5 + 0.5\cos(3\pi r/a)$ is analysed using the same configuration. Although the variation of this profile is considerably greater than Luneburg lens, the methods nevertheless demonstrate perfect agreement as seen in Fig. 2.14. Therefore, it can be concluded that for relatively low contrast values, MoM can be reliably used to produce data for the inverse

problems. Moreover, it is clear from the examples presented in this section that the method based on the reduced integral equations yields accurate results in the calculations of the interior and the scattered field for various types of profiles.
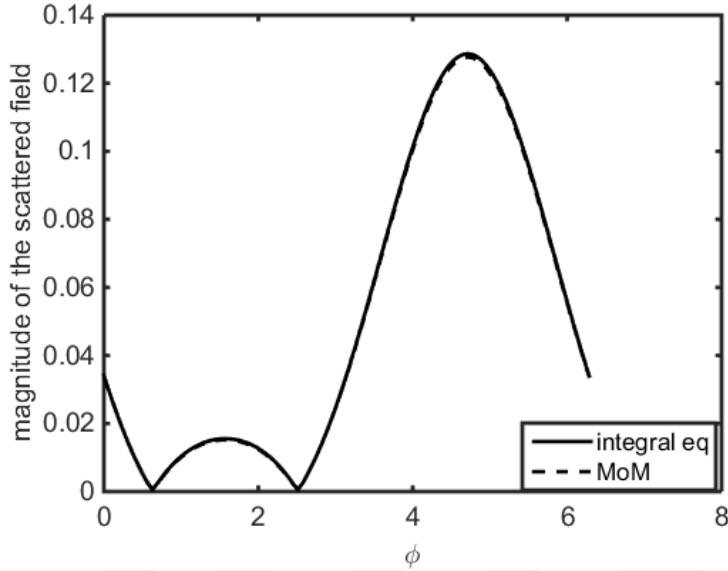
Figure 2.14 : The field scattered by the Luneburg lens, calculated by the integral equations and MoM. Measurement region: $r_{obs} = 0.2m$, $\theta_{obs} = \pi/2$, $\phi_{obs} \in [0, 2\pi]$.
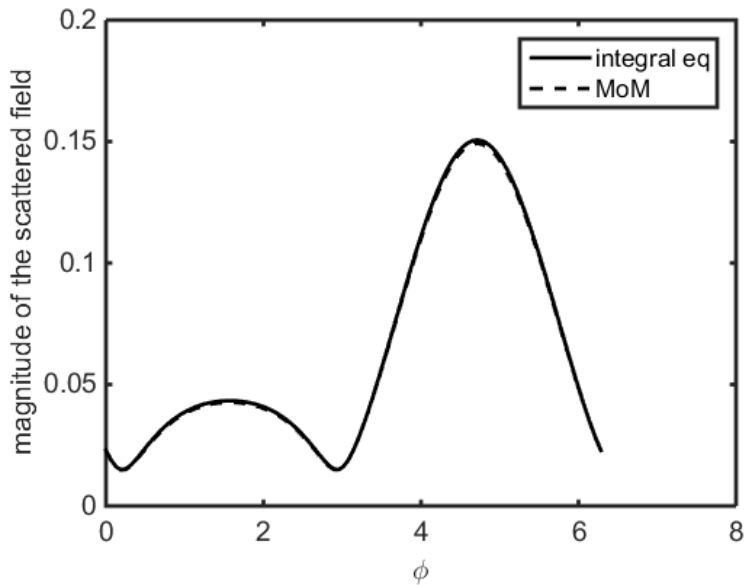
Figure 2.15 : The field scattered from the sphere of $b(r)/b_0 = 1.5 + 0.5\cos(3\pi r/a)$, calculated by the integral equations and MoM. Measurement region: $r_{obs} = 0.2m$, $\theta_{obs} = \pi/2$, $\phi_{obs} \in [0, 2\pi]$; ($k_0 = 8\pi$).

2.3 Inverse Scattering Problem

In this section, the solution of the 1-D profile inversion problem in spherical coordinates will be developed. As stated in the introduction, the aim of this problem is to reconstruct the acoustical profile, which is a function of the radial distance only, via a measurement of the scattered acoustic field on a certain domain outside the sphere. Although this can be considered as a 3-D problem, it can be reduced into a 1-D form by the dimension reduction process demonstrated in the previous sections. Therefore, the original 3-D inverse scattering problem will be restated in a 1-D form through the system formed by the reduced integral equations (2.51) and (2.52). The detailed formulation of the problem, and its solution via a Newton based iterative scheme will be presented in the second part of this section. However, before the development of the solution, a brief discussion of the theoretical features of the inverse problems, alongside the related concepts of ill-posedness and non-linearity, will be given in the first part. Finally, the section will be concluded in the third part where the results of numerical simulations testing the effectiveness of the method will be presented.

2.3.1 Theoretical background

The main difficulty in the solution of the inverse scattering problems lies in the inherent non-linearity and the ill-posedness of the problems [2]. The measured data, that is the scattered field, always contain errors; and due to the ill-posedness, even small deviations in the measured field can cause large errors in the reconstructed profile [2]. Therefore, a typical solution would involve a linearization process such as Born approximation, and a regularization technique such as Tikhonov regularization, in order to obtain a stable solution. In short, the main aim of the solution techniques is to obtain useful approximate solutions instead of an exact solution [2].

In this sub-section, we will first give the mathematical definition of the ill-posedness, and then discuss the regularization procedures that are used to obtain approximate solutions for the ill-posed problems. The entire section can be considered as a summary of the rigorous treatment of these subjects presented in [2]. Therefore, for the mathematical proofs and the systematic analysis of the concepts mentioned in this section, readers should refer to sections four and five of the book [2].

The definition of well-posedness posited in [66] states that for an operator $A:U \subset X \to V \subset X$, from a subset U of a normed space X into a subset V of a normed space Y, the equation

$$A\varphi = f \qquad (2.65)$$

is called well-posed if $A:U \to V$ is bijective and the inverse operator $A^{-1}:V \to U$ is continuous. Otherwise the equation is called ill-posed [2]. This definition of well-posedness has three components. First, a solution should exist for all $f \in V$, that is A must be surjective. Second, the solution should be unique, that is A must be injective. Finally, A^{-1} should be continuous, that is the solution φ must depend continuously on the data f. The last condition guarantees that small perturbations in the measured data will cause small errors in the solution of the problem. However, for most inverse scattering problems, this condition can not be satisfied, and hence these problems are clasified as ill-posed problems. Typically, completely continuous operator equations of the first kind are ill-posed [2]. The linearized form of the reduced data equation (2.52), which is a Fredholm integral equation of the first kind, involves linear compact operators. As the linear compact operators are continuous, the inverse problem that is analysed in this thesis is ill-posed [2]. The ill-posedness implies that a straightforward inversion will result in an instable solution with a large error, since the measured data is assumed to contain random noise. Therefore, special techniques, called regularization methods, should be used to obtain a stable approximate solution of the inverse problem [2].

The regularization methods aims to solve the equation (2.65) for a right hand side with error denoted as f^δ, satisfying

$$\left| f^\delta - f \right| \leq \delta \qquad (2.66)$$

where δ is the error level [2]. It is clear that the solution φ^δ of the equation with f^δ will be an approximate solution. To obtain this stable approximate solution the inverse operator A^{-1} must be replaced by an approximate linear operator $R:Y \to X$ [2]. That is, for the normed spaces of X, Y and the bounded linear operator $A:X \to Y$; a family of bounded linear operators $R_\alpha :Y \to X$, $\alpha > 0$, with the property

$$\lim_{\alpha \to 0} R_\alpha A\varphi = \varphi \tag{2.67}$$

for all $\varphi \in X$, is a regularization scheme for A; here α is the regularization parameter [2]. It is from (2.67) that the approximate solution φ^δ is given by

$$\varphi^\delta = R_\alpha f^\delta \tag{2.68}$$

Considering (2.66) and (2.68), the resulting error can be stated as

$$\left\| \varphi^\delta - \varphi \right\| \leq \delta \left\| R_\alpha \right\| + \left\| R_\alpha A\varphi - \varphi \right\| \tag{2.69}$$

The first term in the right hand side of (2.69) shows the effect of the perturbations in the measured data, and the second term is the result of the replacing inverse operator A^{-1} with the regularization sheme R_α. As for $\alpha \to 0$, $R_\alpha \to A^{-1}$; the second part of the error decreases for smaller values of the regularization parameter α [2]. However, this choice will increase the instability of the solution, and hence will result in an increase in the first part of the error [2]. Different criteria, such as Morozov's discrepancy principle, are used to choose an optimal value for α. In the solution of the inverse problem analysed in this thesis, we have chosen to decrease the value of α in each step of the iterative process. This decision is based on the assumption that in each step the difference between the actual and the approximate solutions will decrease, and therefore the stability of the solution will increase. Since a lower value of α increases the accuracy, whereas a higher value improves the stability; it is safe to assume that relatively smaller values of α will be more beneficial as the number of iterations increases. The initial value of α is determined by trial and error.

Finally, before concluding this sub-section, we will introduce the formal definition of the well-known Tikhonov regularization scheme that will be employed in the solution of the inverse problem in the following sections. The theorem states that for a compact linear operator $A: X \to Y$, the operator $\alpha I + A^* A: X \to X$ is bijective for $\alpha > 0$, and has a bounded inverse [2]. Here, I is the identity operator, and A^* is the adjoint of the operator of the A. More importantly, if A is injective, then

$$R_\alpha = (\alpha I + A^* A)^{-1} A^* \tag{2.70}$$

41

describes the Tikhonov regularization scheme [2]. (2.70) will be used as the regularization technique in the Newton based iterative inversion algorithm, which will later be used in the solution of the 1-D profile inversion problem.

It should be noted that the reduced data equation (2.52) is a non-linear equation. The Newton's method involves replacing a non-linear equation denoted as [2]

$$F(v) = u^s \qquad (2.71)$$

by a linearized equation

$$F(v) + F'q = u^s \qquad (2.72)$$

The details of this procedure will be explained in the next section. In (2.72), F' denotes the Fréchet derivative of the completely continuous operator F. As stated in [2], for a completely continuous, Fréchet differentiable operator F, the derivative F' is also compact. Therefore, the linearized equation (2.72) involves compact operators, and hence it is ill-posed [2]. In conclusion, the ill-posedness is not affected by the linearization, and regularization techniques will be used in the Newton based solution scheme that will be developed in the next section.

2.3.2 The solution of the inverse scattering problem

In the first part of this section the 1-D profile inversion problem will be formulated. The formulation will be based on the configuration of the direct scattering problem, which is already presented in the previous sections. The measurement domain and the method to obtain data for the inversion procedure will also be specified in this part. In the second part of the section, a Newton based iterative solution will be developed in order to reconstruct the unknown acoustic profile of the spherical scatterer. The solution will involve the linearization of the non-linear system formed by the equations (2.51)-(2.52) according to the principles explained in the previous sub-section.

2.3.2.1 Formulation of the problem

Consider the geometry given in Fig. 2.16. Similar to the direct scattering problem, the sphere with radius a is illuminated by a time harmonic point source located at the point (r_s, θ_s, ϕ_s), $r_s > a$. The density ρ_0 is considered constant throughout the whole

42

space, and the outside region is characterized by a constant wave number $k_0 = \omega\sqrt{b_0\rho_0}$

The compressibility inside the sphere, denoted as $b(r)$, is a function of the radial distance only, and it constitutes the unknown of the inverse scattering problem.
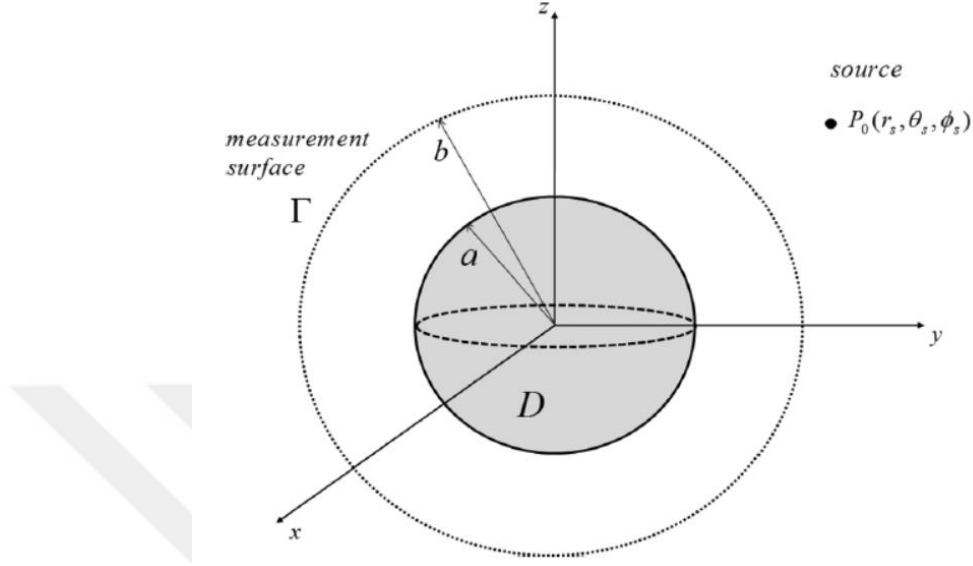
Figure 2.16 : The geometry of the inverse scattering problem.

The scattered field is assumed to be measured on a spherical surface denoted by Γ with radius b, $b > a$. Therefore, the aim of the 1-D profile inversion problem is to reconstruct the unknown object function $v(r)$ via the measurement of the scattered field on the surface Γ outside the sphere. Considering this formulation, the reduced integral equations that defines the problem will be restated here for the sake of presentation:

$$\hat{u}_{nm}(r) = \hat{u}_{nm}^i(r) + ik_0^3 \int_0^a j_n(k_0 r_<)h_n^{(1)}(k_0 r_>)v(r')\hat{u}_{nm}(r')r'^2 dr' \qquad r < a \tag{2.73}$$

$$\hat{u}_{nm}^s(b) = ik_0^3 h_n^{(1)}(k_0 b)\int_0^a j_n(k_0 r')v(r')\hat{u}_{nm}(r')r'^2 dr' \qquad r = b \tag{2.74}$$

As stated before, (2.73) is the reduced object equation, and (2.74) is called as the reduced data equation. Note that the data equation is defined on the measurement domain Γ. (2.73) and (2.74) form a non-linear system of equations for the unknowns $v(r)$ and $\hat{u}_{nm}(r)$, since the coefficients of the interior field $\hat{u}_{nm}(r)$ are themselves dependent on $v(r)$, as seen in (2.73). Therefore, the solution should involve a

linearization technique; and as declared before, a Newton based iterative scheme will be formulated in the next sub-section in order to determine the object function $v(r)$. However, it should be noted that, in this formulation the coefficients of the scattered field $\hat{u}_{nm}^s(b)$ constitute the measured data of the inverse problem instead of the measured field itself. Since those coefficients cannot be measured directly, they should be evaluated using the measured value of the scattered field on the spherical surface Γ. Using the integration defined in (2.15) for series expansion coefficients, $\hat{u}_{nm}^s(b)$ can be obtained as

$$\hat{u}_{nm}^s(b) = \int_0^{2\pi} \int_0^\pi u^s(b,\theta,\phi)\, P_n^{|m|}(\cos\theta)\, e^{-im\phi} \sin\theta\, d\theta d\phi \tag{2.75}$$

where $u^s(b,\theta,\phi)$ represents the actual scattered field measured on Γ. In practical applications, the scattered field can be measured on a finite number of points, and therefore the integral in (2.75) should be evaluated numerically. In the numerical simulations, we used the Simpson's rule for the evaluation of the integral over the spherical surface. At this point, the non-linear system of equations and the data that will be used in the inversion process have been introduced. Therefore, in the next sub-section, the Newton based iterative scheme will be developed.

2.3.2.2 Newton based iterative solution

In order to present the iterative scheme, let us write (2.73) and (2.74) in a more compact form similar to (2.71):

$$K\hat{u} = \hat{u}^i \tag{2.76}$$

$$Lv = \hat{u}^s \tag{2.77}$$

where the operators K and L are defined as

$$K\hat{u} = \hat{u} - ik_0^3 \int_0^a j_n(k_0 r_<) h_n^{(1)}(k_0 r_>) v(r') \hat{u}_{nm}(r') r'^2 dr' \tag{2.78}$$

$$Lv = ik_0^3 h_n^{(1)}(k_0 b) \int_0^a j_n(k_0 r') v(r') \hat{u}_{nm}(r') r'^2 dr' \tag{2.79}$$

Then, we begin the iterative process by choosing an initial guess, denoted as $v^{(0)}(r)$, for the object function. The reduced object equation (2.73) can be solved using this initial guess in order to obtain the initial values of the coefficients of the interior field, that is $\hat{u} = \hat{u}^{(0)}(r)$. This step is identical to the solution of the direct scattering problem, and in the compact notation of (2.76)-(2.77), it corresponds to the inversion of the operator $[I - K]$. Here, I represents the identity matrix with appropriate dimensions. After solving the direct scattering problem via (2.76), the non-linear data equation (2.77) is linearized by expanding the operator L into a Taylor series around the initial guess $v^{(0)}$:

$$Lv^{(0)} + L_{\partial}\delta v(r) = \hat{u}^s \tag{2.80}$$

Note that the resulting equation is of the same form as (2.72). In (2.80), $\delta v(r)$ is the update amount of the object function $v(r)$. Therefore, the aim is to solve linearized equation (2.80) for $\delta v(r)$, in order to update the initial guess $v^{(0)}(r)$. Here, L_{∂} is the Fréchet derivative of the operator L, which is defined as

$$L_{\partial}\delta v = ik_0^3 h_n^{(1)}(k_0 b) \int_0^a j_n(k_0 r')\delta v(r')\hat{u}_{nm}^{(0)}(r')r'^2 dr' \tag{2.81}$$

Now, the update amount $\delta v(r)$ can be obtained by solving (2.80) via inversion of the equation

$$L_{\partial}\delta v = \hat{u}^s - Lv^{(0)} \tag{2.82}$$

However, as stated in the previous section, the Fréchet derivative L_{∂} is a compact operator and (2.82) is ill-posed. Therefore, the Tikhonov regularization will be used to obtain a stable solution for the inversion process. Considering the formulation given in (2.70), the expression for the update amount is determined as

$$\delta v^{(1)} = (\alpha I + L_{\partial}^* L_{\partial})^{-1} L_{\partial}^*(\hat{u}^s - Lv^{(0)}) \tag{2.83}$$

Here, α is the regularization parameter, and L_{∂}^* is the conjugate transpose of the matrix form of the operator L_{∂}. Note that the matrix elements of the operators are

obtained by discretizing the integrals according to the point matching technique. That is, similar to solution of the direct scattering problem, the unknowns $v(r)$ and $\hat{u}(r)$ are assumed to have constant values at each sub-domain of the integration domain $r \in [0, a]$. Finally, at the end of each iterative step, the object function is updated using the equation

$$v^{(1)} = v^{(0)} + \delta v^{(1)} \tag{2.84}$$

Another important parameter of the Newton's method is the stopping threshold for the iterative process. In this thesis, the iterative process is continued until the condition

$$\left\| \frac{\delta v^{(j)}}{v^{(j)}} \right\| < \varepsilon \tag{2.85}$$

is satisfied. Here, ε is a pre-determined threshold, and $\left\| \delta v^{(j)} / v^{(j)} \right\|$ is the ℓ^2 norm of the ratio $\delta v^{(j)} / v^{(j)}$ at the j th iteration.

2.3.3 Numerical simulations

In order to test the validity of the inversion scheme developed in the previous section, numerical tests involving spherical scatterers with various profiles have been performed. In all simulations, the sphere is assumed to have a radius of $a = 0.1 m$, and it is illuminated by a time-harmonic point source located at the point $r_s = 0.25$, $\theta_s = \pi / 3$, $\phi_s = \pi / 2$. The measurement surface Γ, is chosen as the spherical surface with radius $b = 0.2 m$. It should be noted that in order to avoid inverse crime, the scattered field is synthetically produced via MoM, following the formulation given in the Appendix C. Furthermore, a random term of $0.05 |u^s| e^{i2\pi r_n}$ is added to the scattered field to model a more realistic measurement scenario with 5% noise level. Here, r_n's are normally distributed random numbers. The coefficients of the scattered field which constitute the data of the inverse problem are obtained by substituting this noise-added scattered field into the integral given in (2.75). The integrals in the reduced object and data equations are discretized by 30 points in all configurations. As demonstrated in the examples for the direct scattering problem, this choice yields satisfactory results for a reasonably large frequency range.

In the first part of this section, the overall performance of the method will be tested using piecewise homogeneous and continuous profiles. In order to demonstrate the robustness of the method, same parameters will be used for different scenarios. In the second part, the effect of these parameters (e.g. regularization parameter, stopping threshold) on the success of the method will be analysed using different profiles. The dependence of the results on operating frequency will also be demonstrated in the same part.

2.3.3.1 Performance evaluation of the method

In this sub-section, numerical simulations involving four different profiles (two layered piecewise homogeneous, Luneburg lens, sinusoidally varying, and linearly varying) will be presented in order to demonstrate the validity of the inversion method. As stated above, the tests will be performed using identical parameters for all profiles to show the versatility of the inversion scheme. Therefore, for all simulations in this sub-section, the region outside the sphere is assumed to be characterized by the wave number $k_0 = 8\pi$. The number of terms included in the series expansions for the field values is chosen as $N_{max} = 3$. Note that adding more term increases not only the computational cost of each iterative step, but also the instability of the inversion scheme. Therefore, N_{max} can also be considered as an additional regularization parameter. The remaining parameters of the Newton based method, namely the Tikhonov regularization parameter α and the stopping threshold ε, are chosen according to the principles explained in the previous sections. Choosing lower values for α increases both the accuracy of the inversion, and the instability of the solution. As the ill-posedness of the inversion operation is assumed to decrease in each step, smaller values of α would be more suitable as the number of iteration increases. Therefore, in all configurations the regularization parameter is determined as $\alpha = 0.1/i_n$, i_n being the number of iterations. The stopping threshold for the iterative process is chosen as $\varepsilon = 10^{-3}$, that is the procedure is continued until the ℓ^2 norm of the ratio $\delta v^{(j)}/v^{(j)}$ becomes smaller than 10^{-3}. The convergence history graph of the ℓ^2 norm $\left\| \delta v^{(j)}/v^{(j)} \right\|$ versus the number of iterations is presented in Fig. 2.17 for each investigated profile. In the figure, the ℓ^2 norms are given in logarithmic scale in order to better depict the variations in smaller scales. For each case in this section, the actual

profile will be reconstructed using three different initial guesses $v^{(0)}(r)$ for the object function. As a measure of the performance of the method, an ℓ^2 error metric

$$e_{\ell^2} = \frac{\|v_{rec} - v_{exact}\|}{\|v_{exact}\|}$$

(2.86)

is defined using the exact and reconstructed profiles.
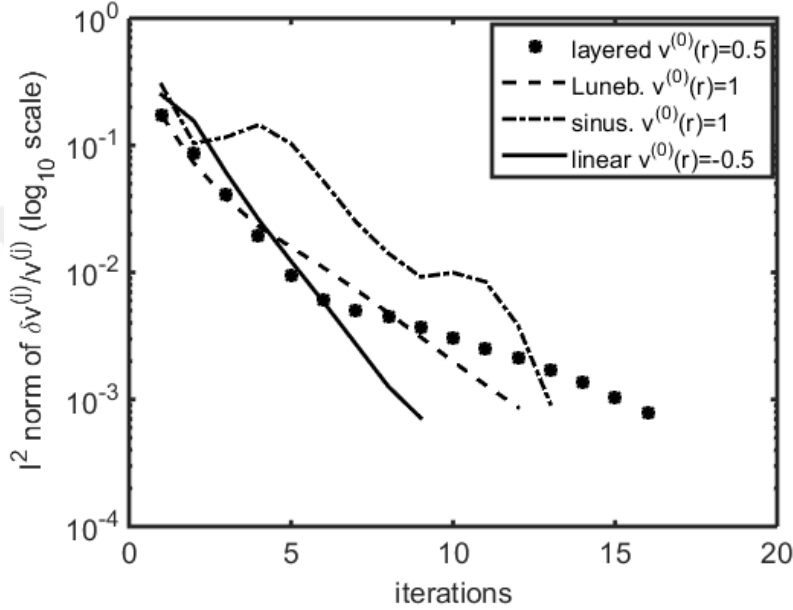
Figure 2.17 : The convergence history graph of the ℓ^2 norm of $\delta v^{(j)}/v^{(j)}$ (in logorithmic scale) for four different profiles.

As a first example, the two layered piecewise homogeneous sphere defined in (2.63) will be analysed. The three different initial guesses are chosen as $v^{(0)}(r) = 0.4$, $v^{(0)}(r) = 0.5$, and $v^{(0)}(r) = 0.6$. For these values, the iterative process lasted for 18, 16, and 12 iterations respectively. As the exact and reconstructed profiles depicted in Fig. 2.18 suggest, although the method is not capable of catching the sharp transition, it nonetheless provides a smoothed approximation of the actual profile. This is an expected result, considering that we are trying to approximate a piecewise continuous functions via pulse basis functions. This also explains the relatively low rate of convergence for the two layered profile compared to the continuous profiles as seen in Fig. 2.17. The lowest error metric is obtained as $e_{\ell^2} = 0.16$ for the optimal initial guess of $v^{(0)}(r) = 0.5$. The error increases to $e_{\ell^2} = 0.18$ for $v^{(0)}(r) = 0.6$, and to $e_{\ell^2} = 0.23$

for $v^{(0)}(r) = 0.4$. This results demonstrate that the success of the method is dependent on the choice of the initial guess. It should be also noted that, when the initial guess further diverges from the optimal value, the method fails to converge to a meaningful result. This is a common problem for Newton based algorithms.
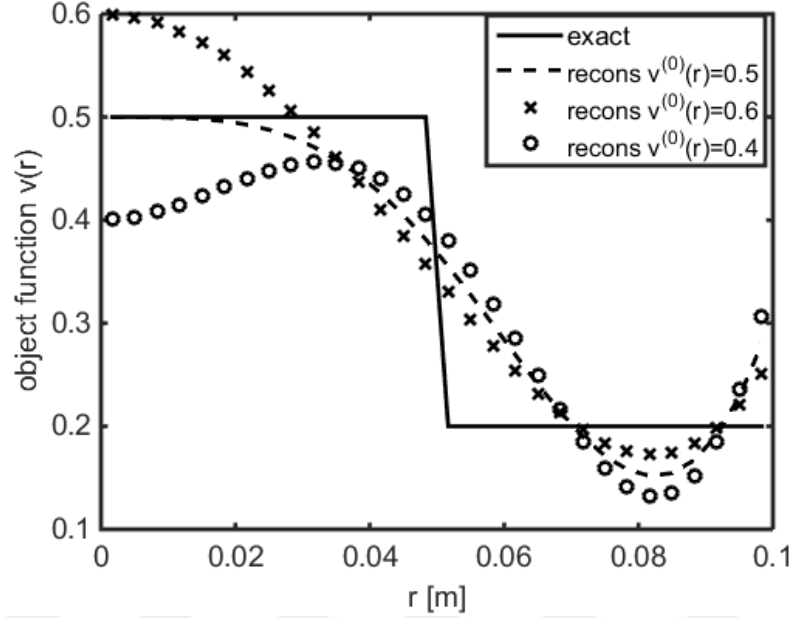
Figure 2.18 : Exact and reconstructed values of the object function for a two layered sphere with three different initial guesses.

In the second example, the profile of the Luneburg lens described by

$$\frac{b(r)}{b_0} = 2 - \left(\frac{r}{a}\right)^2$$

(2.87)

will be reconstructed using the initial guesses of $v^{(0)}(r) = 0.75$, $v^{(0)}(r) = 1$, and $v^{(0)}(r) = 1.25$. The results are obtained in 12 iterations for $v^{(0)}(r) = 1$, and in 13 iterations for $v^{(0)}(r) = 0.75$ and $v^{(0)}(r) = 1.25$. The results presented in Fig. 2.19 demonstrate that for slowly varying smooth profiles, the method is very effective. For the initial estimate of $v^{(0)}(r) = 1$, the error is calculated as $e_{\ell^2} = 9.1 \times 10^{-3}$. Expectedly, as the initial guess deviates from the optimal value, the error starts to increase. For $v^{(0)}(r) = 0.75$, the error metric is obtained as $e_{\ell^2} = 0.16$, and for $v^{(0)}(r) = 1.25$ as $e_{\ell^2} = 0.13$. Nevertheless, these values show that the method performs better for smooth profiles, even with sub-optimal guesses, compared to piecewise homogeneous

profiles. The relatively rapid convergence of ℓ^2 norm for Luneburg lens seen in Fig. 2.17 also proves the efficiency and the reliability of the method for slowly varying continuous profiles.
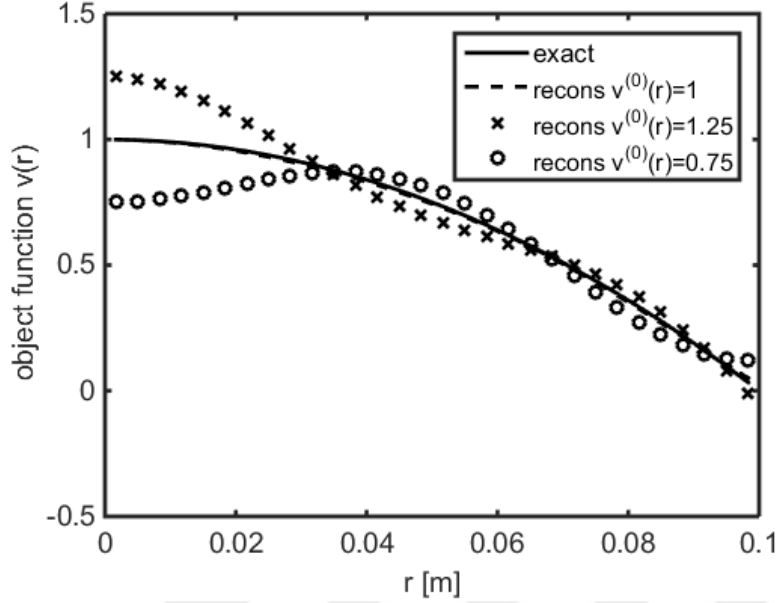
Figure 2.19 : Exact and reconstructed values of the object function for the Luneburg lens with three different initial guesses.

For the third example, the method is used to reconstruct a sinusiodally varying profile described by

$$\frac{b(r)}{b_0} = 1.5 + 0.5\cos\left(\frac{3\pi r}{a}\right) \qquad (2.88)$$

In this case, the initial guesses for the object function are chosen as $v^{(0)}(r) = 0.75$, $v^{(0)}(r) = 1$, and $v^{(0)}(r) = 1.25$. The results presented in Fig. 20 shows that the method is capable of reconstructing an approximate oscillating profile, however, the error is much larger compared to the slowly varying profile of the Luneburg lens. This results demonstrate that rapid variation of the profile restricts the success of the reconstruction process, even for continuous profiles. The error metrics are calculated as $e_{\ell^2} = 0.22$ for $v^{(0)}(r) = 1$, and $e_{\ell^2} = 0.23$ for the other two guesses. The close values of error metrics, and the relatively irregular convergence curve in Fig. 2.17 are also caused by the rapid oscillation of the profile. However, it should be noted that the error level is not independent of the initial guess. Similar to the previous cases, it increases as the

initial value differs from the optimal value of $v^{(0)}(r)=1$. For example, when the initial guess is chosen as $v^{(0)}(r)=1.5$, the method still produces a relevant result, however, the error increases to $e_{\ell^2}=0.35$. For more rapidly oscillating profiles, the method either diverges or needs more iterations to converge.
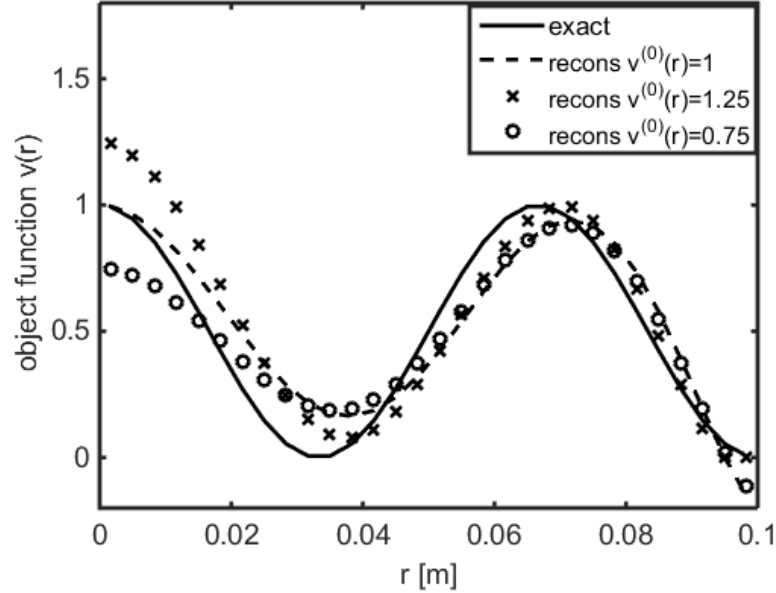
Figure 2.20 : Exact and reconstructed values of the object function for a sphere described by $b(r)/b_0 = 1.5 + 0.5\cos(3\pi r / a)$ with three different initial guesses.

When the compressibility of the outside region is greater than the compressibility inside the inhomogeneous sphere, the object function takes negative values. To test the performance of the method in this type of configurations, we analyse a linearly varying profile described by

$$\frac{b(r)}{b_0} = 0.5 + 0.5\frac{r}{a} \tag{2.89}$$

as the fourth example. For this case, the initial guesses are chosen as $v^{(0)}(r)=-0.4$, $v^{(0)}(r)=-0.5$, and $v^{(0)}(r)=-0.6$. The results presented in Fig. 2.21 demonstrate that the method is also useful in the configurations involving scatterers with compressibility smaller than the outside medium. As expected for a slowly varying smooth profile, the error is relatively low. The metrics are calculated as $e_{\ell^2}=0.08$ for $v^{(0)}(r)=-0.5$, $e_{\ell^2}=0.11$ for $v^{(0)}(r)=-0.4$, and $e_{\ell^2}=0.19$ for $v^{(0)}(r)=-0.6$. For

similar reasons, the result for the optimal guess of $v^{(0)}(r) = -0.5$ converges faster than the other profiles as seen in Fig. 2.17. However, for the remaining sub-optimal guesses the convergence rate, presented in Fig. 2.22, drops significantly. This further emphasizes that not just the accuracy but also the efficiency of the method depends on the initial guess. On the other hand, it should be noted that similar drops in the convergence rate do not occur for sub-optimal guesses of the other profiles analysed in this section. In conclusion, due to the ill-posed nature of the problem, the convergence rate is not entirely predictable.

Figure 2.21 : Exact and reconstructed values of the object function for a sphere described by $b(r)/b_0 = 0.5 + 0.5(r/a)$ with three different initial guesses.

From these examples, it is concluded that the method is reliable for continuous profiles, and provides a useful approximation for a piecewise homogeneous layered profile. However, the success of the method is clearly dependent on the choice of initial guess, which is an expected result for a Newton based iterative scheme. Another limitation that should be mentioned is the limitation on the contrast value of the scatterer. When the contrast between the compressibility of the sphere, and that of the outside region becomes too large, the method fails to produce useful results. Since the non-linearity increases significanly for profiles with large contrasts, the linearization procedure becomes inadequate for these cases. The last point to consider, that is the effect of the initial parameters on the outcome, will be analysed in the next sub-section.
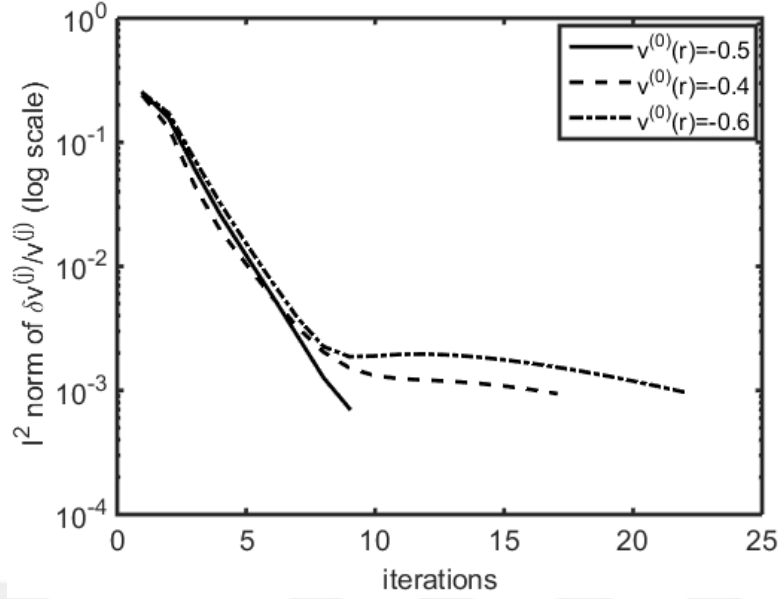
Figure 2.22 : The convergence history graph of the ℓ^2 norm of $\delta v^{(j)} / v^{(j)}$ (in log scale) for three different initial guesses $v^{(0)}(r)$. The sphere has a linearly varying profile described by $b(r)/b_0 = 0.5 + 0.5(r/a)$.

2.3.3.2 The effect of the initial parameters

In this sub-section, the effects of four different initial parameters (k_0, $N_{\max}$, α, and ε) on the performance and the outcome of the method will be investigated. In order to analyse each parameter seperately, a single parameter will be altered for each configuration. For the remaining parameters, the values that are used in the previous sub-section ($k_0 = 8\pi$, $N_{\max} = 3$, $\alpha = 0.1/i_n$, $\varepsilon = 10^3$) will remain unchanged. Different profiles will be used in each case to avoid repetition, and to emphasize the particular effects of the related parameters.

First, in order to analyse the effect of the operating frequency, the two layered sphere defined in (2.63) will be reconstructed using different values for k_0. The results obtained for three different values, $k_0 = 4\pi$, $k_0 = 8\pi$, and $k_0 = 12\pi$, are plotted in Fig. 2.23. For all simulations, the initial value of the object function is chosen as $v^{(0)}(r) = 0.5$. Note that the electrical size of the spherical scatterer is determined by the term $k_0 a$. Therefore, changing the operating frequency, and thus the value k_0, is equivalent to changing the radius of the sphere. The result for $k_0 = 4\pi$ shows that, for this value, the size of the sphere is too low for a meaningful reconstruction. On the

53

other hand, as the frequency increases, the reconstructed profile starts to reflect the actual profile. For $k_0 = 12\pi$, the error is calculated as $e_{\ell^2} = 0.12$, which is lower than the previously calculated error for $k_0 = 8\pi$. However, further increase in the electrical size negatively effects the performance of the method. Although the result is not shown here, the error for $k_0 = 16\pi$ is obtained as $e_{\ell^2} = 0.15$. More importantly, as shown in Fig. 2.24, the result significantly diverges from the actual profile for $k_0 = 20\pi$. Note that this result is obtained in 85 iterations. For even higher values, the method fails to converge. Considering the relation between the electrical size and the term $N_{\max}$, analysed in the direct scattering section, one might argue that increasing the value of $N_{\max}$ could improve the performance of the method for higher frequency. However, as it will be demonstrated below, the regularizing effect of $N_{\max}$ is crucial, and an increase in this value causes the method to further diverge due to the ill-posedness. These results demonstrate that an optimal value for k_0 must be found to maximize the performance of the method. However, it should be noted that this optimal value might be different for different profiles.
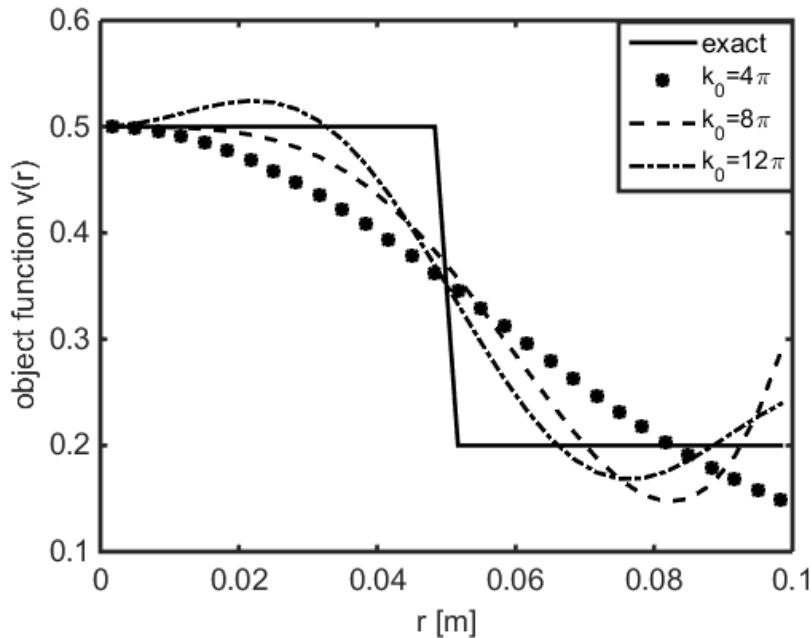
Figure 2.23 : Exact and reconstructed values of the object function for a two layered sphere with three different k_0 values.
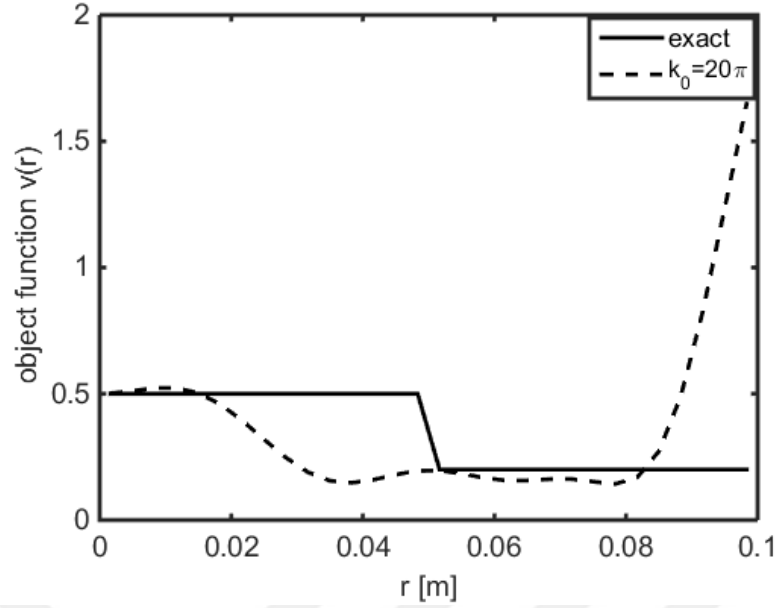
Figure 2.24 : Exact and reconstructed values of the object function for a two layered sphere with $k_0 = 20\pi$.

As a second case, the effect of N_{max}, the number of terms included in the series expansions, will be analysed using the linearly varying profile defined in (2.89). The initial guess of the object function is determined as $v^{(0)}(r) = -0.5$. The exact and reconstructed profiles for $N_{max} = 1$ and $N_{max} = 2$ are presented in Fig. 2.25. Note that the lowest order term of the series is denoted by the index $n = 0$, therefore, for $N_{max} = 1$, the terms with indices $n = 0$ and $n = 1$ are included. As demonstrated in Fig. 2.9, the lower order terms make the greatest contribution to the final result. Thus, even for $N_{max} = 1$, the method produces a useful approximation. The error for this case is calculated as $e_{\ell^2} = 0.11$. On the other hand, adding more terms still improves the results at this point. For $N_{max} = 2$, the error metric is determined as $e_{\ell^2} = 0.09$. In Fig. 2.26, the results for $N_{max} = 3$ and $N_{max} = 4$ is given. From the comparison with the previous figure, it is clear that the variation of the reconstructed profile, that is the fitting ability, increases with the number of terms. However, after the optimal value of $N_{max} = 3$, the error starts to increase due to the over-fitting. For $N_{max} = 4$, the error is calculated as $e_{\ell^2} = 0.10$, whereas it was determined as $e_{\ell^2} = 0.08$ for $N_{max} = 3$. Moreover, for $N_{max} = 4$, the results are obtained in 18 iterations. These results demonstrate that the perturbance caused by the added noise in the data is especially

effective on the higher order terms, and adding more terms increases the instability of the problem. Indeed, the method fails to converge for $N_{max} = 5$. It is clear that N_{max} acts as an additional regularization parameter, and even relatively low values are adequate to produce useful results, especially for slowly varying profiles.

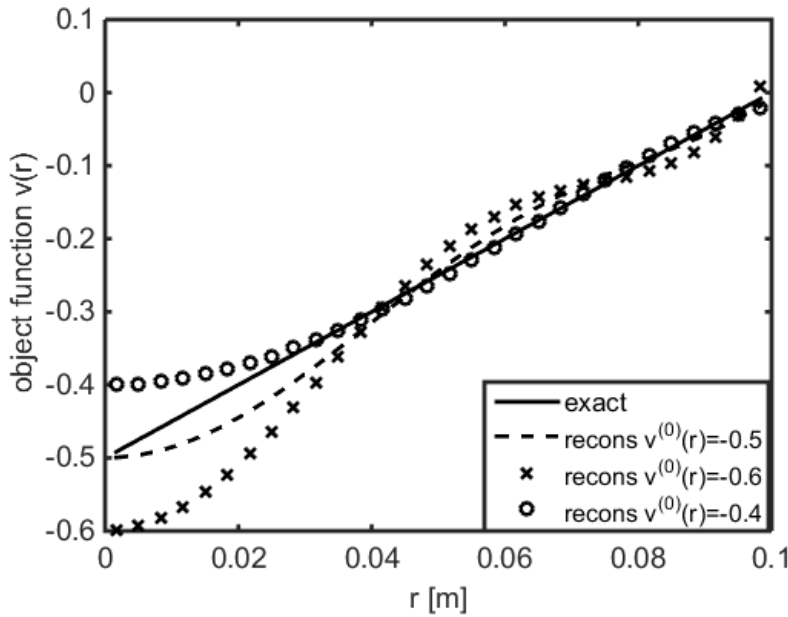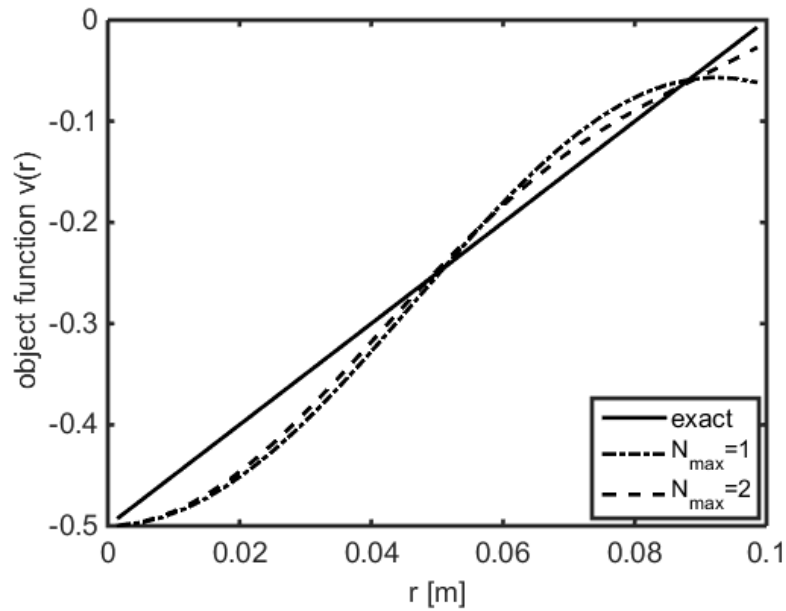**Figure 2.25 :** Exact and reconstructed values of the object function for a sphere described by $b(r)/b_0 = 0.5 + 0.5(r/a)$ with $N_{max} = 1$ and $N_{max} = 2$.
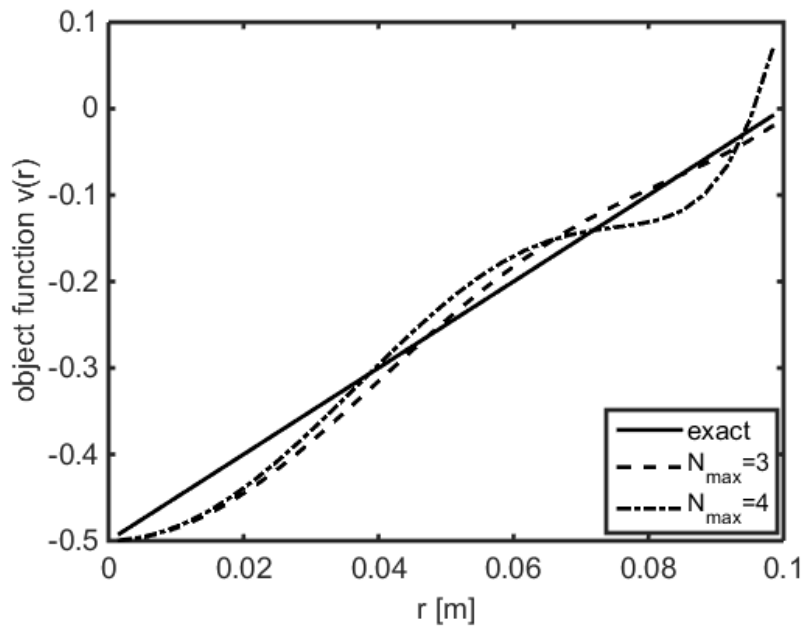
Figure 2.26 : Exact and reconstructed values of the object function for a sphere described by $b(r)/b_0 = 0.5 + 0.5(r/a)$ with $N_{max} = 3$ and $N_{max} = 4$.

One of the most important parameter of the inverse problems is the regularization parameter α. As stated in the section 2.3.1, in this thesis, it has been determined by trial and error, instead of Morozov's principle, for the sake of practicality. Since the error level is strongly affected by this parameter, as a third case, sinusoidally varying profile defined in (2.88) is reconstructed using different values for α. First, in order to test the assumption that smaller values will be more beneficial as the number of iterations increase, we have reconstructed the profile using $\alpha = 0.1/i_n$, and the constant value of $\alpha = 0.1$. The comparison of the results presented in Fig. 2.27 demonstrate that the reconstruction for $\alpha = 0.1/i_n$ is more accurate compared to the reconstruction with constant value. The error $\alpha = 0.1/i_n$ is measured as $e_{\ell^2} = 0.23$, whereas for $\alpha = 0.1$ the value is calculated as $e_{\ell^2} = 0.39$. Clearly, lower regularization parameters increased the accuracy of the inversion procedure, while maintaining the stability. To better elucidate this point, in Fig. 2.28, higher values have been used for the reconstruction. Defining the regularization parameter as $\alpha = 0.5/i_n$ actually improved the result, the error for this case is calculated as $e_{\ell^2} = 0.19$. However, it should be noted that the iterative process lasted for 34 iterations. This is an expected result considering that higher values of α slowed the convergence initially by increasing the error in the inversion procedure. On the other hand, this choice also increased the stability of the problem. It should be noted that the possibility of obtaining a significantly divergent result, which is caused by the ill-posedness of the problem, diminishes considerably for larger values of α. The result for $\alpha = 0.5$ demonstrates this point. Although the accuracy is too low, the method nevertheless converged to a useful solution in 9 iterations. These examples suggest that lowering the value of α in each iteration is a sensible strategy for this inversion scheme. However, when the initial value of α is too low, further decrease might cause the regularization scheme to fail to stabilize the problem. In this case, the outcome will be a divergent result like the one presented in Fig. 2.29 for $\alpha = 0.01/i_n$. This result is obtained in 119 iterations. It is clear that the error caused by the instability was the dominant factor in this case. On the other hand, the fixed value of $\alpha = 0.01$ produced the best recontruction for the sinusoidally varying profile. The error for this value is calculated as $e_{\ell^2} = 0.08$. Although this result suggests that a low constant value for α might be the best choice, further tests with close values demonstrate the

unpredictability of the outcome. For the constant value of $\alpha = 0.05$, the error is calculated as $e_{\ell^2} = 0.33$. Similarly, reconstruction with the even smaller value of $\alpha = 0.001$ yielded an error of $e_{\ell^2} = 0.38$. In conclusion, choosing an optimal value for α is a highly challenging task, and requires numerous simulations for each profile.
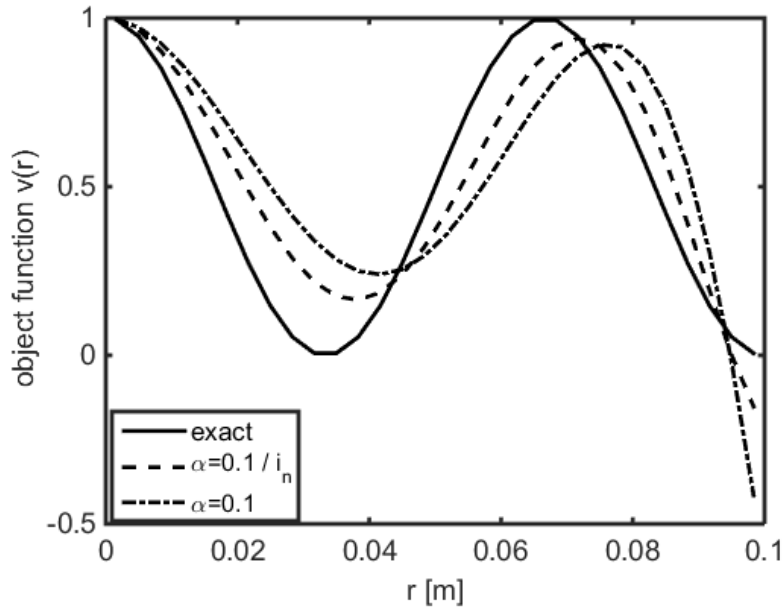
Figure 2.27 : Exact and reconstructed values of the object function for a sphere described by $b(r)/b_0 = 1.5 + 0.5\cos(3\pi r/a)$ with $\alpha = 0.1/i_n$ and $\alpha = 0.1$.
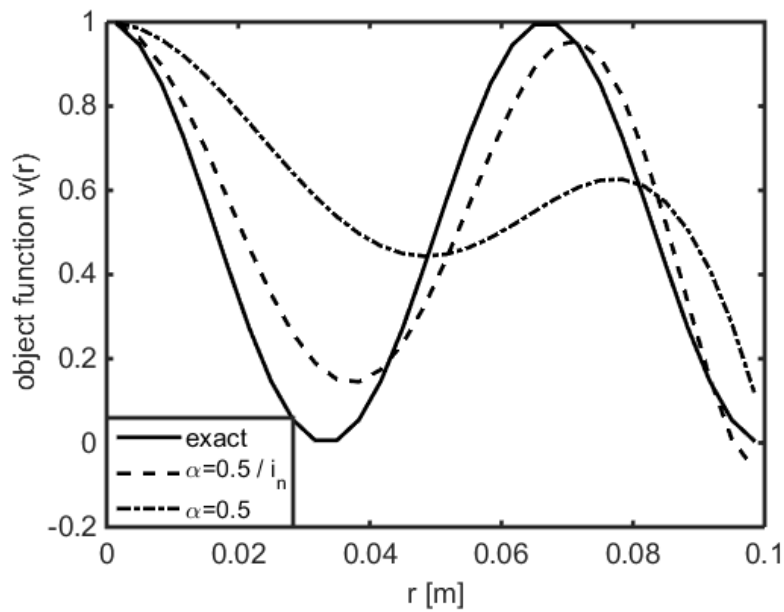
Figure 2.28 : Exact and reconstructed values of the object function for a sphere described by $b(r)/b_0 = 1.5 + 0.5\cos(3\pi r/a)$ with $\alpha = 0.5/i_n$ and $\alpha = 0.5$.
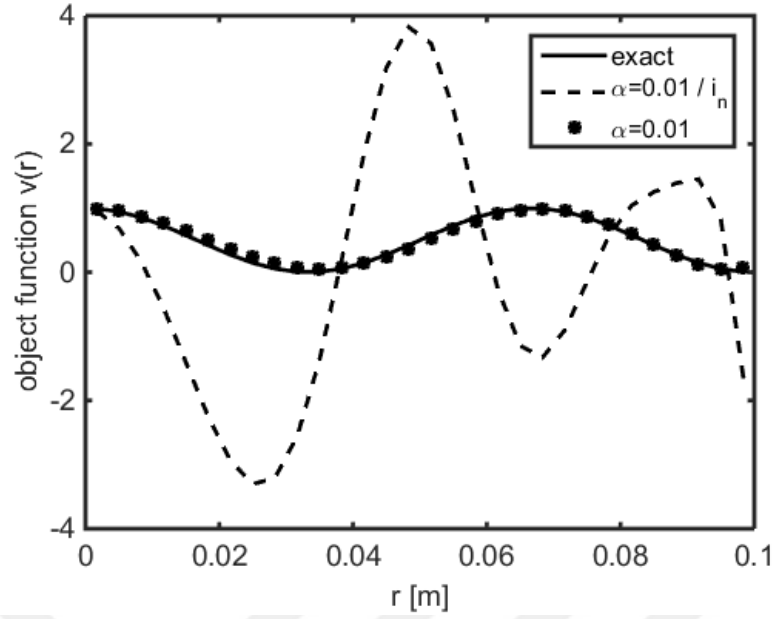
Figure 2.29 : Exact and reconstructed values of the object function for a sphere described by $b(r)/b_0 = 1.5 + 0.5\cos(3\pi r/a)$ with $\alpha = 0.01/i_n$ and $\alpha = 0.01$.

Finally, the effect of the stopping threshold ε is analysed using the Luneburg lens defined in (2.87). The effect of choosing a higher value for ε is predictable. The accuracy of the result would be expected to drop alongside the number of iterations. Indeed, although the results are not presented here, reconstruction with a threshold of $\varepsilon = 10^{-2}$ yielded a slightly higher error level of $e_{\ell^2} = 0.02$ compared to the previous simulation with $\varepsilon = 10^{-3}$. On the other hand, the number of iterative steps decreased to 7 iterations. However, lowering the value of ε does not always result in a more accurate reconstruction. In Fig. 2.30, the reconstructions of the Luneburg lens using the thresholds $\varepsilon = 10^{-3}$ and $\varepsilon = 10^{-6}$ are compared with the actual profile. It is clear from the figure that $\varepsilon = 10^{-3}$ provided a better reconstruction. The error for $\varepsilon = 10^{-6}$ is calculated as $e_{\ell^2} = 0.05$, which is higher than the values obtained by using $\varepsilon = 10^{-3}$ or $\varepsilon = 10^{-2}$. As the figure suggests a prolonged iterative process causes unnecessary variations in the reconstructed profile. More importantly, as the convergence history graph presented in Fig. 2.31 demonstrates, the convergence rate drops significantly when the threshold is too low. The iterative process lasted for 192 iterations in this case. It should be noted that for rapidly varying profiles, the method fails to produce a result for the threshold of $\varepsilon = 10^{-6}$. Even for the slowly varying linear profile, the result converged in 418 iterations, and yielded an error of $e_{\ell^2} = 0.12$, a slightly higher

value than the one obtained with the threshold $\varepsilon = 10^{-3}$. These results show that, like other parameters, an optimal value must be chosen for ε in order to increase the performance of the reconstruction process. In conclusion, the outcome of the method developed in this thesis is highly dependent on the choice of the initial parameters.
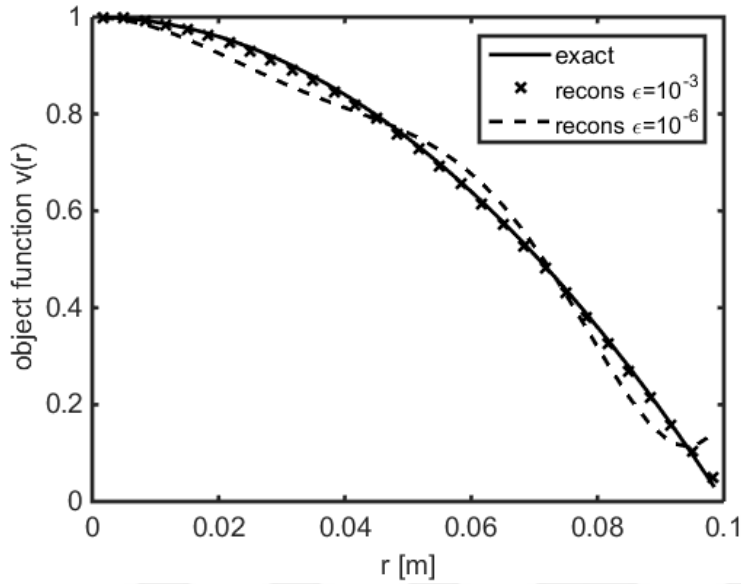
Figure 2.30 : Exact and reconstructed values of the object function for the Luneburg lens with $\varepsilon = 10^{-3}$ and $\varepsilon = 10^{-6}$.
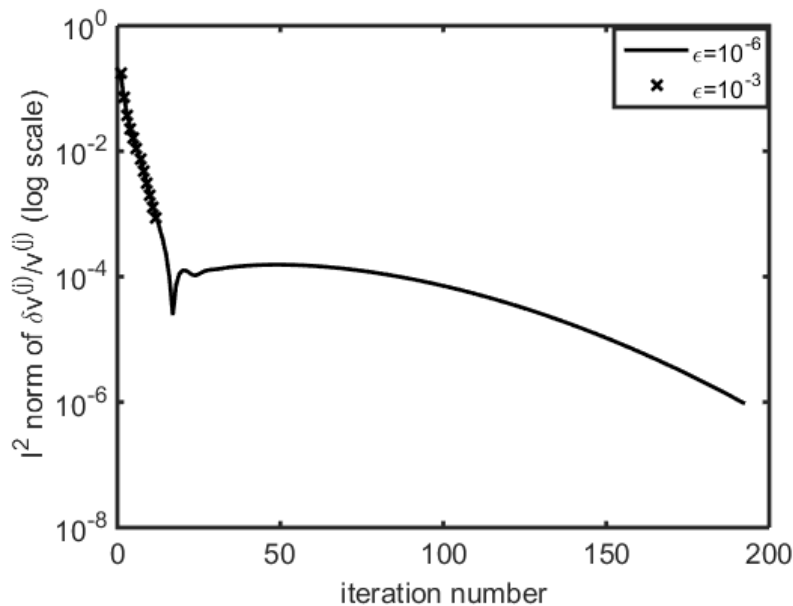
Figure 2.31 : The convergence history graph of the ℓ^2 norm of $\delta v^{(j)}/v^{(j)}$ (in logarithmic scale) for the Luneburg lens with $\varepsilon = 10^{-3}$ and $\varepsilon = 10^{-6}$.

3. ELECTROMAGNETIC CASE

3.1 Purpose

In this section, the electromagnetic direct and inverse scattering problem related to radially inhomogeneous spheres will be analysed. Similar to the acoustic case, we will first formulate the solution of the direct scattering problem through a dimension reduction process. Since the electromagnetic problem is a vectorial one, this process will employ vectorial basis functions instead of the scalar spherical harmonics used in the solution of the acoustic problem. Because of this difference, the reduction process will result in a system of reduced integral equations instead of a single object and a single data equation. However, it should be noted that the main approach of the process, namely obtaining 1-D integral equations using series expansions and orthogonality relations, remains the same; therefore, the formulation and the solution of the direct scattering problem will follow a similar outline as the acoustic case. In the second part, the solution of the related inverse problem will be developed using this system of reduced 1-D integral equations. Since the nature of the problems are similar, the classical Newton algorithm will be used once again for solving the inverse problem. The effect of replacing a single data equation with a system of equations will also be discussed in the same part. A time dependence $e^{-i\omega t}$ is assumed and omitted throughout the entire section.

3.2 Direct Scattering Problem

In this sub-section, we will first give a brief presentation of the vector spherical harmonics and the vector wave functions. These functions will provide the vectorial basis functions that will be used in the series expansion of the electric field and the free space dyadic Green's function. The same orthogonality relationships that were demonstrated in the acoustic section will form the mathematical foundation for the formulation of the vector spherical harmonics. The second part will be the main body of this sub-section, and will include the formulation of the problem. After the scattering problem is first formulated, the dimension reduction process will be

developed using the aforementioned vector spherical harmonics. Via this reduction process, one can replace the 3-D integral equation with a system of reduced 1-D integral equations by expressing the interior and scattered electric field in terms of the vector spherical harmonics. The solution of the direct scattering problem will be obtained using this system of integral equations. Finally, in the third part, the success of the method developed in the previous section will be tested via numerical simulations. The results will be compared with alternative methods such as dyadic Green's function or MoM. The content of this section has been presented in a more compact form in [67]. Here, the formulation of the method will be demonstrated in a more detailed manner.

3.2.1 Vectorial basis functions

In this sub-section, the basis functions that will be used in the series expansions for the interior and scattered electric field will be introduced. These functions compose the solution of the vector wave equation in the spherical coordinate system. The solution of this equation can be formulated using the scalar harmonics, which form the solution of scalar Helmholtz equation. Therefore, the orthogonality relationships related to scalar harmonics will be reused in this section to develop the orthogonality conditions necessary for the series expansions. In the first sub-section, we will introduce the vector spherical harmonics that will be used as the basis functions of the series expansion for the electric field. The orthogonality of these functions over the unit spherical surface will be demonstrated, and the terms of a series expansion with vectorial basis functions will be defined. This series expansion will be used to express the vectorial electric field. The main goal of the dimension reduction process is to obtain 1-D integral equations containing the scalar coefficients of the series expansion for the interior electric field. In the second part, the spherical vector wave functions will be obtained using the vector spherical harmonics. The vector wave functions constitute the formal solution of the Helmholtz equation in the spherical coordinates. That is, in the source free homogeneous medium, the electric field can be expressed in terms of these functions. Therefore, as it will be demonstrated in the next sections, the scattered field outside the sphere can be expanded in terms of vector wave functions. On the other hand, because of the radial inhomogeneity, the field inside the sphere can only be expressed in terms of the vector spherical harmonics. Finally, the expansion of the free space dyadic Green's function will also be presented in the second part.

3.2.1.1 Vector spherical harmonics

As stated in [54], the solution of the Maxwell equations in the spherical coordinates can be expressed via some vector-valued functions, which later will form the basis for the series expansion of the electric field in the source free homogeneous medium. The vector spherical harmonics are defined in [54] in order to construct these vector-valued solutions. Moreover, as it will be demonstrated in the subsequent sections, these harmonics can also be effectively used to represent the angular part of the electric field within the radially inhomogeneous spherical scatterer. Therefore, the definition of the vector spherical harmonics and the analysis of their their mathematical properties is a prerequisite to formulating the solution of the direct scattering problem via a dimension reduction process. A detailed analysis of the subject can be found in [54]. Here, we will present a brief summary, involving the definitions and the essential orthogonality relations, of the comprehensive treatment given in [54].

The vector spherical harmonics are based on the scalar spherical harmonics that have been used in the solution of the acoustic problem. For the sake of presentation, we will first express the scalar harmonics in a more compact form as

$$Y_{nm}(\theta,\phi) = \sqrt{\frac{(2n+1)(n-m)!}{4\pi(n+m)!}} P_n^m(\cos\theta)e^{im\phi} = C_{nm}P_n^m(\cos\theta)e^{im\phi} \tag{3.1}$$

where C_{nm} is the normalization factor. The following relations hold for negative values of indice m:

$$Y_{n,-m}(\theta,\phi) = (-1)^m Y_{nm}^*(\theta,\phi) \tag{3.2}$$

$$\frac{\partial}{\partial\theta}Y_{n,-m}(\theta,\phi) = (-1)^m \left[\frac{\partial}{\partial\theta}Y_{nm}^*(\theta,\phi)\right] \tag{3.3}$$

Here, $Y_{nm}^*(\theta,\phi)$ represents the complex conjugate. From the orthogonality relations already established in the acoustic section, it is clear that $Y_{nm}(\theta,\phi)$ are orthonormal over the unit spherical surface, that is these functions satisfy the orthogonality condition

$$\int_0^{2\pi}\int_0^{\pi} Y_{nm}(\theta,\phi)Y_{n'm'}(\theta,\phi)\sin\theta d\theta d\phi = \delta_{nn'}\delta_{mm'} \tag{3.4}$$

where δ is the Kronocker delta. Taking (3.4) into account, a series expansion in terms of the scalar harmonics can be defined for the vectorial electric field $\mathbf{E}(\mathbf{r})$ satisfying the Maxwell equations

$$\nabla\times(\nabla\times\mathbf{E}(\mathbf{r})) - k_0^2\mathbf{E}(\mathbf{r}) = 0 \tag{3.5}$$

in a source free homogeneous medium. Here, k_0 denotes the wave number of the medium. However, as indicated in [54], such a series would have vector-valued coefficients, and therefore would be unsuitable for the dimension reduction process. In order to have a series expansion with scalar coefficients, a set of vector-valued basis functions that are orthonormal over the unit spherical surface must be defined [54]. The vector spherical harmonics constitute such a set of basis functions. These vector-valued functions are defined by using scalar harmonics as:

$$\mathbf{A}_{1nm}(\theta,\phi) = \frac{1}{\sqrt{n(n+1)}}\nabla\times[\mathbf{r}Y_{nm}(\theta,\phi)] \tag{3.6}$$

$$\mathbf{A}_{2nm}(\theta,\phi) = \frac{1}{\sqrt{n(n+1)}}r\,\nabla Y_{nm}(\theta,\phi) \tag{3.7}$$

$$\mathbf{A}_{3nm}(\theta,\phi) = \mathbf{r}Y_{nm}(\theta,\phi) \tag{3.8}$$

Alternatively, these functions can be expressed in terms of the unit vectors $\hat{r}$, $\hat{\theta}$, $\hat{\phi}$ of the spherical coordinates system:

$$\mathbf{A}_{1nm}(\theta,\phi) = \frac{1}{\sqrt{n(n+1)}}\left\{\frac{1}{\sin\theta}\frac{\partial}{\partial\phi}Y_{nm}(\theta,\phi)\hat{\theta} - \frac{\partial}{\partial\theta}Y_{nm}(\theta,\phi)\hat{\phi}\right\} \tag{3.9}$$

$$\mathbf{A}_{2nm}(\theta,\phi) = \frac{1}{\sqrt{n(n+1)}}\left\{\frac{\partial}{\partial\theta}Y_{nm}(\theta,\phi)\hat{\theta} + \frac{1}{\sin\theta}\frac{\partial}{\partial\phi}Y_{nm}(\theta,\phi)\hat{\phi}\right\} \tag{3.10}$$

$$\mathbf{A}_{3nm}(\theta,\phi) = Y_{nm}(\theta,\phi)\hat{r} \tag{3.11}$$

Considering (3.2) and (3.3), the forms of the vector spherical harmonics for negative values of m are determined by

$$\mathbf{A}_{\tau n,-m}(\theta,\phi) = (-1)^m \mathbf{A}_{\tau nm}^*(\theta,\phi) \tag{3.12}$$

where $\tau = 1,2,3$. Before stating the orthogonality condition related to the vector spherical harmonics, one more orthogonality relation for the associated Legendre functions must be established. Using (2.12) and the formula for the derivative of Legendre functions available in [36], following equations can be obtained:

$$\int_0^\pi \left\{ \frac{\partial P_n^m(\cos\theta)}{\partial\theta} \frac{\partial P_{n'}^m(\cos\theta)}{\partial\theta} + m^2 \frac{P_n^m(\cos\theta)}{\sin\theta} \frac{P_{n'}^m(\cos\theta)}{\sin\theta} \right\} \sin\theta d\theta = $$
$$\frac{2n(n+1)(n+m)!}{(2n+1)(n-m)!} \delta_{nn'} \tag{3.13}$$

$$\int_0^\pi \left\{ \frac{\partial P_n^m(\cos\theta)}{\partial\theta} \frac{P_{n'}^m(\cos\theta)}{\sin\theta} + \frac{P_n^m(\cos\theta)}{\sin\theta} \frac{\partial P_{n'}^m(\cos\theta)}{\partial\theta} \right\} \sin\theta d\theta = 0 \tag{3.14}$$

The orthogonality of the vector spherical harmonics over a spherical surface can be easily demonstrated using (3.13)-(3.14) and the orthogonality relations previously stated in (2.10)-(2.13). The resulting orthogonality relation can be expressed as

$$\int_0^{2\pi}\int_0^\pi \mathbf{A}_{\tau nm}(\theta,\phi)\mathbf{A}_{\tau'n'm'}^*(\theta,\phi)\sin\theta d\theta d\phi = \delta_{\tau\tau'}\delta_{nn'}\delta_{mm'} \tag{3.15}$$

(3.15) demonstrates that vector spherical harmonics constitute a set of vector-valued functions orthonormal over the unit spherical surface. Therefore, a series expansion for the vectorial electric field can be formulated as

$$\mathbf{E}(\mathbf{r}) = \sum_{n=0}^\infty \sum_{m=-n}^n \left\{ \alpha_{nm}(r)\mathbf{A}_{1nm}(\theta,\phi) + \beta_{nm}(r)\mathbf{A}_{2nm}(\theta,\phi) \right.$$
$$\left. + \gamma_{nm}(r)\mathbf{A}_{3nm}(\theta,\phi) \right\} \tag{3.16}$$

It should be noted that the scalar coefficients $\alpha_{nm}(r)$, $\beta_{nm}(r)$, $\gamma_{nm}(r)$ are functions of the radial distance only. Therefore, this series expansion is especially suitable for expressing the electric field inside the radially inhomogeneous spherical scatterer. By

isolating the radial variation which is affected by the inhomogeneity, the orthogonality of angular ones can be preserved. The dimension reduction process will be executed by taking advantage of this orthogonality, and the main aim of the process will be to obtain a system of 1-D integral equations involving the coefficients of the electric field. On the other hand, in the homogeneous region, that is outside the sphere, the radial dependance can be determined by solving (3.5). These solutions will be obtained in the next sub-section.

3.2.1.2 Spherical vector wave functions

In this sub-section, we will formulate the solutions of the vector wave equation defined in (3.5), in the source free homogeneous medium. Similar to the previous sub-section, the formulation will follow the one presented in [54], with a slightly modified notation. The solutions, named spherical vector wave functions, will later be used in the expansion of the 3-D free space dyadic Green's function, and the incoming vectorial electric field in the spherical coordinates. It is clear from the discussion presented in the previous section that the angular components of these vector wave functions will be formed by the vector spherical harmonics. Therefore, in this section, the radial dependence of the vector wave functions will be determined. To this end, the expansion for the electric field given in (3.16) should be substituted into the wave equation (3.5). The resulting equation can be stated in an open form as

$$
\begin{aligned}
\nabla \times (\nabla \times \mathbf{E}(\mathbf{r})) - k_0^2 \mathbf{E}(\mathbf{r}) = \sum_{n=0}^{\infty} \sum_{m=-n}^{n} & \left\{ -\left(\frac{(r\alpha_{nm}(r))'}{r} \right)' \mathbf{A}_{1nm}(\theta,\phi) \right. \\
& -\left(\frac{(r\beta_{nm}(r))' - \gamma_{nm}(r)\sqrt{n(n+1)}}{r} \right)' \mathbf{A}_{2nm}(\theta,\phi) - \frac{(r\alpha_{nm}(r))'}{r^2} \mathbf{A}_{1nm}(\theta,\phi) \\
& -\frac{(r\beta_{nm}(r))' - \gamma_{nm}(r)\sqrt{n(n+1)}}{r} \left(\mathbf{A}_{2nm}(\theta,\phi) + \sqrt{n(n+1)}\mathbf{A}_{3nm}(\theta,\phi) \right) \\
& \left. +\frac{n(n+1)}{r^2} \alpha_{nm}(r)\mathbf{A}_{1nm}(\theta,\phi) \right\} - k_0^2 \sum_{n=0}^{\infty} \sum_{m=-n}^{n} \left\{ \alpha_{nm}(r)\mathbf{A}_{1nm}(\theta,\phi) \right. \\
& \left. +\beta_{nm}(r)\mathbf{A}_{2nm}(\theta,\phi) + \gamma_{nm}(r)\mathbf{A}_{3nm}(\theta,\phi) \right\} = 0
\end{aligned}
\tag{3.17}
$$

Using the orthogonality of the vector spherical harmonics demonstrated in the previous sub-section, separated equations can be obtained for the coefficients $\alpha_{nm}(r)$, $\beta_{nm}(r)$,

66

$\gamma_{nm}(r)$. Multiplying both sides of the equation by complex conjugates of vector spherical harmonics $\mathbf{A}^*_{\tau nm}(\theta,\phi)$ in order, and integrating over unit spherical surface yields three differential equations for the coefficients:

$$\frac{d}{dr}\left(r^2 \frac{d}{dr}\alpha_{nm}(r)\right) - n(n+1)\alpha_{nm}(r) + k_0^2 r^2 \alpha_{nm}(r) = 0 \tag{3.18}$$

$$\frac{d}{dr}\left(r^2 \frac{d}{dr}\beta_{nm}(r)\right) - r\sqrt{n(n+1)}\frac{d}{dr}\gamma_{nm}(r) + k_0^2 r^2 \beta_{nm}(r) = 0 \tag{3.19}$$

$$\sqrt{n(n+1)}\frac{d}{dr}\left(r\beta_{nm}(r)\right) - n(n+1)\gamma_{nm}(r) + k_0^2 r^2 \gamma_{nm}(r) = 0 \tag{3.20}$$

Note that the coefficients $\beta_{nm}(r)$ and $\gamma_{nm}(r)$ are coupled in (3.19) and (3.20), indicating that the final solution will involve both coefficients, and the related vector spherical harmonics $\mathbf{A}_{2nm}(\theta,\phi)$, $\mathbf{A}_{3nm}(\theta,\phi)$. On the other hand, (3.18) is an independent equation, and its solution yields spherical Bessel functions. In conclusion, the solutions of (3.18)-(3.20) are obtained as

$$\alpha_{nm}(r) = z_n(kr) \tag{3.21}$$

$$\beta_{nm}(r) = \frac{1}{k_0 r}\frac{d}{dr}\left(r\, z_n(k_0 r)\right) \tag{3.22}$$

$$\gamma_{nm}(r) = \sqrt{n(n+1)}\frac{z_n(k_0 r)}{k_0 r} \tag{3.23}$$

where $z_n(k_0 r)$ denotes either $j_n(k_0 r)$ or $h_n^{(1)}(k_0 r)$ depending on the type of wave, that is the region where the solution is defined. It is clear that for radiating scattered field, the radial dependency should be represented by $h_n^{(1)}(k_0 r)$ in order to satisfy the radiation condition at infinity. Using the results given in (3.21)-(3.23), and considering the fact that the coefficients $\beta_{nm}(r)$ and $\gamma_{nm}(r)$ are coupled, the spherical vector wave functions can be determined as [53]

$$\mathbf{M}_{nm}(k_0\mathbf{r}) = \sqrt{n(n+1)}\, z_n(k_0 r)\mathbf{A}_{1nm}(\theta,\phi) \tag{3.24}$$

$$\mathbf{N}_{nm}(k_0\mathbf{r}) = \sqrt{n(n+1)}\,\frac{1}{k_0 r}\frac{d}{dr}\Big(rz_n(k_0 r)\Big)\mathbf{A}_{2nm}(\theta,\phi)$$
$$+ n(n+1)\frac{z_n(k_0 r)}{k_0 r}\mathbf{A}_{3nm}(\theta,\phi) \tag{3.25}$$

Since the angular component of the wave functions are composed of spherical harmonics, these functions are also orthogonal over the unit spherical surface, and they form a complete set. Note that the functions defined in (3.24)-(3.25) have zero divergence. Therefore, a third vector wave functions should be included in the representation of the electric field in the source region. This additional vector wave function is defined as

$$\mathbf{L}_{nm}(k_0\mathbf{r}) = \sqrt{n(n+1)}\,\frac{1}{k_0 r}z_n(k_0 r)\mathbf{A}_{2nm}(\theta,\phi)$$
$$+ \frac{1}{k_0}\frac{d}{dr}\Big(z_n(k_0 r)\Big)\mathbf{A}_{3nm}(\theta,\phi) \tag{3.26}$$

For the formulation used in this thesis, the function $\mathbf{L}_{nm}(k_0\mathbf{r})$ would not be needed, since the field inside the sphere will be represented by the series expansion given in (3.16), instead of one that uses vector wave functions. On the other hand, the scattered field can be expanded in terms of vector wave functions, since the region outside the sphere is assumed to be homogeneous. Therefore, the scattered field will be expressed by a series expansion of the form

$$\mathbf{E}^s(\mathbf{r}) = \sum_{n=0}^{\infty}\sum_{m=-n}^{n}\Big\{A_{nm}\mathbf{M}_{nm}^{(1)}(k_0\mathbf{r}) + B_{nm}\mathbf{N}_{nm}^{(1)}(k_0\mathbf{r})\Big\} \tag{3.27}$$

where A_{nm} and B_{nm} are scalar constant coefficients. In (3.27), the superscript (1) signals that the radial dependence is expressed by spherical Hankel functions $h_n^{(1)}(k_0 r)$ in order to represent out-going scattered field. The free-space dyadic Green's function can also be expanded in terms of the vector wave functions in the spherical coordinates as [53]

$$\bar{\bar{\mathbf{G}}}_0(\mathbf{r},\mathbf{r}') = ik_0 \sum_{n=0}^{\infty} \sum_{m=-n}^{n} \frac{1}{n(n+1)} \left\{ \mathbf{M}_{nm}(k_0\mathbf{r})\mathbf{M}^*_{nm}(k_0\mathbf{r}') \right. $$
$$\left. + \mathbf{N}_{nm}(k_0\mathbf{r})\mathbf{N}^*_{nm}(k_0\mathbf{r}') \right\} - \frac{\hat{r}\hat{r}}{k_0^2} \delta(\mathbf{r}\text{-}\mathbf{r}') \tag{3.28}$$

In (3.28) the radial functions $z_n(k_0 r)$ of the vector wave functions denote either $j_n(k_0 r_<)$ or $h_n^{(1)}(k_0 r_>)$, where $r_<$ and $r_>$ represent the smaller and the larger of the pair r, r' respectively. This expansion will be used in the dimension reduction process.

A final point to note is that in the literature, slightly different formulations are used in the definition of vector wave functions. In [51] and [52], linear combinations of trigonometric functions $\cos(m\phi)$ and $\sin(m\phi)$ are used to represent the angular dependence. Since these textbooks will be frequently referred in the subsequent sections, their definition of vector wave functions should be presented here. In [51], Stratton defined these functions as

$$\mathbf{M}_{e\,nm\,o}(k_0\mathbf{r}) = \mp \frac{m}{\sin\theta} z_n(k_0 r) P_n^m(\cos\theta) \begin{pmatrix} \sin m\phi \\ \cos m\phi \end{pmatrix} \hat{\theta}$$
$$- z_n(k_0 r) \frac{\partial}{\partial\theta} P_n^m(\cos\theta) \begin{pmatrix} \cos m\phi \\ \sin m\phi \end{pmatrix} \hat{\phi} \tag{3.29}$$

$$\mathbf{N}_{e\,nm\,o}(k_0\mathbf{r}) = \frac{n(n+1)}{k_0 r} z_n(k_0 r) P_n^m(\cos\theta) \begin{pmatrix} \cos m\phi \\ \sin m\phi \end{pmatrix} \hat{r}$$
$$+ \frac{1}{k_0 r} \frac{d}{dr}\left(r z_n(k_0 r)\right) \frac{\partial}{\partial\theta} P_n^m(\cos\theta) \begin{pmatrix} \cos m\phi \\ \sin m\phi \end{pmatrix} \hat{\theta} \tag{3.30}$$
$$\mp \frac{m}{k_0 r \sin\theta} \frac{d}{dr}\left(r z_n(k_0 r)\right) P_n^m(\cos\theta) \begin{pmatrix} \sin m\phi \\ \cos m\phi \end{pmatrix} \hat{\phi}$$

where the subscripts e and o refer to even and odd functions respectively. The free space dyadic Green's function can be alternatively defined by a series expansion in terms of these even and odd vector wave functions. Such an expansion is provided in [52] by Tai:

69

$$\bar{\bar{\mathbf{G}}}_0^{eo}(\mathbf{r},\mathbf{r}') = \frac{ik_0}{4\pi} \sum_{n=1}^{\infty} \sum_{m=0}^{n} (2-\delta_0) \frac{2n+1}{n(n+1)} \frac{(n-m)!}{(n+m)!}$$

$$\times \begin{cases} \mathbf{M}_{\substack{e\\o}nm}^{(1)}(k_0\mathbf{r})\mathbf{M}_{\substack{e\\o}nm}(k_0\mathbf{r}') + \mathbf{N}_{\substack{e\\o}nm}^{(1)}(k_0\mathbf{r})\mathbf{N}_{\substack{e\\o}nm}(k_0\mathbf{r}') & r > r' \\ \mathbf{M}_{\substack{e\\o}nm}(k_0\mathbf{r})\mathbf{M}_{\substack{e\\o}nm}^{(1)}(k_0\mathbf{r}') + \mathbf{N}_{\substack{e\\o}nm}(k_0\mathbf{r})\mathbf{N}_{\substack{e\\o}nm}^{(1)}(k_0\mathbf{r}') & r < r' \end{cases} \quad (3.31)$$

where

$$\delta_0 = \begin{cases} 1 & m = 0 \\ 0 & m \neq 0 \end{cases} \quad (3.32)$$

Since it includes neither the functions $\mathbf{L}_{nm}(k_0\mathbf{r})$ nor the last term in (3.28) with dyad $\hat{r}\hat{r}$, $\bar{\bar{\mathbf{G}}}_0^{eo}(\mathbf{r},\mathbf{r}')$ is not valid in the source region [53]. However, it should be noted that, outside source region, the expansion given in (3.31) is equivalent to the one introduced in (3.28). Therefore, both forms of free space dyadic Green's function can be used in the formulation of direct scattering problem, although $\bar{\bar{\mathbf{G}}}_0(\mathbf{r},\mathbf{r}')$ will be more frequently employed in this thesis. The correspondance of the even and odd functions defined in (3.29)-(3.30) to the vector wave functions introduced in (3.24)-(3.25), and will be used throughout this thesis, is determined in [68] as

$$\mathbf{X}_{enm}(k_0\mathbf{r}) = \frac{1}{2C_{nm}}\left(\mathbf{X}_{nm}(k_0\mathbf{r}) + (-1)^m \mathbf{X}_{n,-m}(k_0\mathbf{r})\right) \quad (3.33)$$

$$\mathbf{X}_{onm}(k_0\mathbf{r}) = \frac{1}{2iC_{nm}}\left(\mathbf{X}_{nm}(k_0\mathbf{r}) - (-1)^m \mathbf{X}_{n,-m}(k_0\mathbf{r})\right) \quad (3.34)$$

where $\mathbf{X}$ represents either $\mathbf{M}$ or $\mathbf{N}$, and C_{nm} denotes the normalization factor defined in (3.1).

3.2.2 Solution of the direct scattering problem

In the first part of this sub-section, the general formulation of the direct scattering problem will be presented. We will define the electromagnetic vectorial problem in its original 3-D form, and then introduce the electric field integral equation that will be reduced to a 1-D form. The series expansion for the incoming field will also be

70

constructed in this section. The details of the dimension reduction process will be presented in the second part. The main aim of that process is to obtain 1-D integral equations involving scalar coefficients of the series expansion for the electric field. Unlike the acoustic problem, the 3-D object equation cannot be reduced to a single 1-D equation; instead, it will be replaced by a system of reduced integral equations. Solution of the direct scattering problem will be obtained by solving this system via a discretization of the integration domain.

3.2.2.1 Formulation of the problem

Consider a dielectric spherical object with radius a, denoted by D in Fig. 3.1, whose permittivity $\varepsilon(r)$, and conductivity $\sigma(r)$ are arbitrarily varying functions of radial distance r only. The magnetic permeability μ_0 is considered constant throughout the whole space. The region outside the sphere is assumed to be described by a constant wave number $k_0 = \omega\sqrt{\varepsilon_0\mu_0}$, ε_0 being the free space dilectric constant, and ω the operating angular frequency of the source. The sphere is illuminated by a infinitesimal horizontal electric dipole with a current moment C_0 pointed in the x-direction, located at the point $x = 0$, $y = 0$, $z = z_d$, ($z_d > a$).
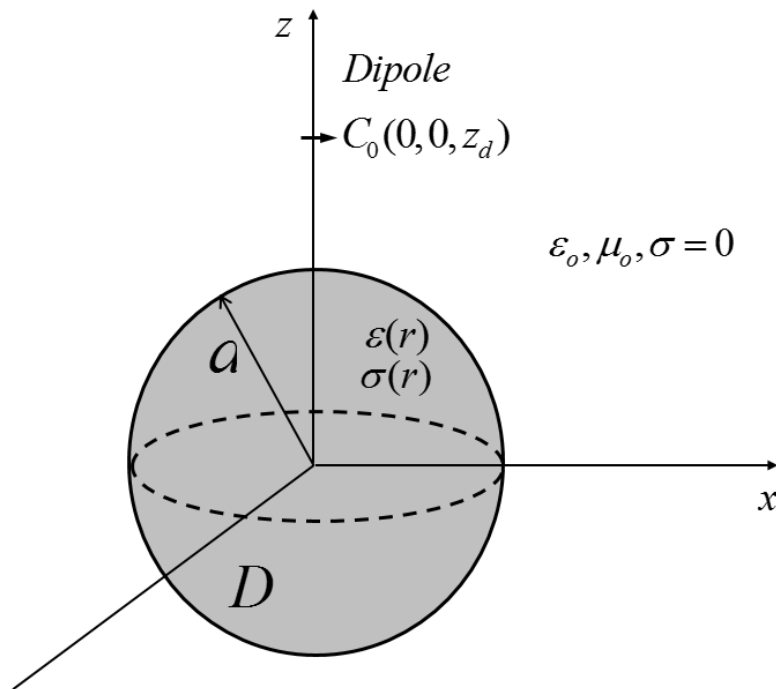
Figure 3.1 : The geometry of the direct scattering problem.

The total electric field inside sphere, $\mathbf{E}(\mathbf{r})$, satisfies the electric field integral equation

$$\mathbf{E}(\mathbf{r}) = \mathbf{E}^i(\mathbf{r}) + k_0^2 \int_D \bar{\bar{\mathbf{G}}}_0(\mathbf{r}, \mathbf{r}') v(r') \mathbf{E}(\mathbf{r}') dv' \qquad \mathbf{r} \in D$$

(3.35)

where $\mathbf{E}^i(\mathbf{r})$ represents the incoming electric field. Similarly, the scattered field outside the sphere can be expressed by

$$\mathbf{E}^s(\mathbf{r}) = k_0^2 \int_D \bar{\bar{\mathbf{G}}}_0(\mathbf{r}, \mathbf{r}') v(r') \mathbf{E}(\mathbf{r}') dv' \qquad |\mathbf{r}| > a$$

(3.36)

Similar to the acoustic case, the function $v(r')$ appearing in (3.35) and (3.36) denotes the object function that is defined as

$$v(r) = \frac{k^2(r)}{k_0^2} - 1$$

(3.37)

where $k^2(r) = \omega^2 \mu_0 \varepsilon(r) + i\omega \mu_0 \sigma(r)$ inside the sphere, and $k^2(r) = k_0^2$ in the outside region. It is clear that (3.35) and (3.36) have similar forms as (2.40) and (2.39) respectively. Therefore, (3.35) can be named as the 3-D electromagnetic object equation, and (3.36) is called as the data equation. One can obtain the electric field anywhere in the space by solving the system formed by these equations, via a numerical technique such as MoM [14]. However, since the electromagnetic problem is a vectorial one, the computational effort required for solving 3-D problem is even higher than the acoustic case. Therefore, a dimension reduction process will be applied in this thesis to replace 3-D equations by 1-D reduced integral equations. To this end, the electric field $\mathbf{E}(\mathbf{r})$ and the free space dyadic Green's function $\bar{\bar{\mathbf{G}}}_0(\mathbf{r}, \mathbf{r}')$ will be expressed as series expansions. Although the approach will be similar to the one used for the solution of the acoustic problem, the technique must be altered to suit the vectorial problem. The details of the procedure will be explained in the next sub-section.

It should be noted that in order to complete the expansion of (3.35), the incoming electric field must also be expressed as a series expansion, and the coefficients of this expansion must be determined before solving the system of reduced object and data

equations that will be produced by the dimension reduction process. To this end, the incident field will be expressed as a series expansion in a form similar to the interior electric field:

$$\mathbf{E}^i(\mathbf{r}) = \sum_{n=0}^{\infty} \sum_{m=-n}^{n} \left\{ \alpha_{nm}^i(r)\mathbf{A}_{1nm}(\theta,\phi) + \beta_{nm}^i(r)\mathbf{A}_{2nm}(\theta,\phi) \right.$$
$$\left. + \gamma_{nm}^i(r)\mathbf{A}_{3nm}(\theta,\phi) \right\}$$

(3.38)

Note that an expansion in terms of vector wave functions, like the one introduced in (3.27), can also be used, since the calculation of the incident field assumes a homogenous space characterized by k_0. The form of (3.38) is chosen to match the expansion of the interior electric field, and to simplify the structures of the reduced equations that will be formed in the next sub-section.

First, we will obtain the coefficients for the infinetesimal horizontal electric dipole depicted in Fig 3.1. The series expansion of the field created by this source is developed in [52]. Here, the results will be reproduced, and the process will be presented in a more detailed fashion. Following the notation of [52], (3.31) will be used as the free-space dyadic Green's function. The current density of the x-oriented dipole situated at $r' = z_d$, $\theta' = 0$, $\phi' = 0$ is defined as [52]

$$\mathbf{J}(\mathbf{r}') = C_0 \frac{\delta(r' - z_d)\delta(\theta' - 0)\delta(\phi' - 0)}{z_d^2 \sin\theta'} \hat{x}$$

(3.39)

The field induced by this dipole can be determined by a convolution integral involving the free space dyadic Green's function that yields [52]

$$\mathbf{E}^i(\mathbf{r}) = i\omega\mu_0 \int \bar{\bar{\mathbf{G}}}_0^{eo}(\mathbf{r},\mathbf{r}')\mathbf{J}(\mathbf{r}')dv' = i\omega\mu_0 C_0 \bar{\bar{\mathbf{G}}}_0^{eo}(\mathbf{r},\mathbf{r}') \cdot \hat{x}$$

(3.40)

Considering that in (3.40)

$$\hat{x} = \cos\theta' \sin\phi'\,\hat{r} + \cos\theta' \cos\phi'\,\hat{\theta} - \sin\phi'\,\hat{\phi},$$

(3.41)

and $\mathbf{r}' = (z_d, 0, 0)$ in spherical coordinates, it is clear that only the $\hat{\theta}$ components of $\mathbf{M}_{\substack{e \\ o}nm}(k_0\mathbf{r}')$ and $\mathbf{N}_{\substack{e \\ o}nm}(k_0\mathbf{r}')$ will make a contribution to the final form of (3.40); the

73

remaining components do not survive the scalar product with $\hat{x}$. Moreover, since $\phi' = 0$, the outcome of the functions $\mathbf{M}_{enm}(k_0\mathbf{r}')$ and $\mathbf{N}_{onm}(k_0\mathbf{r}')$ will be zero due to the term $\sin\phi'$. Therefore, the expression of incident field becomes

$$\mathbf{E}^i(\mathbf{r}) = \frac{-k_0\omega\mu_0 C_0}{4\pi} \sum_{n=1}^{\infty} \sum_{m=0}^{n} (2-\delta_0) \frac{2n+1}{n(n+1)} \frac{(n-m)!}{(n+m)!}$$
$$\times \mathbf{M}_{onm}(k_0\mathbf{r})\left[\mathbf{M}_{onm}^{(1)}(k_0\mathbf{r}')\right]_\theta + \mathbf{N}_{enm}(k_0\mathbf{r})\left[\mathbf{N}_{enm}^{(1)}(k_0\mathbf{r}')\right]_\theta \tag{3.42}$$

where $\left[\mathbf{M}_{onm}^{(1)}(k_0\mathbf{r}')\right]_\theta$ and $\left[\mathbf{N}_{enm}^{(1)}(k_0\mathbf{r}')\right]_\theta$ denote the $\hat{\theta}$ components of the respective functions. Note that in (3.42) only the case of $r < r'$ is taken into account, since $r' = z_d$ and for the region inside the sphere $r < z_d$. The final point to consider is the behaviour of the associated Legendre functions for $\theta' = 0$. Calculating the limit values of the terms with θ' in $\left[\mathbf{M}_{onm}^{(1)}(k_0\mathbf{r}')\right]_\theta$ and $\left[\mathbf{N}_{enm}^{(1)}(k_0\mathbf{r}')\right]_\theta$ yields

$$\lim_{\theta'\to 0^-} \frac{P_n^m(\cos\theta')}{\sin\theta'} = \lim_{\theta'\to 0^-} \frac{\frac{\partial}{\partial\theta'}P_n^m(\cos\theta')}{\cos\theta'} = \lim_{\theta'\to 0^-} \frac{\partial}{\partial\theta'}P_n^m(\cos\theta')$$
$$= \begin{cases} \infty & m = 0 \\ \dfrac{n(n+1)}{2} & m = 1 \\ 0 & m \neq 0,1 \end{cases} \tag{3.43}$$

(3.43) demonstrates that only for $m=1$, $\left[\mathbf{M}_{onm}^{(1)}(k_0\mathbf{r}')\right]_\theta$ and $\left[\mathbf{N}_{enm}^{(1)}(k_0\mathbf{r}')\right]_\theta$ takes non-zero finite values. Therefore, the series with indice m disappears from (3.42), and the equation simplifies to [52]

$$\mathbf{E}^i(\mathbf{r}) = \frac{-k_0\omega\mu_0 C_0}{4\pi} \sum_{n=1}^{\infty} \frac{2n+1}{n(n+1)}\left\{h_n^{(1)}(k_0 z_d)\mathbf{M}_{on1}(k_0\mathbf{r})\right.$$
$$\left. + \frac{1}{k_0 z_d} \frac{d}{dr'}\left(r'h_n^{(1)}(k_0 r')\right)\bigg|_{r'=z_d} \mathbf{N}_{en1}(k_0\mathbf{r})\right\} \tag{3.44}$$

Although (3.44) completes the series expansion of the incident field for an infinitesimal horizontal dipole, it is not yet suitable for determining the coefficients $\alpha_{nm}^i(r)$, $\beta_{nm}^i(r)$ and $\gamma_{nm}^i(r)$ that will be used in the solution of the reduced direct scattering problem. To this end, the series expansion in (3.44) should be restated using

the vector wave functions defined in (3.24)-(3.25). Using the identity established in (3.33) and (3.34), the incident field can be expressed as

$$
\begin{aligned}
\mathbf{E}^i(\mathbf{r}) = \frac{-k_0 \omega \mu_0 C_0}{2} \sum_{n=1}^{\infty} & \sqrt{\frac{2n+1}{4\pi n(n+1)}} \Big\{ -i\, h_n^{(1)}(k_0 z_d) \mathbf{M}_{n1}(k_0 \mathbf{r}) \\
& - i\, h_n^{(1)}(k_0 z_d) \mathbf{M}_{n,-1}(k_0 \mathbf{r}) + \frac{1}{k_0 z_d} \frac{d}{dr'}\Big(r' h_n^{(1)}(k_0 r') \Big)\Big|_{r'=z_d} \mathbf{N}_{n1}(k_0 \mathbf{r}) \\
& - \frac{1}{k_0 z_d} \frac{d}{dr'}\Big(r' h_n^{(1)}(k_0 r') \Big)\Big|_{r'=z_d} \mathbf{N}_{n,-1}(k_0 \mathbf{r}) \Big\}
\end{aligned}
\tag{3.45}
$$

Considering the expressions of the vector wave functions given in (3.24)-(3.25), the coefficients of the incident field for x-oriented inifnitesimal horizontal electric dipole can be determined from (3.45) as

$$
\alpha_{nm}^i(r) = \frac{ik_0 \omega \mu_0 C_0}{2} \sqrt{\frac{2n+1}{4\pi}} h_n^{(1)}(k_0 z_d) j_n(k_0 r) \qquad m = -1,1
\tag{3.46}
$$

$$
\begin{aligned}
\beta_{nm}^i(r) = -m \frac{k_0 \omega \mu_0 C_0}{2} & \sqrt{\frac{2n+1}{4\pi}} \frac{1}{k_0 z_d} \frac{d}{dr'}\Big(r' h_n^{(1)}(k_0 r') \Big)\Big|_{r'=z_d} \\
& \times \frac{1}{k_0 r} \frac{d}{dr}\big(r j_n(k_0 r) \big) \qquad m = -1,1
\end{aligned}
\tag{3.47}
$$

$$
\begin{aligned}
\gamma_{nm}^i(r) = -m \frac{k_0 \omega \mu_0 C_0}{2} & \sqrt{\frac{2n+1}{4\pi n(n+1)}} \frac{1}{k_0 z_d} \frac{d}{dr'}\Big(r' h_n^{(1)}(k_0 r') \Big)\Big|_{r'=z_d} \\
& \times n(n+1) \frac{j_n(k_0 r)}{k_0 r} \qquad m = -1,1
\end{aligned}
\tag{3.48}
$$

It should be clear that for any $m \neq -1,1$, the coefficients are all zeros.

Another frequently used incident field is the plane wave excitation. Therefore, we will also present the coefficients for an x-polarized plane wave travelling in the z direction. The series expansion for this incident field has been obtained by Stratton in [51], using even and odd vector wave functions. As noted in [51], the divergence of the electric field excited by an x-polarized plane wave is zero, therefore the functions $\mathbf{L}_{nm}(k_0 \mathbf{r})$ are not needed for the expansion. Moreover, to avoid having singularity in the origin the functions $j_n(k_0 r)$ must be used to express the radial component [51]. Therefore, the expansion would have the form

$$\mathbf{E}^i(\mathbf{r}) = e^{ikz}\hat{x} = \sum_{n=1}^{\infty}\sum_{m=0}^{n} a_{nm}\mathbf{M}_{\substack{e\\o}nm}(k_0\mathbf{r}) + b_{nm}\mathbf{N}_{\substack{e\\o}nm}(k_0\mathbf{r}) \tag{3.49}$$

The scalar coefficients a_{nm} and b_{nm} can be determined using the orthogonality relations. Considering the expression $\hat{x}$ given in (3.41), and the ϕ dependence of the vector wave functions; it is clear that only $\mathbf{M}_{on1}(k_0\mathbf{r})$ and $\mathbf{N}_{en1}(k_0\mathbf{r})$ will have non-zero contributions [51]. Therefore, using the series expansion for the plane wave introduced in (2.16), the coefficients can be determined as [51]

$$a_{n1} = \frac{2n+1}{n(n+1)} i^n \tag{3.50}$$

$$b_{n1} = \frac{2n+1}{n(n+1)}(-i^{n+1}) \tag{3.51}$$

Once again through the equivalence demonstrated in (3.33)-(3.34), the final form of the coefficients for the x-polarized plane wave travelling along the positive z direction can be stated as

$$\alpha_{nm}^i(r) = i^{n+1}\sqrt{\pi(2n+1)}\, j_n(k_0 r) \qquad m = -1,1 \tag{3.52}$$

$$\beta_{nm}^i(r) = m\, i^{n+1}\sqrt{\pi(2n+1)}\,\frac{1}{k_0 r}\frac{d}{dr}\big(rj_n(k_0 r)\big) \qquad m = -1,1 \tag{3.53}$$

$$\gamma_{nm}^i(r) = m\, i^{n+1}\sqrt{\pi(2n+1)}\sqrt{n(n+1)}\,\frac{1}{k_0 r}\, j_n(k_0 r) \qquad m = -1,1 \tag{3.54}$$

Similar to the case with dipole, for any $m \neq -1,1$, the coefficients are all zeros.

3.2.2.2 Dimension reduction for the object and data equations

In this sub-section the reduced object and data equations will be obtained. To this end, the series expansion defined by (3.16) and (3.38) will be used to express the total field and the incoming field respectively. Similar to the acoustic case, the main aim of this sub-section is to obtain 1-D integral equations involving the series expansion coefficients instead of the field values themselves. As the expansion defined in (3.16) contains three separate coefficients $\alpha_{nm}(r)$, $\beta_{nm}(r)$, $\gamma_{nm}(r)$; three equations will be

needed to determine the coefficients of the interior field. Therefore, the vectorial object equation (3.35) will be replaced by a system consisting of three reduced 1-D integral equations. Similarly, using (2.27) to represent scattered field, two independent 1-D integral equations will be obtained as reduced data equations.

In order to take advantage of the orthogonality relations, let us substitute the expansion for the interior field given in (3.16), and the one for the dyadic Green's function $\bar{\bar{\mathbf{G}}}_0(\mathbf{r},\mathbf{r}')$ given in (3.28) into the object equation (3.35). For the sake of compactness, we will analyze the integral appearing on the right-hand side of (3.35) in three parts as

$$\int_D \bar{\bar{\mathbf{G}}}_0(\mathbf{r},\mathbf{r}')v(r')\mathbf{E}(\mathbf{r}')dv' = I_\alpha + I_\beta + I_\gamma \tag{3.55}$$

where I_α, I_β, and I_γ represent the parts containing the terms $\alpha_{nm}(r)\mathbf{A}_{1nm}(\theta,\phi)$, $\beta_{nm}(r)\mathbf{A}_{2nm}(\theta,\phi)$, and $\gamma_{nm}(r)\mathbf{A}_{3nm}(\theta,\phi)$ of the expansion for the interior electric field respectively. Therefore, the open form of the integral I_α is defined as

$$\begin{aligned} I_\alpha = \int_D &\left\{ ik_0 \sum_{\bar{n}=0}^{\infty} \sum_{\bar{m}=-\bar{n}}^{\bar{n}} \frac{1}{\bar{n}(\bar{n}+1)} \left[\mathbf{M}_{\bar{n}\bar{m}}(k_0\mathbf{r})\mathbf{M}^*_{\bar{n}\bar{m}}(k_0\mathbf{r}') + \mathbf{N}_{\bar{n}\bar{m}}(k_0\mathbf{r})\mathbf{N}^*_{\bar{n}\bar{m}}(k_0\mathbf{r}') \right] \right. \\ &\left. - \frac{\hat{r}\hat{r}}{k_0^2}\delta(\mathbf{r}\text{-}\mathbf{r}') \right\} \sum_{n=0}^{\infty} \sum_{m=-n}^{n} \left\{ \alpha_{nm}(r')\mathbf{A}_{1nm}(\theta',\phi') \right\} v(r')dv' \end{aligned} \tag{3.56}$$

where the indices $\bar{n}$, $\bar{m}$ are used to distinguish the expansion of the dyadic Green's function from the expansion for the interior electric field. In order to obtain the 1-D expression of (3.56), the structures of $\mathbf{M}_{\bar{n}\bar{m}}(k_0\mathbf{r})\mathbf{M}^*_{\bar{n}\bar{m}}(k_0\mathbf{r}')$ and $\mathbf{N}_{\bar{n}\bar{m}}(k_0\mathbf{r})\mathbf{N}^*_{\bar{n}\bar{m}}(k_0\mathbf{r}')$ must be analyzed. Note that the form of the dyad for $\bar{m}<0$ should be investigated separately. Considering (3.12), the expression of the first dyad can be determined as $\mathbf{M}_{\bar{n},|\bar{m}|}(k_0\mathbf{r}')\mathbf{M}^*_{\bar{n},|\bar{m}|}(k_0\mathbf{r})$ for $\bar{m}<0$. Now, let us state the dyad $\mathbf{M}_{\bar{n}\bar{m}}(k_0\mathbf{r})\mathbf{M}^*_{\bar{n}\bar{m}}(k_0\mathbf{r}')$ in matrix form as

$$\mathbf{M}_{\bar{n}\bar{m}}(k_0\mathbf{r})\mathbf{M}^*_{\bar{n}\bar{m}}(k_0\mathbf{r}') = \begin{bmatrix} 0 & 0 & 0 \\ 0 & MM_{\theta\theta} & MM_{\theta\phi} \\ 0 & MM_{\phi\theta} & MM_{\phi\phi} \end{bmatrix} \tag{3.57}$$

where the elements $MM_{\theta\theta}$ and $MM_{\theta\phi}$ are defined as

$$MM_{\theta\theta} = \begin{cases} \bar{n}(\bar{n}+1)\, j_{\bar{n}}(k_0 r_<)h_{\bar{n}}^{(1)}(k_0 r_>) \\ \bar{n}(\bar{n}+1)\, j_{\bar{n}}(k_0 r_<)h_{\bar{n}}^{(1)}(k_0 r_>) \end{cases}$$
$$\times \left[\mathbf{A}_{1\bar{n}\bar{m}}(\theta,\phi)\right]_\theta \left[\mathbf{A}_{1\bar{n}\bar{m}}^*(\theta',\phi')\right]_\theta \quad \bar{m} \geq 0 \qquad (3.58)$$
$$\times \left[\mathbf{A}_{1\bar{n},|\bar{m}|}^*(\theta,\phi)\right]_\theta \left[\mathbf{A}_{1\bar{n},|\bar{m}|}(\theta',\phi')\right]_\theta \quad \bar{m} < 0$$

and

$$MM_{\theta\phi} = \begin{cases} \bar{n}(\bar{n}+1)\, j_{\bar{n}}(k_0 r_<)h_{\bar{n}}^{(1)}(k_0 r_>) \\ \bar{n}(\bar{n}+1)\, j_{\bar{n}}(k_0 r_<)h_{\bar{n}}^{(1)}(k_0 r_>) \end{cases}$$
$$\times \left[\mathbf{A}_{1\bar{n}\bar{m}}(\theta,\phi)\right]_\theta \left[\mathbf{A}_{1\bar{n}\bar{m}}^*(\theta',\phi')\right]_\phi \quad \bar{m} \geq 0 \qquad (3.59)$$
$$\times \left[\mathbf{A}_{1\bar{n},|\bar{m}|}^*(\theta,\phi)\right]_\theta \left[\mathbf{A}_{1\bar{n},|\bar{m}|}(\theta',\phi')\right]_\phi \quad \bar{m} < 0$$

In (3.58) and (3.59), the signs $[\Box]_\theta$ and $[\Box]_\phi$ denote the $\hat{\theta}$ and $\hat{\phi}$ components of the related functions respectively. The remaining matrix elements $MM_{\phi\theta}$ and $MM_{\phi\phi}$ can be written in a similar fashion. Since the vector wave functions $\mathbf{M}_{\bar{n}\bar{m}}(k_0\mathbf{r})$ do not have an $\hat{r}$ component, the related matrix elements are all zeros. To comlete the matrix notation, we also express the term $\alpha_{nm}(r')\mathbf{A}_{1nm}(\theta',\phi')$ as a matrix:

$$\alpha_{nm}(r')\mathbf{A}_{1nm}(\theta',\phi') = \begin{bmatrix} 0 & \alpha A_\theta & \alpha A_\phi \end{bmatrix}^T \qquad (3.60)$$

Here the term αA_θ can be expressed in an open form as

$$\alpha A_\theta = \begin{cases} \alpha_{nm}(r')\left[\mathbf{A}_{1nm}(\theta',\phi')\right]_\theta & m \geq 0 \\ \alpha_{nm}(r')(-1)^{|m|}\left[\mathbf{A}_{1n,|m|}^*(\theta',\phi')\right]_\theta & m < 0 \end{cases} \qquad (3.61)$$

The remaining term, αA_ϕ in (3.60), can be expressed in a similar form using $\hat{\phi}$ component. In order to obtain the kernel of the integral I_α, one can use the matrices introduced in (3.57) and (3.60). It is clear that the result of the matrix product will be a vector whose components are given by

$$\begin{bmatrix} 0 & 0 & 0 \\ 0 & MM_{\theta\theta} & MM_{\theta\phi} \\ 0 & MM_{\phi\theta} & MM_{\phi\phi} \end{bmatrix} \begin{bmatrix} 0 \\ \alpha A_\theta \\ \alpha A_\phi \end{bmatrix} = \begin{bmatrix} 0 \\ MA_\theta \\ MA_\phi \end{bmatrix} \tag{3.62}$$

where the open form of the $\hat{\theta}$ component, denoted as MA_θ, can be stated as

$$MA_\theta = \begin{cases} \bar{n}(\bar{n}+1)\, j_{\bar{n}}(k_0 r_<)h_{\bar{n}}^{(1)}(k_0 r_>)\alpha_{nm}(r')\left[\mathbf{A}_{1\bar{n}\bar{m}}(\theta,\phi)\right]_\theta \\ \bar{n}(\bar{n}+1)\, j_{\bar{n}}(k_0 r_<)h_{\bar{n}}^{(1)}(k_0 r_>)\alpha_{nm}(r')\left[\mathbf{A}_{1\bar{n},|\bar{m}|}^*(\theta,\phi)\right]_\theta (-1)^{|\bar{m}|} \\ \times\left\{\mathbf{A}_{1\bar{n}\bar{m}}^*(\theta',\phi')\cdot\mathbf{A}_{1nm}(\theta',\phi')\right\} \quad \bar{m}\geq 0 \\ \times\left\{\mathbf{A}_{1\bar{n},|\bar{m}|}(\theta',\phi')\cdot\mathbf{A}_{1n,|m|}^*(\theta',\phi')\right\} \quad \bar{m}<0 \end{cases} \tag{3.63}$$

Once again, the $\hat{\phi}$ component MA_ϕ will not be stated here, since its form is similar to (3.63). It is clear from (3.63) that, for any $\bar{m}\neq m$ and $\bar{n}\neq n$, the result of the integral I_α will be zero due to the orthogonality of the functions $\mathbf{A}_{1nm}$ over unit spherical surface. Therefore the series expansion of the dyadic Green's function $\bar{\bar{\mathbf{G}}}_0(\mathbf{r},\mathbf{r}')$ with terms $\bar{n},\bar{m}$ can be discarded. Moreover, the analysis presented above demonstrates that the dyad $\mathbf{N}_{\bar{n}\bar{m}}(k_0\mathbf{r})\mathbf{N}_{\bar{n}\bar{m}}^*(k_0\mathbf{r}')$ and the term with $\hat{r}\hat{r}$ will not have any contribution to I_α, since the functions $\mathbf{A}_{\tau nm}$ are orthogonal, and $\mathbf{A}_{1nm}$ have no radial component. Therefore, after putting the vectorial components together for $m<0$ and $m\geq 0$ by taking (3.12) into account, the integral I_α can be restated as

$$I_\alpha = \sum_{n=0}^{\infty}\sum_{m=-n}^{n} ik_0\mathbf{A}_{1nm}(\theta,\phi)\int_0^a n(n+1)\, j_n(k_0 r_<)h_n^{(1)}(k_0 r_>)\alpha_{nm}(r')v(r')r'^2 dr'$$
$$\times\int_0^{2\pi}\int_0^{\pi}\mathbf{A}_{1nm}(\theta',\phi')\cdot\mathbf{A}_{1nm}^*(\theta',\phi')\sin\theta' d\theta' d\phi' \tag{3.64}$$

It is clear that the last integral in (3.64) is a direct application of the orthogonality relation. Therefore, the final 1-D form of the integral can be obtained by carrying the integration over the unit spherical surface:

79

$$I_{\alpha} = \sum_{n=0}^{\infty} \sum_{m=-n}^{n} ik_0 \mathbf{A}_{1nm}(\theta, \phi)$$
$$\times \int_0^a n(n+1) \, j_n(k_0 r_<) h_n^{(1)}(k_0 r_>) \alpha_{nm}(r') v(r') r'^2 dr'$$

(3.65)

Note that the functions $\mathbf{A}_{1nm}(\theta, \phi)$ appearing in (3.65) are functions of $\mathbf{r}$ coordinates instead of $\mathbf{r}'$. This term will be eliminated in later stages by using the orthogonality condition for $\mathbf{r}$ coordinates.

Next, for the integrals I_{β} and I_{γ}, the procedure will be similar. It is clear that for these integrals the dyad $\mathbf{M}_{\bar{n}\bar{m}}(k_0\mathbf{r})\mathbf{M}_{\bar{n}\bar{m}}^*(k_0\mathbf{r}')$ will not make any contribution due to the orthogonality. Hence, this time we should express $\mathbf{N}_{\bar{n}\bar{m}}(k_0\mathbf{r})\mathbf{N}_{\bar{n}\bar{m}}^*(k_0\mathbf{r}')$ as a matrix in order to obtain 1-D forms of the integrals:

$$\mathbf{N}_{\bar{n}\bar{m}}(k_0\mathbf{r})\mathbf{N}_{\bar{n}\bar{m}}^*(k_0\mathbf{r}') = \begin{bmatrix} NN_{rr} & NN_{r\theta} & NN_{r\phi} \\ NN_{\theta r} & NN_{\theta\theta} & MM_{\theta\phi} \\ NN_{\phi r} & MM_{\phi\theta} & MM_{\phi\phi} \end{bmatrix}$$

(3.66)

Note that all the matrix elements are non-zeros, since the vector wave functions $\mathbf{N}_{\bar{n}\bar{m}}(k_0\mathbf{r})$ contains both $\mathbf{A}_{2nm}$ and $\mathbf{A}_{3nm}$. We will state some of the terms in (3.66) in open form in order to illucidate the matrix structure. Expectedly, the angular part of the term NN_{rr} consists solely of the functions $\mathbf{A}_{3nm}$:

$$NN_{rr} = \frac{\bar{n}^2(\bar{n}+1)^2}{k_0^2 r r'} j_{\bar{n}}(k_0 r_<) h_{\bar{n}}^{(1)}(k_0 r_>)$$
$$\times \begin{cases} \mathbf{A}_{3\bar{n}\bar{m}}(\theta, \phi)\mathbf{A}_{3\bar{n}\bar{m}}^*(\theta', \phi') & \bar{m} \geq 0 \\ \mathbf{A}_{3\bar{n},|\bar{m}|}^*(\theta, \phi)\mathbf{A}_{3\bar{n},|\bar{m}|}(\theta', \phi') & \bar{m} < 0 \end{cases}$$

(3.67)

Similarly, for the terms $NN_{\theta\theta}$, $NN_{\theta\phi}$, $NN_{\phi\theta}$, $NN_{\phi\phi}$, the angular parts will be formed by the $\hat{\theta}$ and $\hat{\phi}$ components of the functions $\mathbf{A}_{2nm}$. Since the structure of these terms are very similar to those presented in (3.58)-(3.59), they will not be stated here. On the other hand, the remaining terms are the results of the coupling between the functions $\mathbf{A}_{2nm}$ and $\mathbf{A}_{3nm}$ within the dyad $\mathbf{N}_{\bar{n}\bar{m}}(k_0\mathbf{r})\mathbf{N}_{\bar{n}\bar{m}}^*(k_0\mathbf{r}')$, and they will effect the outcome

of the dimension reduction process by causing the 1-D reduced integral equations to be dependent. The open form of the terms

$$NN_{r\theta} = \frac{\left[\bar{n}(\bar{n}+1)\right]^{\frac{3}{2}}}{k_0^2 rr'} \left\{ \begin{array}{l} h_{\bar{n}}^{(1)}(k_0 r)\dfrac{\partial}{\partial r'}\left[r'j_{\bar{n}}(k_0 r')\right] \\[3mm] j_{\bar{n}}(k_0 r)\dfrac{\partial}{\partial r'}\left[r'h_{\bar{n}}^{(1)}(k_0 r')\right] \end{array} \right\}$$
$$\times \left\{ \begin{array}{ll} \mathbf{A}_{3\bar{n}\bar{m}}(\theta,\phi)\left[\mathbf{A}_{2\bar{n}\bar{m}}^{*}(\theta',\phi')\right]_{\theta} & \bar{m}\geq 0 \\[3mm] \mathbf{A}_{3\bar{n},|\bar{m}|}^{*}(\theta,\phi)\left[\mathbf{A}_{2\bar{n},|\bar{m}|}(\theta',\phi')\right]_{\theta} & \bar{m}<0 \end{array} \right. \tag{3.68}$$

and

$$NN_{\theta r} = \frac{\left[\bar{n}(\bar{n}+1)\right]^{\frac{3}{2}}}{k_0^2 rr'} \left\{ \begin{array}{l} j_{\bar{n}}(k_0 r')\dfrac{\partial}{\partial r}\left[r\,h_{\bar{n}}^{(1)}(k_0 r)\right] \\[3mm] h_{\bar{n}}^{(1)}(k_0 r')\dfrac{\partial}{\partial r}\left[r\,j_{\bar{n}}(k_0 r)\right] \end{array} \right\}$$
$$\times \left\{ \begin{array}{ll} \left[\mathbf{A}_{2\bar{n}\bar{m}}(\theta,\phi)\right]_{\theta}\mathbf{A}_{3\bar{n}\bar{m}}^{*}(\theta',\phi') & \bar{m}\geq 0 \\[3mm] \left[\mathbf{A}_{2\bar{n},|\bar{m}|}^{*}(\theta,\phi)\right]_{\theta}\mathbf{A}_{3\bar{n},|\bar{m}|}(\theta',\phi') & \bar{m}<0 \end{array} \right. \tag{3.69}$$

clearly demonstrate the coupling effect. In (3.68), the term $h_{\bar{n}}^{(1)}(k_0 r)\dfrac{\partial}{\partial r'}\left[r'j_{\bar{n}}(k_0 r')\right]$

must be used for $r>r'$, and $j_{\bar{n}}(k_0 r)\dfrac{\partial}{\partial r'}\left[r'h_{\bar{n}}^{(1)}(k_0 r')\right]$ for $r<r'$. Similarly, in (3.69),

$j_{\bar{n}}(k_0 r')\dfrac{\partial}{\partial r}\left[r\,h_{\bar{n}}^{(1)}(k_0 r)\right]$ and $h_{\bar{n}}^{(1)}(k_0 r')\dfrac{\partial}{\partial r}\left[r\,j_{\bar{n}}(k_0 r)\right]$ must be chosen for the cases of

$r>r'$ and $r<r'$ respectively. In order to obtain the 1-D form of the integral I_β, one

must express the vectorial functions $\beta_{nm}(r')\mathbf{A}_{2nm}(\theta',\phi')$ as a matrix in a form similar

to (3.60), and repeat the procedure outlined in (3.62)-(3.65) by using (3.67) instead of

(3.62). By applying the orthogonality relations for angular terms, the final form of the

integral is obtained as

$$I_\beta = \sum_{n=0}^{\infty} \sum_{m=-n}^{n} \mathbf{A}_{3nm}(\theta,\phi) \frac{i\sqrt{n(n+1)}}{k_0 r}$$

$$\times \int_0^a \left\{ \begin{array}{l} h_n^{(1)}(k_0 r) \dfrac{\partial}{\partial r'}\left[r' j_n(k_0 r') \right] \\[2mm] j_n(k_0 r) \dfrac{\partial}{\partial r'}\left[r' h_n^{(1)}(k_0 r') \right] \end{array} \right\} \beta_{nm}(r') v(r') r' dr'$$

$$+ \sum_{n=0}^{\infty} \sum_{m=-n}^{n} \mathbf{A}_{2nm}(\theta,\phi) \frac{i}{k_0 r} \int_0^a \frac{\partial}{\partial r_<}\left[r_< j_n(k_0 r_<) \right]$$

$$\times \frac{\partial}{\partial r_>}\left[r_> h_n^{(1)}(k_0 r_>) \right] \beta_{nm}(r') v(r') \, r' dr' \tag{3.70}$$

First term in (3.70) which contains $\mathbf{A}_{3nm}(\theta,\phi)$, is the result of the terms $NN_{r\theta}$ and $NN_{r\phi}$ in (3.66). Note that the term with the dyad $\hat{r}\hat{r}$ in $\bar{\bar{\mathbf{G}}}_0(\mathbf{r},\mathbf{r}')$ had no effect on I_β, since the functions $\mathbf{A}_{2nm}(\theta,\phi)$ have no radial component.

Finally, to obtain the 1-D form of I_γ, one must use $\gamma_{nm}(r')\mathbf{A}_{3nm}(\theta',\phi')$ alongside (3.66) in a fashion similar to the previous integrals. However, since the functions $\mathbf{A}_{3nm}$ have a radial component, the additional $\hat{r}\hat{r}$ term in $\bar{\bar{\mathbf{G}}}_0(\mathbf{r},\mathbf{r}')$ must be taken into account. It is clear that the integration of $\gamma_{nm}(r')\mathbf{A}_{3nm}(\theta',\phi')$, i.e. $\gamma_{nm}(r')Y_{nm}(\theta',\phi')\hat{r}$, with the dyad $\hat{r}\hat{r}$ will yield a vectorial function with $\hat{r}$ component. Considering the mathematical properties of the Dirac delta function, the result of the integral can be calculated as

$$\int_D \frac{\hat{r}\hat{r}}{k_0^2} \sum_{n=0}^{\infty} \sum_{m=-n}^{n} \gamma_{nm}(r')Y_{nm}(\theta',\phi')\hat{r}\, v(r')\delta(\mathbf{r} \text{-} \mathbf{r}')dv' =$$

$$\sum_{n=0}^{\infty} \sum_{m=-n}^{n} \frac{v(r)}{k_0^2}\gamma_{nm}(r)\mathbf{A}_{3nm}(\theta,\phi) \tag{3.71}$$

Note that the left hand side of (3.71) consists solely of functions of $\mathbf{r}$ coordinates due to the integration with Dirac delta function. Therefore, the contribution of this term in the final form of the reduced object equations will be different from the other terms. Adding the left hand side of (3.71) to the result of the integration with the dyad $\mathbf{N}_{\bar{n}\bar{m}}(k_0\mathbf{r})\mathbf{N}_{\bar{n}\bar{m}}^*(k_0\mathbf{r}')$ yields the 1-D form of the integral I_γ as

$$I_\gamma = \sum_{n=0}^{\infty} \sum_{m=-n}^{n} \mathbf{A}_{2nm}(\theta,\phi) \frac{i\sqrt{n(n+1)}}{k_0 r}$$

$$\times \int_0^a \left\{ \begin{array}{l} j_n(k_0 r') \dfrac{\partial}{\partial r}\left[r\, h_n^{(1)}(k_0 r) \right] \\[2mm] h_n^{(1)}(k_0 r') \dfrac{\partial}{\partial r}\left[r\, j_n(k_0 r) \right] \end{array} \right\} \gamma_{nm}(r') v(r') r' dr'$$

$$+ \sum_{n=0}^{\infty} \sum_{m=-n}^{n} \mathbf{A}_{3nm}(\theta,\phi) \frac{in(n+1)}{k_0 r} \int_0^a h_n^{(1)}(k_0 r_>) j_n(k_0 r_<)$$

$$\times \gamma_{nm}(r') v(r')\, r' dr' + \sum_{n=0}^{\infty} \sum_{m=-n}^{n} \mathbf{A}_{3nm}(\theta,\phi) \frac{v(r)}{k_0^2} \gamma_{nm}(r) \qquad (3.72)$$

Similar to I_β, the first term with $\mathbf{A}_{2nm}(\theta,\phi)$ reflects the effect of the coupling, and it is a result of the terms $NN_{\theta r}$ and $NN_{\phi r}$ in (3.66). On the other hand, the last term in (3.72) stems from (3.71).

At this point, the series expansions for all terms in (3.35) is completed. The vector spherical harmonics appearing in the series expansions are all functions of **r** coordinates, and therefore they can be eliminated using orthogonality relations. Before that operation, we represent the expanded form of the object equation by substituting (3.16), (3.38), (3.65), (3.70), and (3.72) into (3.35):

$$\sum_{n=0}^{\infty} \sum_{m=-n}^{n} \left\{ \alpha_{nm}(r)\mathbf{A}_{1nm}(\theta,\phi) + \beta_{nm}(r)\mathbf{A}_{2nm}(\theta,\phi) + \gamma_{nm}(r)\mathbf{A}_{3nm}(\theta,\phi) \right\} =$$

$$\sum_{n=0}^{\infty} \sum_{m=-n}^{n} \left\{ \alpha_{nm}^i(r)\mathbf{A}_{1nm}(\theta,\phi) + \beta_{nm}^i(r)\mathbf{A}_{2nm}(\theta,\phi) + \gamma_{nm}^i(r)\mathbf{A}_{3nm}(\theta,\phi) \right\}$$

$$+ \sum_{n=0}^{\infty} \sum_{m=-n}^{n} ik_0^3 \mathbf{A}_{1nm}(\theta,\phi) \int_0^a n(n+1)\, j_n(k_0 r_<) h_n^{(1)}(k_0 r_>) \alpha_{nm}(r') v(r') r'^2 dr'$$

$$+ \sum_{n=0}^{\infty} \sum_{m=-n}^{n} \mathbf{A}_{3nm}(\theta,\phi) \frac{ik_0\sqrt{n(n+1)}}{r} \int_0^a \left\{ \begin{array}{l} h_n^{(1)}(k_0 r) \dfrac{\partial}{\partial r'}\left[r' j_n(k_0 r') \right] \\[2mm] j_n(k_0 r) \dfrac{\partial}{\partial r'}\left[r' h_n^{(1)}(k_0 r') \right] \end{array} \right\} \qquad (3.73)$$

$$\times \beta_{nm}(r') v(r') r' dr' + \sum_{n=0}^{\infty} \sum_{m=-n}^{n} \mathbf{A}_{2nm}(\theta,\phi) \frac{ik_0}{r} \int_0^a \frac{\partial}{\partial r_<}\left[r_< j_n(k_0 r_<) \right]$$

$$\times \frac{\partial}{\partial r_>}\left[r_> h_n^{(1)}(k_0 r_>) \right] \beta_{nm}(r') v(r') r' dr' + \sum_{n=0}^{\infty} \sum_{m=-n}^{n} \mathbf{A}_{2nm}(\theta,\phi) \frac{ik_0\sqrt{n(n+1)}}{r}$$

$$\times \int_0^a \left\{ \begin{matrix} j_n(k_0 r') \dfrac{\partial}{\partial r}\left[r\, h_n^{(1)}(k_0 r) \right] \\[4pt] h_n^{(1)}(k_0 r') \dfrac{\partial}{\partial r}\left[r\, j_n(k_0 r) \right] \end{matrix} \right\} \gamma_{nm}(r')v(r')r'dr' + \sum_{n=0}^{\infty}\sum_{m=-n}^{n} \mathbf{A}_{3nm}(\theta,\phi)$$

$$\times \left\{ \frac{ik_0 n(n+1)}{r}\int_0^a h_n^{(1)}(k_0 r_>)\, j_n(k_0 r_<)\gamma_{nm}(r')v(r')r'dr' + \gamma_{nm}(r)v(r) \right\}$$

Note that each term in (3.73) consists of a vector spherical harmonic $\mathbf{A}_{\tau nm}(\theta,\phi)$, coefficients of series expansions for interior or incident electric fields, and a 1-D integral along the radial direction. Therefore, to obtain a completely 1-D formulation, the vector spherical harmonics must be eliminated. Since each $\mathbf{A}_{\tau nm}(\theta,\phi)$ in (3.73) is a function of $\mathbf{r}$ coordinates, orthogonality relations can be applied in a straightforward manner to achieve this objective. That is, by multiplying both sides of (3.73) with the complex conjugate of each $\mathbf{A}_{\tau nm}(\theta,\phi)$ separately, and integrating over the unit spherical surface; one can obtain three 1-D integral equations for the coefficients $\alpha_{nm}(r)$, $\beta_{nm}(r)$, and $\gamma_{nm}(r)$. We first apply this procedure with the function $\mathbf{A}_{1nm}^{*}(\theta,\phi)$ to obtain the first reduced object equation

$$\alpha_{nm}(r) = \alpha_{nm}^{i}(r) + ik_0^3 \int_0^a n(n+1)\, j_n(k_0 r_<)h_n^{(1)}(k_0 r_>)\alpha_{nm}(r')v(r')r'^2 dr' \tag{3.74}$$

(3.74), contains only the coefficients $\alpha_{nm}(r)$, since it is the only coefficient that is related to the vector wave functions $\mathbf{M}_{nm}(k_0\mathbf{r})$. Note that the form of the reduced 1-D integral equation (3.74) is similar to the acoustic reduced object equation (2.51). Therefore, one can determine the coefficients $\alpha_{nm}(r)$ by solving (3.74) independently through discretization of the interval $r' \in [0,a]$, in a fashion identical to the one presented for the acoustic case in Appendix A. For the remaining coefficients, the procedure will be similar. However, due to the coupling effect demonstrated earlier, separate equations for each coefficient cannot be formed. Now, to produce the second reduced object equation, let us apply the same procedure with the function $\mathbf{A}_{2nm}^{*}(\theta,\phi)$ to obtain

$$\beta_{nm}(r) = \beta_{nm}^i(r) + \frac{ik_0}{r} \int_0^a \frac{\partial}{\partial r_<} \left[r_< j_n(k_0 r_<) \right] \frac{\partial}{\partial r_>} \left[r_> h_n^{(1)}(k_0 r_>) \right]$$

$$\times \beta_{nm}(r') v(r') r' dr' + \frac{ik_0 \sqrt{n(n+1)}}{r} \int_0^a \left\{ \begin{array}{c} j_n(k_0 r') \frac{\partial}{\partial r} \left[r h_n^{(1)}(k_0 r) \right] \\ h_n^{(1)}(k_0 r') \frac{\partial}{\partial r} \left[r j_n(k_0 r) \right] \end{array} \right\} \tag{3.75}$$

$$\times \gamma_{nm}(r') v(r') r' dr'$$

Finally, using $\mathbf{A}_{3nm}^*(\theta, \phi)$, the third reduced object equation can be formed as

$$\gamma_{nm}(r) = \frac{\gamma_{nm}^i(r)}{v(r)+1} + \frac{ik_0 n(n+1)}{[v(r)+1]r} \int_0^a h_n^{(1)}(k_0 r_>) j_n(k_0 r_<) \gamma_{nm}(r') v(r') r' dr'$$

$$+ \frac{ik_0 \sqrt{n(n+1)}}{[v(r)+1]r} \int_0^a \left\{ \begin{array}{c} h_n^{(1)}(k_0 r) \frac{\partial}{\partial r'} \left[r' j_n(k_0 r') \right] \\ j_n(k_0 r) \frac{\partial}{\partial r'} \left[r' h_n^{(1)}(k_0 r') \right] \end{array} \right\} \beta_{nm}(r') v(r') r' dr' \tag{3.76}$$

The term $[v(r)+1]$ appearing in (3.76) stems from the term with $\hat{r}\hat{r}$ dyad in $\bar{\bar{\mathbf{G}}}_0(\mathbf{r},\mathbf{r}')$ As demonstrated in (3.71), that term makes a contribution in the $\mathbf{r}$ coordinates for the coefficient $\gamma_{nm}(r)$, which is reflected in the last term of (3.73). It is clear from the appearance of the coefficients $\beta_{nm}(r')$ and $\gamma_{nm}(r')$ in both equations that, (3.75)-(3.76) are coupled, and form a system of equations. Therefore, the discretization procedure of Appendix A should be slightly altered. For a discretization into P sub-interval, the coefficient matrix will be of the form $K = [K_{\beta\beta} \ K_{\beta\gamma}; K_{\gamma\beta} \ K_{\gamma\gamma}]$. Here, these four sub-matrices are of size $P \times P$. The elements of $K_{\beta\beta}$ and $K_{\beta\gamma}$ will be determined from the integrals in (3.75) containing $\beta_{nm}(r')$ and $\gamma_{nm}(r')$ respectively. Similarly, $K_{\gamma\beta}$ and $K_{\gamma\gamma}$ will be formed using the integrals in (3.76). It is clear that K will have a size of $2P \times 2P$, and solving the resulting discretized equation would provide the coefficients $\beta_{nm}(r)$ and $\gamma_{nm}(r)$ simultaneously.

Therefore, one can solve the system of reduced object equations (3.74)-(3.76) to obtain the coefficients of the interior electic field $\alpha_{nm}(r)$, $\beta_{nm}(r)$, and $\gamma_{nm}(r)$. After determining the coefficients, it is possible to calculate the total electric field inside the

sphere using (3.16). Note that the coefficients $\alpha_{nm}^i(r)$, $\beta_{nm}^i(r)$, and $\gamma_{nm}^i(r)$ appearing in (3.74)-(3.76) are the coefficients of the incident field. The open forms of these coefficients were given in (3.46)-(3.48) for the infinitesimal horizontal electric dipole, and in (3.52)-(3.54) for the x-polarized plane wave. Finally, for the scattered field the 3-D vectorial data equation (3.36) must be transformed in a manner similar to (3.35). Since both equations have similar structures, the related dimension reduction processes would be identical. Note that in the region outside the sphere $r > r'$, since $r' \in [0,a]$; and the object function $v(r)$ is zero. Considering these conditions, the expanded form of (3.36) can be written for $|\mathbf{r}| > a$ as

$$
\begin{aligned}
\mathbf{E}^s(\mathbf{r}) = &\sum_{n=0}^{\infty}\sum_{m=-n}^{n} ik_0^3 \mathbf{A}_{1nm}(\theta,\phi) h_n^{(1)}(k_0 r) \int_0^a n(n+1)\, j_n(k_0 r') v(r') \\
&\times \alpha_{nm}(r') r'^2 dr' + \sum_{n=0}^{\infty}\sum_{m=-n}^{n} \mathbf{A}_{2nm}(\theta,\phi) \frac{ik_0}{r}\frac{\partial}{\partial r}\left[r h_n^{(1)}(k_0 r)\right] \\
&\times \int_0^a \frac{\partial}{\partial r'}\left[r' j_n(k_0 r')\right]\beta_{nm}(r') v(r') r' dr' + \sum_{n=0}^{\infty}\sum_{m=-n}^{n} \mathbf{A}_{2nm}(\theta,\phi) \frac{ik_0\sqrt{n(n+1)}}{r} \\
&\times \frac{\partial}{\partial r}\left[r h_n^{(1)}(k_0 r)\right] \int_0^a j_n(k_0 r')\gamma_{nm}(r') v(r') r' dr' + \sum_{n=0}^{\infty}\sum_{m=-n}^{n} \mathbf{A}_{3nm}(\theta,\phi) \\
&\times \frac{ik_0\sqrt{n(n+1)}}{r} h_n^{(1)}(k_0 r)\int_0^a \frac{\partial}{\partial r'}\left[r' j_n(k_0 r')\right]\beta_{nm}(r') v(r') r' dr' \\
&+ \sum_{n=0}^{\infty}\sum_{m=-n}^{n} \mathbf{A}_{3nm}(\theta,\phi) \frac{ik_0 n(n+1)}{r} h_n^{(1)}(k_0 r)\int_0^a j_n(k_0 r')\gamma_{nm}(r') v(r') r' dr'
\end{aligned}
\tag{3.77}
$$

By comparing (3.77) with the series expansion for the scattered field defined in (3.27), one can form the reduced data equations for the scalar coefficients A_{nm} and B_{nm} of the scattered field:

$$
A_{nm} = \frac{ik_0^3}{\sqrt{n(n+1)}} \int_0^a j_n(k_0 r') v(r')\alpha_{nm}(r') r'^2 dr'
\tag{3.78}
$$

$$
\begin{aligned}
B_{nm} = \int_0^a \Bigg\{ &\beta_{nm}(r') \frac{ik_0^2}{\sqrt{n(n+1)}}\frac{\partial}{\partial r'}\left[r' j_n(k_0 r')\right] \\
&+ ik_0^2 j_n(k_0 r')\gamma_{nm}(r') \Bigg\} v(r') r' dr'
\end{aligned}
\tag{3.79}
$$

(3.78)-(3.79) constitute the reduced data equations. After solving the reduced object equations, determining the coefficients of the interior field, one can obtain the coefficients of the scattered field using these equations. The scattered field itself can be then calculated easily via (3.27).

3.2.3 Numerical simulations

In this sub-section, some numerical examples will be presented in order to test the validity of the method developed in the previous sub-sections. The result obtained by the method developed in this thesis will be compared with established alternative methods such as dyadic Green's function or MoM. We will present the results in four sub-sections. In the first part, the interior electric field calculated via the reduced integral equations (3.74)-(3.76) will be compared with the field obtained via dayadic Green's function. In the second part, the comparison with MoM will be performed for the scattered field. The advantages, in terms of efficiency and accuracy, of the method developed in this work will be demonstrated through this comparison. In the third sub-section, the field inside well-known lenses such as Luneburg or Eaton lens will be reconstructed using the reduced integral equations. The agreement of the results with the established characteristics of the lenses further proves the applicability of the method. Finally, in the fourth part, a special case with a dipole located inside the sphere will be analysed. As it will explained in that sub-section, although a rigorous mathematical formulation that removes the singularity cannot be developed, the method nevertheless provides an effective tool for determining the field distribution outside the vicinity of the source.

3.2.3.1 The comparison with the dyadic Green's function

Consider a two-layered piecewise homogeneous sphere described by

$$\varepsilon_r(r) = \begin{cases} 3.8 + 1.8i, & 0 \le r/a \le 0.5 \\ 2.4 + 1.2i, & 0.5 < r/a \le 1 \end{cases} \tag{3.80}$$

where

$$\varepsilon_r(r) = \frac{\varepsilon(r)}{\varepsilon_0} + \frac{i\sigma(r)}{\omega\varepsilon_0} \tag{3.81}$$

denotes the complex relative dielectric constant of the material. The magnetic permeability μ_0 considered constant throughout the whole space. The radius of the sphere is chosen as $a = 1m$ and it is illuminated by a dipole positioned right above the surface along the positive z direction. The outside region is assumed to be a homogeneous medium characterized by the free space parameters of ε_0 and μ_0. As stated in the previous sections, dyadic Green's functions can be used reliably in order to determine the interior and the scattered field for layered spheres. The formulation of the dyadic Green's function for a two layered sphere, developed in [52], is presented in Appendix D. Here, the result obtained by the reduced integral equations will be compared with the results produced via dyadic Green's function. For the first case the operating frequency is chosen as $f = 300\ MHz$. The variation of the magnitude of the electric field components inside the sphere, on the line defined by $\theta = \phi = \pi/4$, is calculated via both methods. The results depicted in Fig. 3.2 show an excellent agreement between two techniques. The number of terms n included in the series expansion for the interior electric field is determined as $N_{max} = 15$. The reduced integral equations (3.74)-(3.76) are discretized into 30 points along the radial direction.

Figure 3.2 : Magnitude of the total field inside the two-layered sphere, solid line corresponds to the solution with integral equations, and circles to the dyadic Green's function ($k_0 a = 2\pi$, $N_{max} = 15$).

Note that for the parameters $a = 1m$ and $f = 300 \, MHz$ used in the previous example the value $k_0 a$ is determined as $k_0 a = 2\pi$. This parameter denotes the electrical size of the sphere. In the section 2.2.3.1 of the acoustic case, it was demonstrated that number of terms included in the series expansions must be increased as higher operating frequencies are used. The same necessity also exists for the electromagnetic case. Higher values of N_{max} must be chosen for electrically larger spheres. To demonstrate this, the same configuration as the previous example will be repeated for the operating frequency of $f = 955 \, MHz$. This value is chosen in order to replicate the value of $k_0 a = 20$, which was used for the acoustic example analysed in Fig. 2.6. To make the comparison exact, the value of N_{max} is chosen as $N_{max} = 25$. In the acoustic case, an almost perfect agreement with the analytical solution was obtained for this value. However, as shown in Fig. 3.3, the results obtained via reduced integral equations differs considerably from those produced via the dyadic Green's function. Actually, even for higher values of N_{max}, a perfect match does not occur. The results presented in Fig. 3.4 demonstrate that for $N_{max} = 75$, there is good agreement between two methods, however the level of agreement is lower compared to acoustic case. It can be concluded from these simulations that the complexity of the electromagnetic problem is higher compared to the acoustic one.
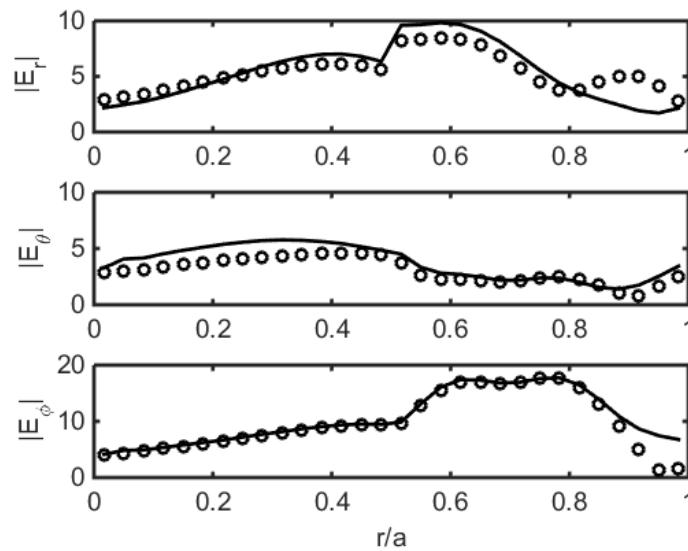
Figure 3.3 : Magnitude of the total field inside the two-layered sphere, solid line corresponds to the solution with integral equations, and circles to the dyadic Green's function ($k_0 a = 20$, $N_{max} = 25$).
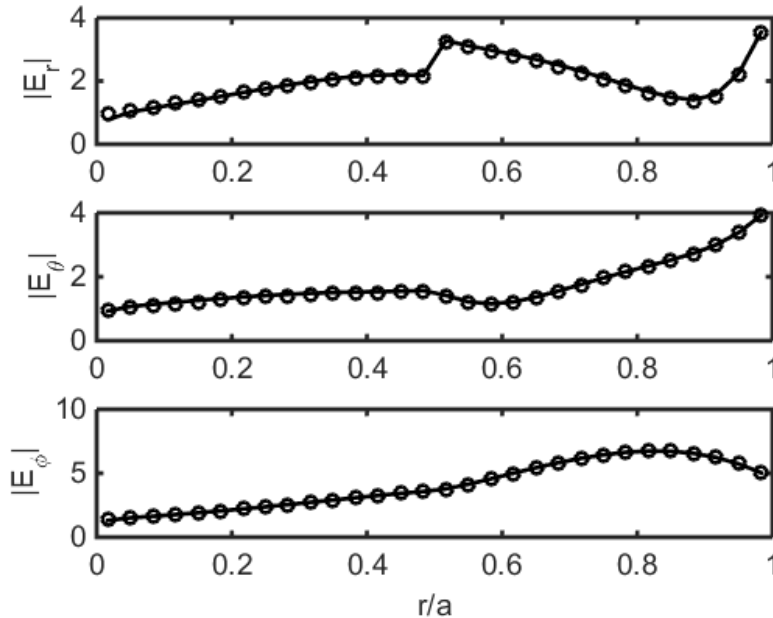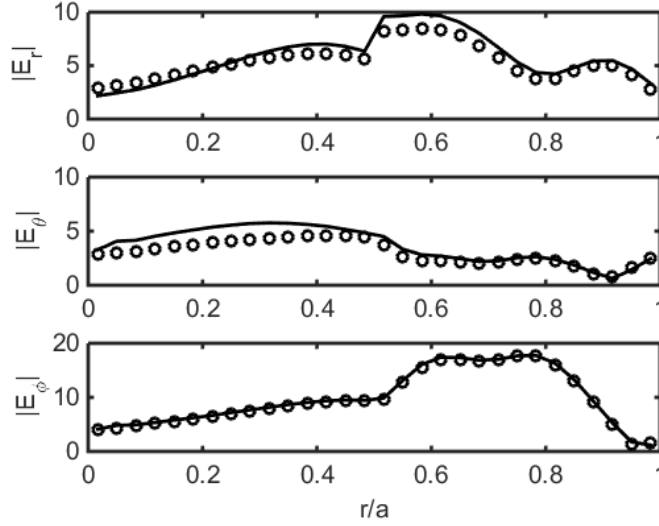
Figure 3.4 : Magnitude of the total field inside the two-layered sphere, solid line corresponds to the solution with integral equations, and circles to the dyadic Green's function ($k_0 a = 20$, $N_{max} = 75$).

3.2.3.2 Calculation of the scattered field

The dyadic Green's function can also be used to calculate the scattered field outside the sphere. Therefore, we will first calculate the scattered field for the configuration used in the first example of the previous sub-section. The integrals in (3.74)-(3.76) and those in (3.78)-(3.79) are discretized by 30 points. The number of terms included in the series expansions for the interior field and the scattered field are both chosen as $N_{max} = 15$, since the working frequency is assumed to be $f = 300 \, MHz$. The scattering cross section defined as

$$\sigma_{CS} = \lim_{r \to \infty} 4\pi r^2 \frac{\left| \mathbf{E}^s \right|^2}{\left| \mathbf{E}^i \right|^2} \tag{3.82}$$

is calculated for different values of θ, $\theta \in [0, \pi]$, in the H-plane ($\phi = \pi/2$), and in the E-plane ($\phi = 0$). For each investigated case, the scattering cross section is presented with the E-plane and the H-plane shown in the same figure, and plotted from $\theta = 0$ to $\theta = 180$, and from $\theta = 180$ to $\theta = 360$, respectively. The results given in Fig. 3.5 demonstrate that the method is in agreement with the dyadic Green's function, and can be reliably used for layered profiles.

90
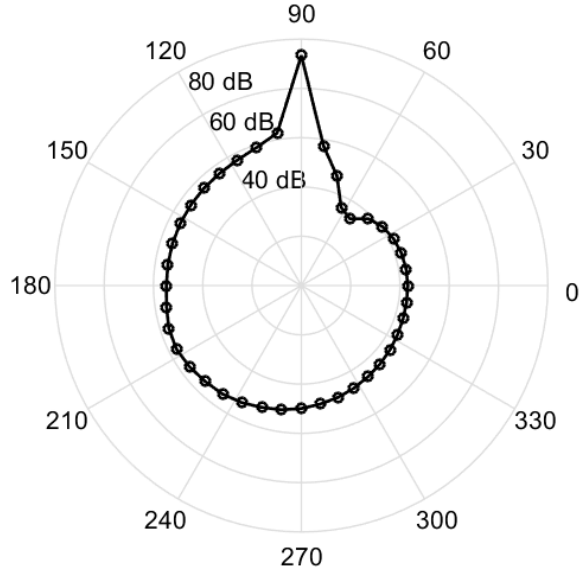
Figure 3.5 : Scattering cross section for the two layered sphere illuminated by a dipole, solid line corresponds to the solution with integral equations, and circles to the dyadic Green's function. E-plane values are given in $\theta \in [0,180]$, H-plane in $\theta \in [180,360]$.

As stated in the introduction, constructing the dyadic Green's functions for continuous profiles is much more challenging. Therefore, for this type of profiles, the comparison must be made using alternative numerical techniques. In this sub-section, the MoM formulation developed in [14] will be used for the comparison. A brief presentation of the formulation can be found in Appendix E. However, before proceeding with the comparison, the consistency and the robustness of the method developed in this thesis must be established. To this end, we will first analyze the behaviour of the scattered field coefficients in the configuration that will subsequently be used for the comparison with MoM.

For the first case of continuous profiles, consider the linearly varying profile described by

$$\varepsilon_r(r) = \left(2 - \frac{r}{a} \right) + i \left(1 - \frac{r}{a} \right). \tag{3.83}$$

In order to reduce the computational effort for MoM simulation that will be performed later, the radius of the sphere is chosen as is $a = 0.5m$, and accordingly the integrals are discretized by 15 points. The sphere is illuminated by an x-polarized plane wave

propagating along the minus z-direction with a frequency of $f = 300\ MHz$. Since the electrical size of the sphere is smaller, lower values can be used for the term N_{max}. To prove this point, the coefficients of the scattered field must be analyzed. To better depict the behaviour of the coefficients in the far field, let us use the set of coefficients $\alpha_{nm}^{s}(r)$, $\beta_{nm}^{s}(r)$, and $\gamma_{nm}^{s}(r)$ instead of the scalar coefficients A_{nm}, B_{nm} of the scattered field. That is, instead of (3.27), a series expansion in the form of (3.16) will be used:

$$
\begin{aligned}
\mathbf{E}^{s}(\mathbf{r}) = \sum_{n=0}^{\infty}\sum_{m=-n}^{n}\Big\{ &\alpha_{nm}^{s}(r)\mathbf{A}_{1nm}(\theta,\phi)+\beta_{nm}^{s}(r)\mathbf{A}_{2nm}(\theta,\phi)\\
&+\gamma_{nm}^{s}(r)\mathbf{A}_{3nm}(\theta,\phi)\Big\}
\end{aligned}
\tag{3.84}
$$

Note that the radial components of the vector wave functions $\mathbf{M}_{nm}^{(1)}(k_0\mathbf{r})$ and $\mathbf{N}_{nm}^{(1)}(k_0\mathbf{r})$ in (3.27) will be represented by the coefficients $\alpha_{nm}^{s}(r)$, $\beta_{nm}^{s}(r)$, and $\gamma_{nm}^{s}(r)$ in (3.84). This form is preferred in order to demonstrate the behaviour of the $\gamma_{nm}^{s}(r)\mathbf{A}_{3nm}(\theta,\phi)$, which represent the $\hat{r}$ component of the scattered field. Since we are investigating the scattering cross section, the far field pattern of the scattered field should be used. Therefore, the values of the coefficients at a sufficiently far radial distance of $r = 300m$, that is the values of $\alpha_{n1}^{s}(r=300)$, $\beta_{n1}^{s}(r=300)$, and $\gamma_{n1}^{s}(r=300)$, will be depicted in Fig. 3.6 and 3.7. Note that only the coefficients for $m=1$ are presented since for $m\neq\pm1$ the coefficients are all zeros, and the values for $m=-1$ have the same magnitude as the coefficients with $m=1$.

The coefficients $\alpha_{n1}^{s}(r=300)$ and $\beta_{n1}^{s}(r=300)$ are presented in the same graph in Fig. 3.6, since their magnitude are of the same scale. That shows that the vector spherical harmonics $\mathbf{A}_{1nm}(\theta,\phi)$ and $\mathbf{A}_{2nm}(\theta,\phi)$ make similar contribution to the $\hat{\theta}$ and $\hat{\phi}$ components of the scatered field. On the other hand, as depicted in Fig. 3.7, the magnitudes of the coefficients $\gamma_{n1}^{s}(r=300)$ are far lower. This is an expected result considering the fact that the far field pattern is dominated by the tangential components. Therefore the functions $\mathbf{A}_{3nm}(\theta,\phi)$, which represent the $\hat{r}$ component, do not make any significant contribution to the scattered field in the far field region. Also note that for $n\geq5$, the values of coefficients are preactically zero. This suggests that $N_{max}=5$ is an efficient choice. For any value lower than 5, there will be an error

in the scattered field, as demonstrated in Fig. 3.8. For this figure, the scattering cross section of the sphere with linearly varying profile is calculated with the reduced integral equations using $N_{max} = 3$ and $N_{max} = 5$. The difference between two results demonstrates that the coefficients with indices $n = 4$ and $n = 5$ make non-zero contributions to the scattered field. On the other hand, as expected, adding more terms with indices $n > 5$ do not effect the outcome. This will be demonstrated in Fig. 3.9.
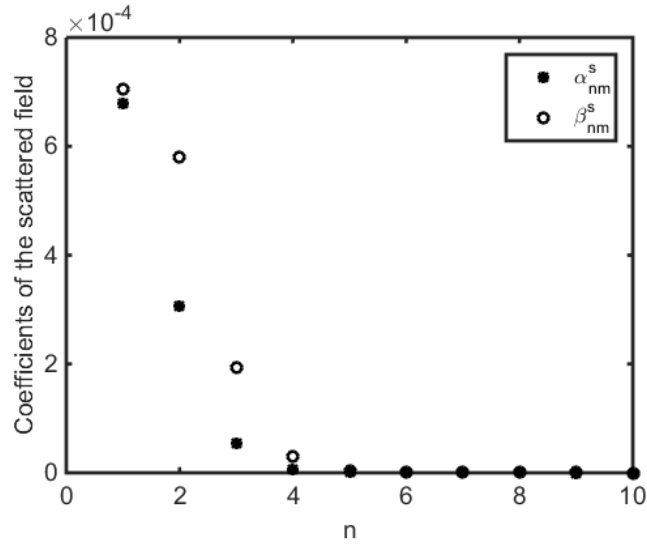
Figure 3.6 : The magnitude of the coefficients $\alpha_{n1}^{s}(r = 300)$ and $\beta_{n1}^{s}(r = 300)$ of the field scattered by a sphere with linearly varying profile.
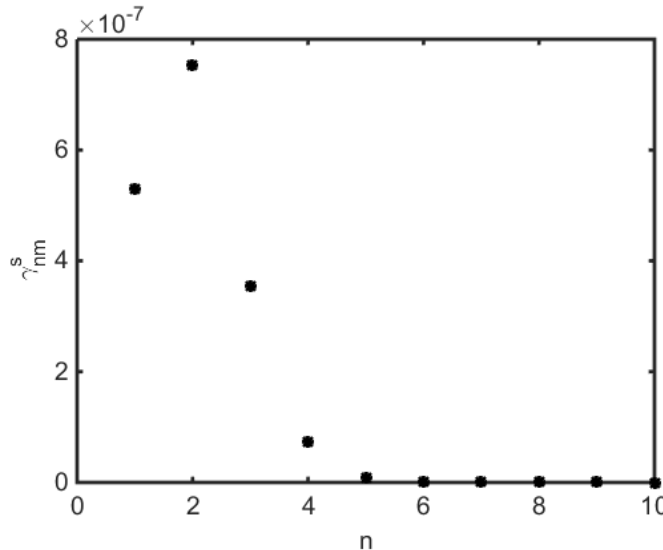
Figure 3.7 : The magnitude of the coefficients $\gamma_{n1}^{s}(r = 300)$ of the field scattered by a sphere with linearly varying profile.

Figure 3.8 : Scattering cross section for the sphere with linearly varying profile, illuminated by a plane wave travelling in the negative z-direction. Solid line corresponds to the solution with $N_{max} = 5$, and dashed line to the solution with $N_{max} = 3$. E-plane values are given in $\theta \in [0,180]$, H-plane in $\theta \in [180, 360]$.

After establishing the optimal parameters of the solution with integral equations, we can proceed to the comparison with MoM. In the method descibed in [14], the entire volume of the scatterer is discretized into cubic cells, and the electric field in the centres of those cells are evaluated by solving 3-D vectorial electric field equation via method of moments. Two different discretizations have been employed for this example. First, the dimensions of the cubic cells are chosen as $0.1m$, which corresponds to the ratio of $\lambda_0 / 10$, λ_0 being the wavelength of the free space. This is a commonly used measure in MoM applications. By this choice, the sphere is discretized into 552 cells, therefore the number of unknowns, the electric field vector components, is 1656. Secondly, a cell dimension of $0.067m$ is used for finer meshing. For this case, the number of cells and unknowns are 1791 and 5373 respectively.

On the other hand, with a discretization into 15 points, and the optimal value of $N_{max} = 5$, the number of unknowns is determined as 450 for the solution with integral equations. Note that this value indicates the number of interior electric field coefficients that will be used in (3.77). Only the coefficients with indices $m = \pm 1$ are taken into account, since the remaining coefficients are all zeros. For an electrically

larger sphere, the difference in the required computational effort would be greater as a result of the higher complexity of the MoM algorithm, which uses a 3-D discretization scheme. The scattering cross sections calculated via the reduced integral equations and MoM are plotted in Fig. 3.9. Unlike the method based on 1-D integral equations, or dyadic Green's function, which are designed specifically for symmetrical spheres, the cubic discretization only approximately represents the spherical geometry. Therefore a perfect match does not occur, although the methods are compatible in general. An important point to note is the excellent agreement between the results with $N_{max} = 5$ and $N_{max} = 10$ for the solution with integral equations. Considering the analysis presented for the previous figures of Fig. 3.6-3.8, this is an expected result, and it further demonstrates the robustness of the method developed in this thesis.
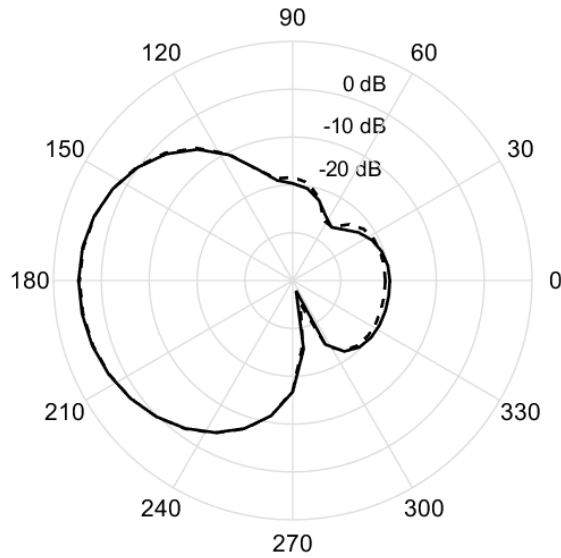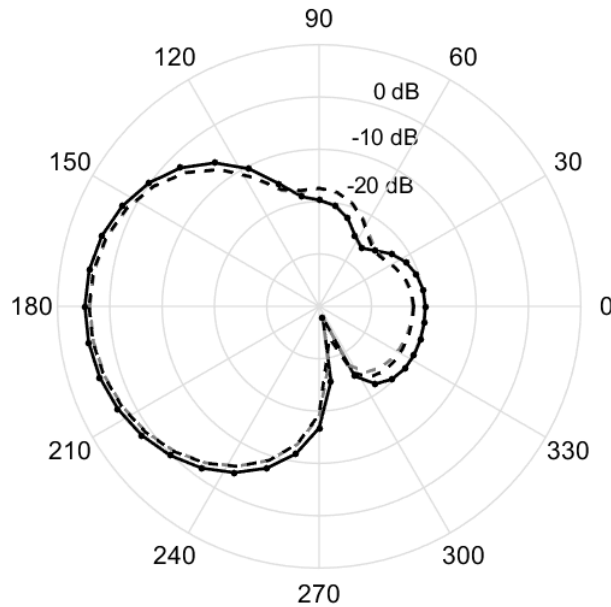

Figure 3.9 : Scattering cross section for the sphere with linearly varying profile, illuminated by a plane wave travelling in the negative z-direction. Solid line corresponds to the solution with integral equations with $N_{max} = 10$, dots to solution with $N_{max} = 5$, gray dashed line to the solution with MoM, with a cell size of $0.1m$, and black dashed line to the solution with MoM, with a cell size of $0.067m$. E-plane values are given in $\theta \in [0, 180]$, H-plane in $\theta \in [180, 360]$.
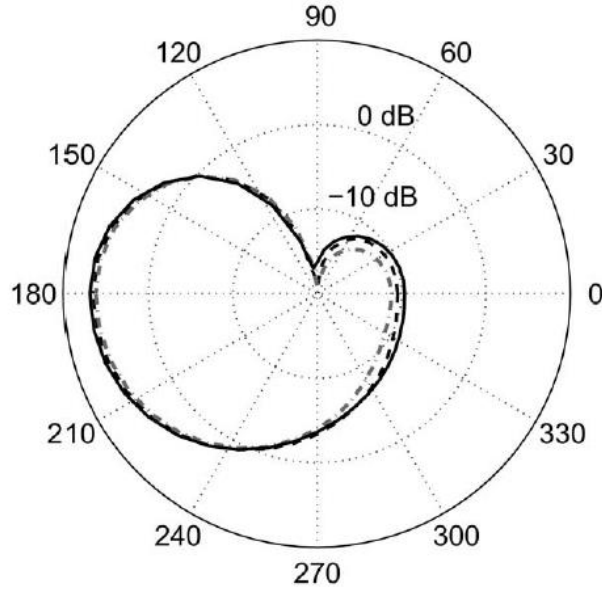
Figure 3.10 : Scattering cross section for the Eaton lens, illuminated by a plane wave travelling in the negative z-direction. Solid line corresponds to the solution with integral equations, gray dashed line to the solution with MoM, with a cell size of $0.15m$, and black dashed line to the solution with MoM, with a cell size of $0.05m$. E-plane values are given in $\theta \in [0,180]$, H-plane in $\theta \in [180,360]$.

Note that in Fig. 3.9, for the smaller cell size of $0.067m$, the result of MoM slightly approaches to the solution with integral equations. To further analyze the effect of MoM meshing, consider the Eaton lens described by

$$\varepsilon_r(r) = \left(\frac{r}{a}\right)^2. \tag{3.85}$$

The scattering cross section will be calculated with the integral equations using the same parameters as the case with linearly varying profile. For the MoM, two different discretizations will be used: First, a discretization into 136 cells with a size of $0.15m$ Second, a discretization into 4224 cells with a cell size of $0.05m$. The results are presented in Fig. 3.10. Expectedly, as the cell size decreases, the results obtained via MoM approach to the solution with integral equations. This proves that for symmetrical spheres, the method developed in this thesis presents a more efficient and accurate alternative to the classical numerical techniques such as MoM.

3.2.3.3 The field variation inside the lenses

The geometrical theory of optics provides a reliable model for predicting the field picture inside well-known lenses such as Luneburg lens [32]. Therefore, as another test for the applicability of the method, the variation of the interior electric field on the surfaces of some special lenses will be calculated via reduced integral equations. For all examples in this sub-section, the integrals are discretized by 30 points, and the value of N_{max} is chosen as $N_{max} = 20$ to guarantee accuracy. Apart from the Eaton lens defined in (3.85), the well-known Luneburg lens described by

$$\varepsilon_r(r) = 2 - \left(\frac{r}{a} \right)^2 \tag{3.86}$$

and the Maxwell fish-eye lens defined as

$$\varepsilon_r(r) = \frac{4}{\left[1 + \left(\frac{r}{a} \right)^2 \right]^2} \tag{3.87}$$

will be analysed. First, we will investigate the behaviours of the lenses in the case of excitement by a plane wave propagative along the negative z-direction with a frequency of $f = 300MHz$. In Fig. 3.11, the magnitude of the total electric field normalized with respect to the incoming field, $|\mathbf{E}| / |\mathbf{E}^i|$, on the surface is plotted for a Luneburg lens and an Eaton lens with radii of $a = 2m$. For the Luneburg lens, as predicted by the optical model, the maximum value of the field is measured on the $\theta = \pi$ axis, around the focal point of the lens [32]. Since it has a single focal point, it focuss the plane wave into its focal point which is located on the opposite side. On the other hand, the Eaton lens acts as a reflactor, and bends the incoming wave. Therefore, it creates a stronger field around the plane of $\theta = \pi/2$, compared to the region $\theta > \pi/2$

As a second example of plane wave excitation, the same value of $|\mathbf{E}| / |\mathbf{E}^i|$ is plotted for the Luneburg lens and the Maxwell fish-eye lens are plotted in Fig. 3.12. The parameters are the same as the ones used in the previous figure. It is clear that the fish-eye lens produce an evenly distributed field picture. Unlike Luneburg lens, Maxwell fish-eye lens has two focal points [32]. Therefore, in the case plane wave excitation, it

acts as a scatterer and spreads the incoming field in all directions evenly. It is clear that for plane wave excitation, the results are compatible with optical theory. The simulations demonstrate that the method can be effectively used to obtain the interior field variation not only in the radial direction, which was investigated in the section 3.2.3.1, but also in the tangential direction.

Figure 3.11 : Normalized magnitude of the interior field ($|\mathbf{E}|/|\mathbf{E}^i|$) on the surface of Eaton lens (solid line), and Luneburg lens (dashed line), induced by a plane wave travelling in the negative z-direction.

Figure 3.12 : Normalized magnitude of the interior field ($|\mathbf{E}|/|\mathbf{E}^i|$) on the surface of Maxwell fish-eye lens (solid line), and Luneburg lens (dashed line), induced by a plane wave travelling in the negative z-direction.

In the second part of this sub-section, we will produce the interior field variation on the surfaces of the lenses, in the case of excitation by a dipole. First, the Luneburg and the Maxwell fish-eye lenses will be compared. Two lenses with radii of $a = 2m$ are illuminated by an infinitesimal horizontal electric dipole situated just above the surface along the pozitive z-axis. The ratio of the field magnitudes $|\mathbf{E}|/|\mathbf{E}^i|$ for both lenses are plotted in Fig. 3.13. Since the Luneburg lens has a single focal point it distribute the field evenly in the region $\theta > \pi/2$. That is, the dipole is stuated in the focal point. On the other hand, the Maxwell lens has two focal points, and thus, it focuses the field created by the dipole in one focal point, to the other one located along the $\theta = \pi$ axis. The second example, presented in Fig. 3.14, compares the behaviour of the Eaton lens with Luneburg lens. The ratio of $|\mathbf{E}|/|\mathbf{E}^i|$, calculated for both lenses in the same configuration as the previous example, demontrates that the wave bending effect of the Eaton lens is not as effective as the plane wave excitation. Since the Eaton lens is designed as a reflector for the plane wave, this is an expected result. Nevertheless, comparison with Luneburg lens shows that it still supresses the field in the region $\theta > \pi/2$. In general, the analysis of the lenses provides another verification for the effectiveness of the method.
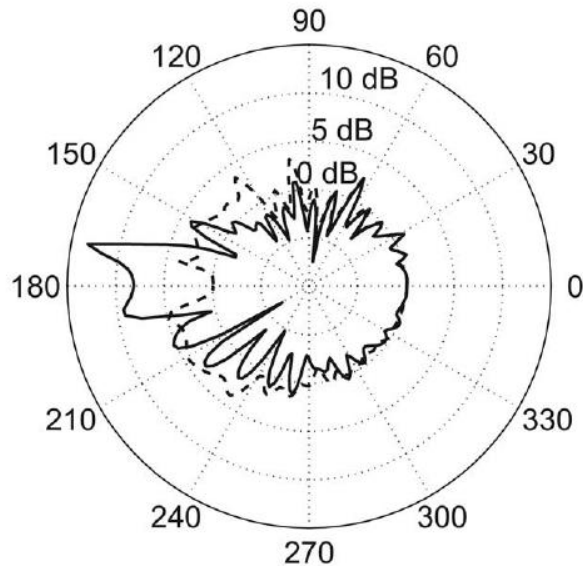
Figure 3.13 : Normalized magnitude of the interior field ($|\mathbf{E}|/|\mathbf{E}^i|$) on the surface of Maxwell fish-eye lens (solid line), and Luneburg lens (dashed line), induced by an infinitesimal dipole on the surface along the positive z-axis.
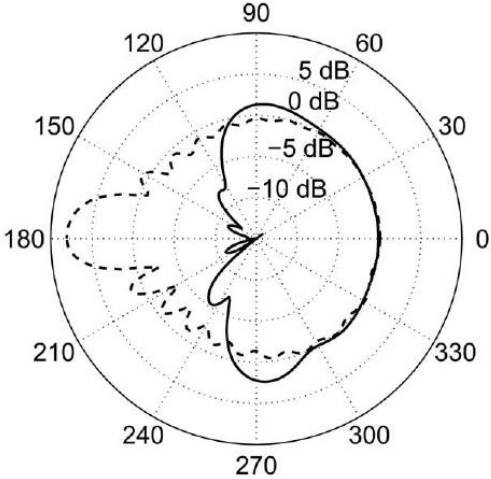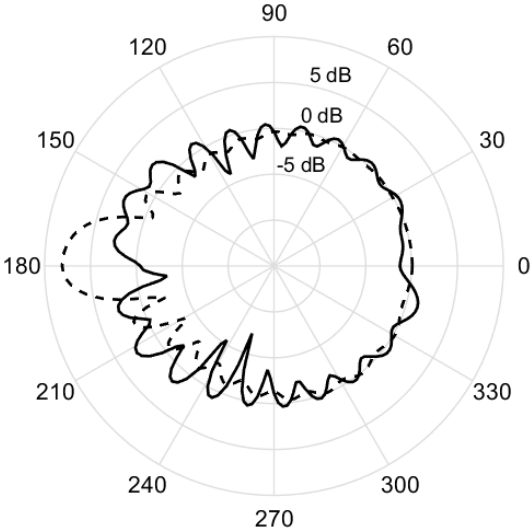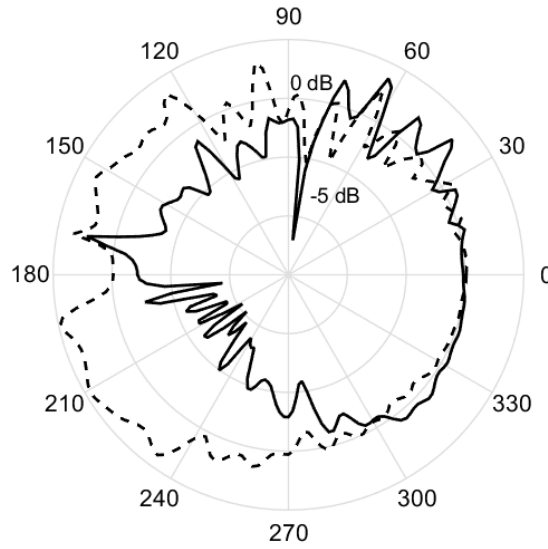
Figure 3.14 : Normalized magnitude of the interior field ($|\mathbf{E}|/|\mathbf{E}^i|$) on the surface of Eaton lens (solid line), and Luneburg lens (dashed line), induced by an infinitesimal dipole on the surface along the positive z-axis.

3.2.3.4 The case with an internal source

The applicability of the method for the cases in which the dipole is located inside the sphere will be considered in this section. Straightforward adaptation by changing the radial functions of the coefficients of the incident field given in (3.46)-(3.48) does not work, since the incident field has a singularity at the location of the dipole. Therefore, the series for the electric field inside the sphere does not converge in a vicinity of the dipole. It is clear that a mathematically rigorous solution cannot be formed based on the analysis presented in this thesis. However, numerical simulations demonstrate that the method still produces useful results, by simply jumping over the singularity caused by the internal source. To this end, an appropriate radial meshing must be constructed in a way that places the source point in a boundary between two adjacent cells. This placement guarantees that the incident field evaluated in the cell centers, albeit large, will be finite. Since the series does not converge aroung the dipole, the value of N_{max} greatly effects the results. The numerical example will demonstrate that point.

For the simulation, consider the two-layered sphere defined in (3.80). The sphere is assumed to have a radius of $a = 1m$. The x-oriented infinitesimal dipole is located at the point $x = 0$, $y = 0$, $z = 0.3m$. Therefore, the radial dependency of the coefficients

for the incoming field given in (3.46)-(3.49) must be altered for $r > 0.3m$. For example, for the coefficients $\alpha_{nm}^i(r)$, the radial function $h_n^{(1)}(k_0 z_d) j_n(k_0 r)$ must be replaced by $h_n^{(1)}(k_0 r) j_n(k_0 z_d)$, for $r > z_d$. The reaason for this alteration can be seen by analysing (3.40)-(3.42). The integrals are discretized by 30 points, to satisfy the requirement about the meshing stated above. For the comparison, the dyadic Green's function for a two-layered sphere with a source located in the inner layer will be used. The formulation of this function can be found in [45]. The total field along the radial direction has been calculated using different values of N_{max} for both methods to show the effect of the internal source on the convergence rate. The results presented in Fig. 3.15 demonstrate that there is an agreement between two methods outside the vicinity of the dipole. Also, different values of N_{max} do not cause any variation in this region, showing that the series converge at these points. On the other hand, in the vicinity of the dipole the series fails to converge even for very large truncation numbers. It can be concluded that the method provides useful results outside the vicinity of the dipole, however, a more rigorous formulation must be developed for the case with an internal source.
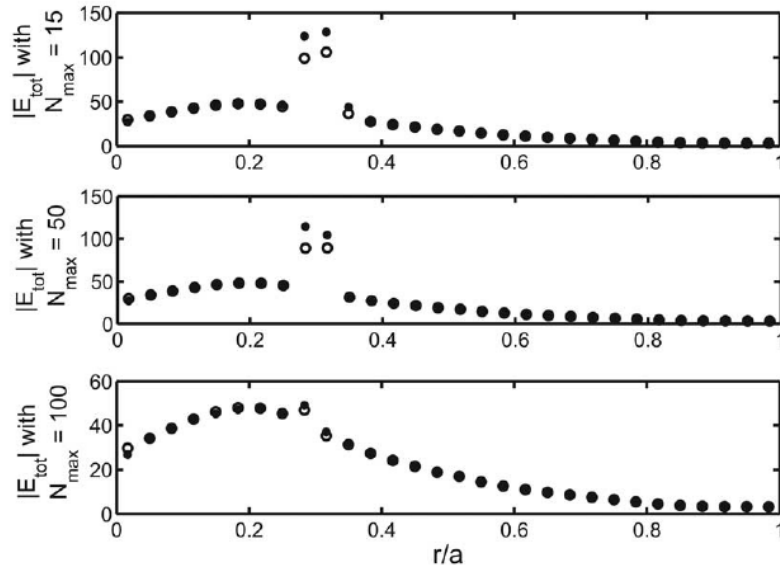
Figure 3.15 : Magnitude of the total field inside a two-layered sphere with an internal source located at $r = 0.3m$, dots corresponds to the solution with integral equations, and circles to the dyadic Green's function.

3.3 Inverse Scattering Problem

In this section, the solution of the 1-D electromagnetic profile inversion problem in spherical coordinates will be developed. Similar to the acoustic case, the aim of this section is to develop a method to reconstruct the unknown profile, which is assumed to be a function of the radial distance only. The reconstruction process will use the scattered field measured on a spherical surface outside the sphere as the data. The 1-D reduced integral equations that were formulated in the previous section for the solution of the direct scattering problem will be reused here as reduced object and data equations. Therefore, the original 3-D problem will be reduced to 1-D form as in a manner similar to the direct scattering problem. It is clear that the electromagnetic inverse problem has a similar structure to the acoustic one. As a result of this similarity, the solution will be modeled after the formulation developed in the section 2.3.2. The iterative Newton's method will be used to reconstruct the electromagnetic parameters, and the Tikhonov regularization will be used to obtain a stable solution. Therefore, the theoretical background presented in the section 2.3.1 is also relevant for the problem analysed in this section, and it will not be repeated here. In the first part of this section, we will formulate the inverse problem, and its iterative solution via the Newton's method. In the second part, some numerical simulations will be presented to demonstrate the validity of the formulation. The content of this section is also available in [69], in a more compact form. A time dependence of $e^{-i\omega t}$ is assumed and omitted throughout the entire section.

3.3.1 The formulation and the solution of the inverse scattering problem

Consider the dielectric sphere of radius a, denoted by D in Fig. 3.16. The permittivity $\varepsilon(r)$, and the conductivity $\sigma(r)$ of the sphere are assumed to be arbitrary functions of radial distance only. These parameters also constitute the unknowns of the inverse scattering problem. On the other hand, the magnetic permeability μ_0 is considered constant throughout the whole space. The region outside the sphere is assumed to be free space region characterized by a constant wave number $k_0 = \omega\sqrt{\varepsilon_0\mu_0}$. The sphere is illuminated by an infinitesimal horizontal electric dipole located at the point $x=0$, $y=0$, $z=z_d$, $z_d > a$. The current moment of the dipole is denoted by C_0.
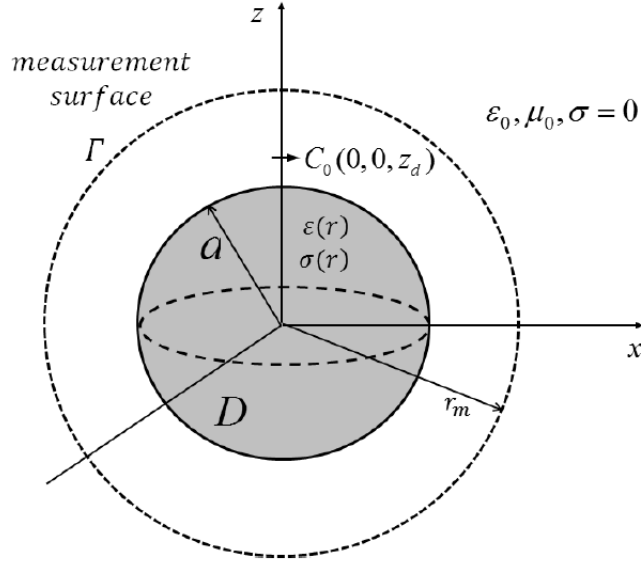
Figure 3.16 : The geometry of the electromagnetic inverse scattering problem.

In Fig. 3.16, Γ represents a spherical surface of radius r_m, where the scattered field is assumed to be measured. Therefore, the aim of the inverse problem is to determine the electromagnetic parameters of the spherical scatterer via the measurement of the scattered field on the surface Γ. To this end, the reduced object equations (3.74)-(3.76), and the reduced data equations (3.78)-(3.79) will be used to formulate a 1-D inversion algorithm. Note that, the unknown parameters determine the object function $v(r)$ appearing in those equations, and the main objective of the iterative process will be to reconstruct $v(r)$, which is defined in (3.37), starting from an initial guess.

It is clear that the coefficients of the scattered field, A_{nm} and B_{nm}, constitute the data of the inverse problem. However, those coefficients cannot be measured directly, and they should be obtained from the measured scattered field. To this end, the orthogonality of the vector spherical harmonics over the unit spherical surface can be used. Since the scattered field is assumed to be measured over a spherical surface with radius r_m, by multiplying the scattered field with the complex conjugate $\mathbf{A}^*_{1nm}(\theta,\phi)$, and integrating over Γ, one obtain the integral

$$\int_0^{2\pi} \int_0^{\pi} \mathbf{E}^s(\mathbf{r}) \cdot \mathbf{A}^*_{1nm}(\theta,\phi) r_m^2 \sin\theta \, d\theta \, d\phi. \tag{3.88}$$

By using (3.27) to represent $\mathbf{E}^s(\mathbf{r})$, and taking the orthogonality relation into account, the integral is transformed into

$$\int_0^{2\pi}\int_0^{\pi} \mathbf{E}^s(\mathbf{r}) \cdot \mathbf{A}_{1nm}^*(\theta,\phi) r_m^2 \sin\theta d\theta d\phi = A_{nm}\sqrt{n(n+1)} h_n^{(1)}(k_0 r_m) r_m^2$$
$$\times \int_0^{2\pi}\int_0^{\pi} \mathbf{A}_{1nm}(\theta,\phi) \cdot \mathbf{A}_{1nm}^*(\theta,\phi) \sin\theta d\theta d\phi.$$

(3.89)

Since the integral on the right hand side is a direct application of the orthogonality relation, the coefficients A_{nm} are obtained as

$$A_{nm} = \frac{1}{\sqrt{n(n+1)} h_n^{(1)}(k_0 r_m)} \int_0^{2\pi}\int_0^{\pi} \mathbf{E}^s(\mathbf{r}) \cdot \mathbf{A}_{1nm}^*(\theta,\phi) \sin\theta d\theta d\phi$$

(3.90)

For the coefficients B_{nm}, the same procedure can be applied using $\mathbf{A}_{2nm}^*(\theta,\phi)$ or $\mathbf{A}_{3nm}^*(\theta,\phi)$. Using $\mathbf{A}_{2nm}^*(\theta,\phi)$ yields

$$B_{nm} = \frac{k_0 r_m}{\sqrt{n(n+1)} \dfrac{\partial}{\partial r}\left[r h_n^{(1)}(k_0 r)\right]\Big|_{r=r_m}} \int_0^{2\pi}\int_0^{\pi} \mathbf{E}^s(\mathbf{r}) \cdot \mathbf{A}_{2nm}^*(\theta,\phi) \sin\theta d\theta d\phi$$

(3.91)

and by $\mathbf{A}_{3nm}^*(\theta,\phi)$, one obtains

$$B_{nm} = \frac{k_0 r_m}{n(n+1) h_n^{(1)}(k_0 r_m)} \int_0^{2\pi}\int_0^{\pi} \mathbf{E}^s(\mathbf{r}) \cdot \mathbf{A}_{3nm}^*(\theta,\phi) \sin\theta d\theta d\phi$$

(3.92)

In practical applications, the scattered field is measured at a finite number of discrete points. Therefore, the integrals in (3.90)-(3.92) should be evaluated numerically. In the numerical simulations that will be presented in the next section, the Simpson's rule have been used for this purpose. Also it should be noted that, in the simulations, the values of B_{nm} obtained via (3.91) and (3.92) have been slightly different due to the errors in numerical integration, and the additive noise in the measured data. Therefore, the arithmetic average of two values has been used.

3.3.1.1 Newton based iterative solution

The formulation of the iterative process follows the same steps that were used in section 2.3.3.2 for the acoustic problem. However, unlike acoustic problem, in the electromagnetic case there are two data equations. Moreover, these equations, namely (3.78) and (3.79), are independent. Therefore, the object function $v(r)$ can be reconstructed independently via the system formed by (3.74)-(3.78), or the the one formed by (3.75)-(3.76), (3.79). Hence, in the iterative process, two different update amounts are obtained for the object function $v(r)$ in each step. Expectedly, the system formed by (3.75)-(3.76), (3.79) is more effective, since it also carries the information obtained from the radial component through the functions $\mathbf{A}_{3nm}(\theta,\phi)$ and the coefficients $\gamma_{nm}(r)$. However, numerical simulations suggest that using the average of the two independent update amounts improves the accuracy of the reconstruction in most cases. Therefore, unless stated otherwise, in the numerical examples that will be presented in the next section, the average value will be used to update the object function at the end of each step.

Now, to formulate the iterative scheme, let us state the data equations (3.78) and (3.79) in a compact form:

$$F_\alpha v = A_{nm} \tag{3.93}$$

$$F_{\beta\gamma} v = B_{nm} \tag{3.94}$$

Here, the operators F_α and $F_{\beta\gamma}$ are defined as

$$F_\alpha v = \frac{ik_0^3}{\sqrt{n(n+1)}} \int_0^a j_n(k_0 r') v(r') \alpha_{nm}(r') r'^2 dr' \tag{3.95}$$

and

$$
\begin{aligned}
F_{\beta\gamma} v = \int_0^a \Bigg\{ & \beta_{nm}(r') \frac{ik_0^2}{\sqrt{n(n+1)}} \frac{\partial}{\partial r'} \left[r' j_n(k_0 r') \right] \\
& + ik_0^2 j_n(k_0 r') \gamma_{nm}(r') \Bigg\} v(r') r' dr'
\end{aligned}
\tag{3.96}
$$

It is clear that, in order to solve (3.93) and (3.94), the values of the coefficients of the interior electric field, $\alpha_{nm}(r)$, $\beta_{nm}(r)$, $\gamma_{nm}(r)$ must be obtained. Therefore, to produce the initial values of those coefficients, denoted by $\alpha_{nm}^{(0)}(r)$, $\beta_{nm}^{(0)}(r)$, $\gamma_{nm}^{(0)}(r)$, the direct scattering problem must be solved by substituting the initial guess for the object function, denoted by $v^{(0)}(r)$, into the reduced object equations (3.74)-(3.76). The solution of the direct scattering problem is explained in the previous section in detail.

After obtaining the coefficients of the interior electric field, the non-linear data equations are linearized:

$$F_\alpha v + F_\alpha' \delta v_\alpha = A_{nm} \tag{3.97}$$

$$F_{\beta\gamma} v + F_{\beta\gamma}' \delta v_{\beta\gamma} = B_{nm} \tag{3.98}$$

Here, δv_α and $\delta v_{\beta\gamma}$ represent the independent update amounts for the object function. These functions will be obtained by inverting the linearized equations (3.97) and (3.98). F_α' and $F_{\beta\gamma}'$ denotes the Fréchet derivatives of the related operators. The open form of these terms are given as

$$F_\alpha' \delta v_\alpha = \frac{ik_0^3}{\sqrt{n(n+1)}} \int_0^a j_n(k_0 r') \delta v_\alpha(r') \alpha_{nm}^{(0)}(r') r'^2 dr' \tag{3.99}$$

and

$$F_{\beta\gamma}' \delta v_{\beta\gamma} = \int_0^a \left\{ \beta_{nm}^{(0)}(r') \frac{ik_0^2}{\sqrt{n(n+1)}} \frac{\partial}{\partial r'} \left[r' j_n(k_0 r') \right] \right. \\ \left. + ik_0^2 j_n(k_0 r') \gamma_{nm}^{(0)}(r') \right\} \delta v_{\beta\gamma}(r') r' dr' \tag{3.100}$$

Note that, as a result of discretization of the integrals in the object and data equations, all the terms appearing in (3.97)-(3.98) are matrices. Therefore, the solution would be obtained by inverting the matrices formed by F_α' and $F_{\beta\gamma}'$, to determine δv_α and $\delta v_{\beta\gamma}$ However, as explained in the section 2.3.1, the Fréchet derivatives are linear compact operators, and hence, the equations (3.97)-(3.98) are ill-posed. To produce a stable

solution, a regularization technique must be used. Similar to the acoustic case, the Tikhonov regularization will be used here to obtain the update amount as

$$\delta v_\alpha^{(1)} = (\alpha_T I + F_\alpha'^* F_\alpha')^{-1} F_\alpha'^* (A_{nm} - F_\alpha v^{(0)}) \tag{3.101}$$

$$\delta v_{\beta\gamma}^{(1)} = (\alpha_T I + F_{\beta\gamma}'^* F_{\beta\gamma}')^{-1} F_{\beta\gamma}'^* (B_{nm} - F_{\beta\gamma} v^{(0)}) \tag{3.102}$$

Here, α_T is the regularization parameter, and I is the identity matrix of the appropriate dimension.

As an alternative formulation, the update amounts can be expressed in terms of some basis functions $\Phi_p(r)$ as

$$\delta v_\chi(r) = \sum_{p=1}^{P} a_p^\chi \Phi_p(r) \tag{3.103}$$

where χ denotes either α or $\beta\gamma$ [1]. In this case, the linearized equations (3.97)-(3.98) are replaced by

$$\sum_{p=1}^{P} a_p^\alpha \left[F_\alpha' \Phi_p(r) \right] = (A_{nm} - F_\alpha v^{(0)}) \tag{3.104}$$

$$\sum_{p=1}^{P} a_p^{\beta\gamma} \left[F_{\beta\gamma}' \Phi_p(r) \right] = (B_{nm} - F_{\beta\gamma} v^{(0)}) \tag{3.105}$$

and solved via Tikhonov regularization to obtain the scalar coefficients a_p^α and $a_p^{\beta\gamma}$ [1]. Note that, in this formulation, the matrix forms of the F_χ' in (3.101) and (3.102) are replaced by the matrix product $F_\chi' \Phi_p$ for the Tikhonov regularization.

For both alternatives the initial step is completed by updating the object function

$$v^{(1)}(r) = v^{(0)}(r) + \frac{\delta v_\alpha(r) + \delta v_{\beta\gamma}(r)}{2} \tag{3.106}$$

The iterative process is continued until the ℓ^2 norm of the ratio $\delta v(r)/v(r)$ becomes smaller than a predefined threshold ε_S.

3.3.2 Numerical simulations

Some numerical tests have been conducted to assess the performance of the method for the electromagnetic case. The results will be presented in three parts: In the first sub-section, three different profiles, slowly varying, oscillating, and piecewise layered, will be reconstructed using different initial guesses for the object functions. In the second part, the independence of the reduced object functions will be analysed. Two different profiles will be constructed via $\delta v_\alpha(r)$ and $\delta v_{\beta\gamma}(r)$ independently, then the results will be compared with those obtained via (3.106). In the final part, the alternative formulation described in (3.103)-(3.105) will be used to determine update amounts. The results obtained via three different basis functions $\Phi_p(r)$ will be presented in the sub-section. In all sub-sections, the error metric, defined in (2.86), will be given as a measure of the success of the reconstruction.

For all examples, the radius of the dielectric sphere is chosen as $a = 0.1m$. The incident field is created by an infinitesimal horizontal electric dipole with a current moment $C_0 = 0.1$, located at the point $x = 0$, $y = 0$, $z = 0.11m$. The operating frequency is chosen as $f = 600MHz$. The radius of the measurement surface Γ is assumed to be $r_m = 0.12m$. To make the simulations more realistic, a $\%5$ additive noise is added to the scattered field. That is, a random term of $0.05|\mathbf{E}_\chi^s|e^{i2\pi r_n}$ is added to each vectorial component denoted by χ. Here, χ represents one of r, θ, ϕ; and r_n's are uniformly distributed random numbers.

For the parameters of the Newton's method, the regularization parameter is chosen as $\alpha_T = 0.5/itn$, itn being the number of iterations. The reasons for decreasing the value of α_T was discussed in the section 2.3.3.1, and that discussion is also valid for the electromagnetic case. For similar reasons, the optimal value determined in the acoustic case will be reused here as the value of the stopping threshold, that is ε_S is chosen as $\varepsilon_S = 10^{-3}$. For the solution of the direct scattering problem, the integrals in (3.74)-(3.76) and (3.77)-(3.78) are evaluated by a discretization of 30 points. Moreover, unless stated otherwise, the truncation number for the series expansions representing the interior and scattered electric fields is chosen as $N_{max} = 3$.

3.3.2.1 The performance test with different profiles

As a first example, the Luneburg lens defined in (3.86) will be reconstructed. The initial guesses for the object function are chosen as $v^{(0)}(r) = 0.75$, $v^{(0)}(r) = 1$ and $v^{(0)}(r) = 1.25$. The results presented in Fig. 3.17 demonstrate that the method is capable of reconstructing slowly varying profiles accurately, provided that an appropriate initial guess is chosen. Expectedly, the best result is obtained for the initial guess of $v^{(0)}(r) = 1$ in 9 iterative steps. The error for this case is calculated as $e_{\ell^2} = 6.2 \times 10^{-3}$, which indicates excellent agreement between the reconstructed and exact profiles. For the remaining initial values, the iterative process lasted for 11 steps, and the error metric is calculated as $e_{\ell^2} = 0.15$. The increase in the error demonstrates the importance of the initial guess for the performance of the method.
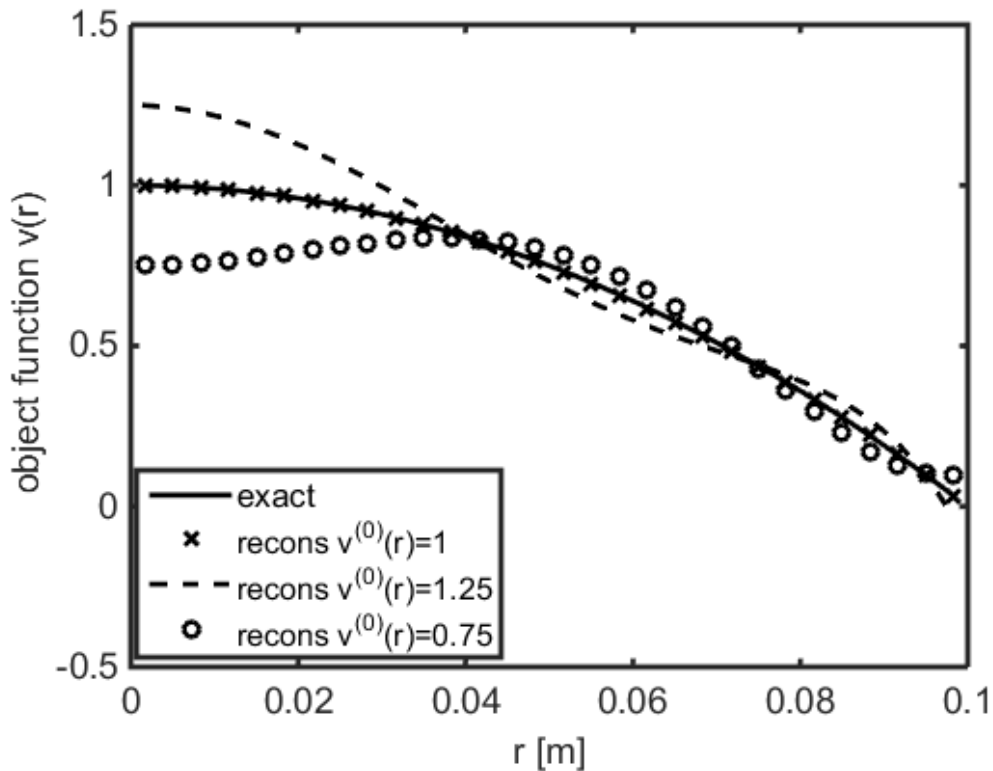
Figure 3.17 : Exact and the reconstructed values of the object function for the Luneburg lens with three different initial guesses for the object function.

Previous example shows that the method is capable of reconstructing slowly varying profiles. It is clear that more more rapidly varying profiles the success rate will be lower. To test this assumption, a profile with sinusoidally varying real, and linearly varying imaginary part will be reconstructed as the second case. The profile is defined as

$$\varepsilon_r(r) = 1.5 + 0.5\cos\left(3\pi\frac{r}{a}\right) + i\left(1 - \frac{r}{a}\right)$$

(3.107)

The initial guesses are chosen as $v^{(0)}(r) = 1.25 + 0.75i$, $v^{(0)}(r) = 1.5 + 1i$ and $v^{(0)}(r) = 1.75 + 1.25i$. The results presented in Fig. 3.18 demonstrate that the method is capable of reconstructing an approximate oscillating profile. However, the difference between the exact and the reconstructed profiles is much greater compared to the case with Luneburg lens. On the other hand, the reconstruction of the imaginary part, depicted in Fig. 3.19, is much more accurate, since it is slowly varying. The itarative process lasted for 14 iterations for each initial guess, and the lowest error value is obtained as $e_{\ell^2} = 0.23$ for the initial guess of $v^{(0)}(r) = 1.5 + 1i$. This example demonstrates that the success of the reconstruction process decreases as the oscillation of the profile increases. For more rapidly oscillating profiles, the method fails to converge to a useful result.

Figure 3.18 : The real part of the exact and the reconstructed values of the object function for the sinusoidally varying profile with three different initial guesses.
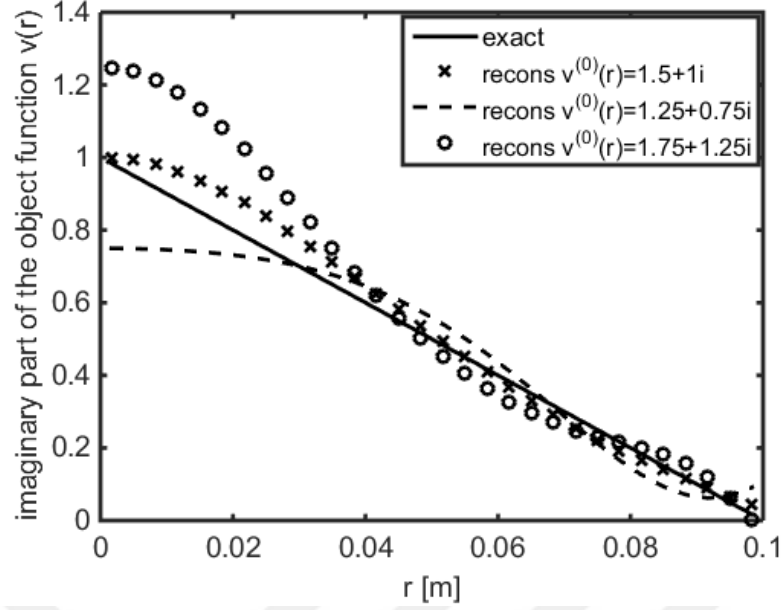
Figure 3.19 : The linearly varying imaginary part of the exact and the reconstructed values of the object function for the sinusoidally varying profile with three different initial guesses.

The reconstruction of piecewise homogeneous layered profiles is more challenging, due to the discontinuities in the layer boundaries. Since the reconstruction is made by continuous radial functions, only an approximation can be obtained for these profiles. As an example of piecewise homogeneous profiles, consider the three layered sphere described by

$$\varepsilon_r(r) = \begin{cases} 3+0.3i & 0 \le r/a \le 0.33 \\ 3.8+0.9i & 0.33 < r/a \le 0.66 \\ 2.4+0.6i & 0.66 < r/a \le 1 \end{cases} \qquad (3.108)$$

The initial guesses for this profile are chosen as $v^{(0)}(r) = 1.75 + 0.2i$, $v^{(0)}(r) = 2 + 0.3i$ and $v^{(0)}(r) = 2.25 + 0.4i$. For these initial values, the iterative process converged in 16 15 and 14 iterations respectively. The results for the real part given in Fig. 3.20, and those for the imaginary part given in Fig. 3.21 shows that although the method expectedly fails to detect sharp transitions, it nevertheless provides a smoothed approximation. The error levels for three initial guesses are calculated as $e_{\ell^2} = 0.13$, $e_{\ell^2} = 0.14$ and $e_{\ell^2} = 0.17$ respectively. The close values indicate that choosing the most suitable initial guess does not guarantee a rapid convergence in the case of

layered profiles. However, it should be noted that the method fails to converge when the initial guess deviates too far from the ideal value. For all types of profiles, the choice of initial parameters determines the success of the method.

Figure 3.20 : The real part of the exact and the reconstructed values of the object function for the three layered profile with three different initial guesses.

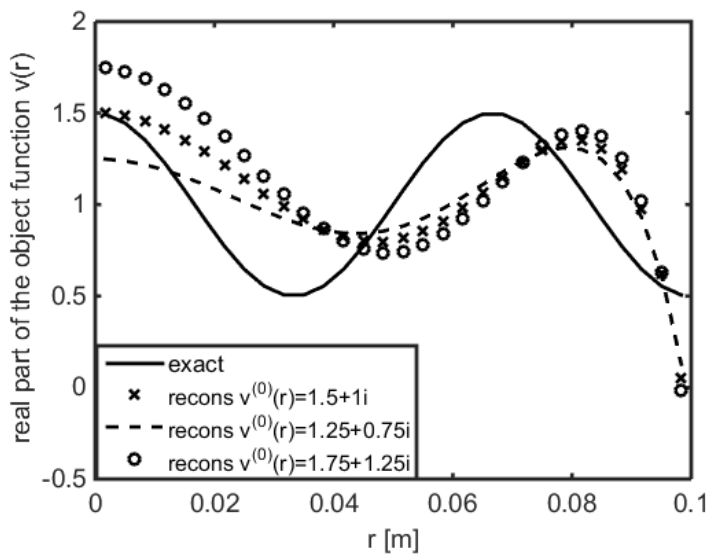**Figure 3.21 :** The imaginary part of the exact and the reconstructed values of the object function for the three layered profile with three different initial guesses.

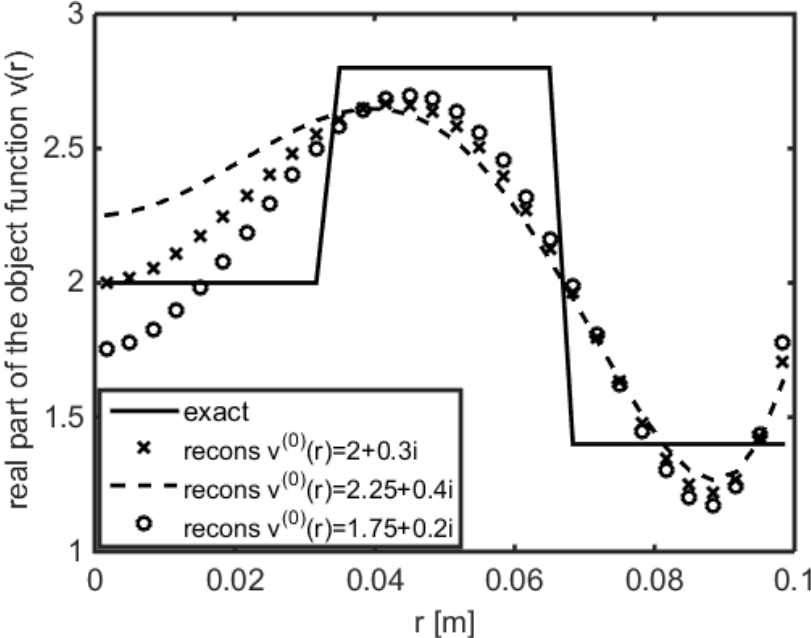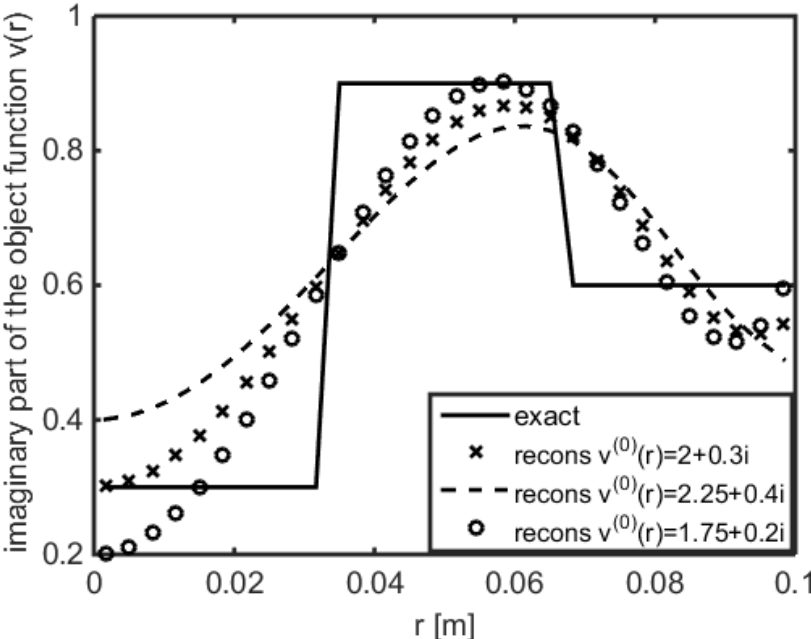### 3.3.2.2 Reconstruction via independent data equations

For all the examples analysed in the previous sub-section, the average value defined in (3.106) has been used. However, as indicated in the section 3.3.1.1, the reduced data equations (3.78) and (3.79) are independent, and the object function can also be reconstructed by using only one of them. That is, the update functions δv_α and $\delta v_{\beta\gamma}$ can be obtained by using the scattered field coefficients A_{nm} and B_{nm} respectively. Then, the update of the object function in the end of each iterative step will be made using either δv_α or $\delta v_{\beta\gamma}$ independently. Here, we will present two examples to compare this approach with the one used in the previous sub-section.

As the first example, the Maxwell fish-eye lens defined in (3.87) will be used for the comparison. For this case, the profile is reconstructed using three different update amounts, namely δv_α, $\delta v_{\beta\gamma}$, and the average of both. For all recontructions, the initial guess is chosen as $v^{(0)}(r) = 3$. As seen in Fig. 3.22, the reconstruction with δv_α, which is lasted 6 iterations, provides only a rough approximation of the actual profile. The reason is that, as stated in the section 3.3.1.1, the system formed by (3.74)-(3.78) does not carry the information provided by the radial component. On the other hand, the reconstruction using $\delta v_{\beta\gamma}$, that is by the system of (3.75)-(3.76), (3.79), provides a much better approximation. This result demonstrates that the reconstruction process using the average value defined in (3.106) is dominated by the system (3.75)-(3.76), (3.79). Nevertheless, using the average value provides the best result of the reconstruction. The error for the average value is calculated as $e_{\ell^2} = 0.01$, whereas for the update via $\delta v_{\beta\gamma}$, it is determined as $e_{\ell^2} = 0.03$. It can be concluded that the additional information provided by the update amount δv_α slightly increases the success of the method.

It should be noted that although this improvement is meaningful in the case of slow variation, it is relatively insignificant for the rapidly oscillating profiles. Consider the sinusoidally varying profile defined in (3.107). In Fig. 3.23 and 3.24, the real and the imaginary parts of the reconstructed profiles are presented. It is clear that the update via the average value and via $\delta v_{\beta\gamma}$ produced similar results. The error rates are given

as $e_{\ell^2} = 0.27$ for the average value, and $e_{\ell^2} = 0.26$ for the update amount $\delta v_{\beta\gamma}$. Moreover, the iterative process for $\delta v_{\beta\gamma}$ lasted only 8 steps, whereas for the average value, the result is obtained in 14 iterations. It can be concluded that for more challenging profiles, reconstruction via the system of system (3.75)-(3.76), (3.79) might be a more efficient alternative.
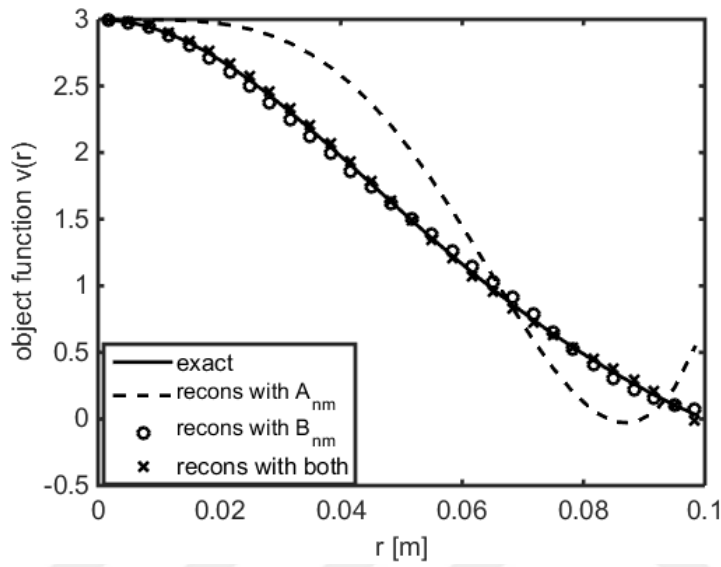
Figure 3.22 : Exact and the reconstructed values of the object function for the Maxwell fish-eye lens obtained via three different update amounts.
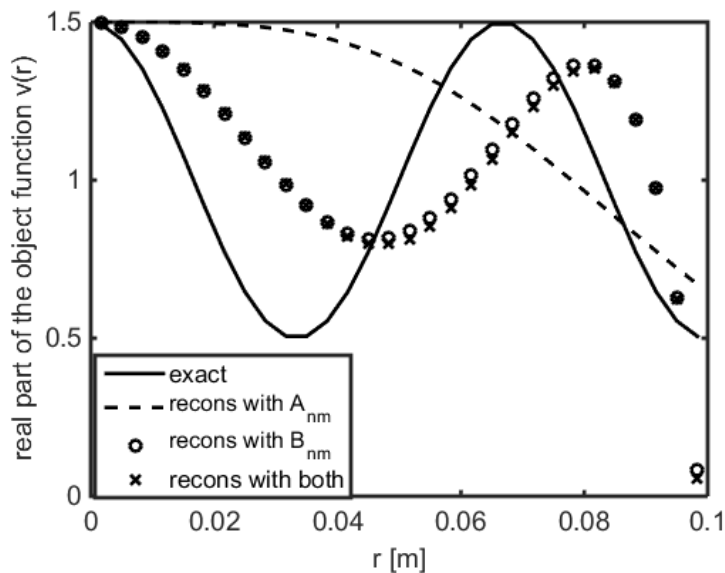
Figure 3.23 : The real part of the exact and the reconstructed values of the object function for the sinusoidally varying profile with three different update amounts.
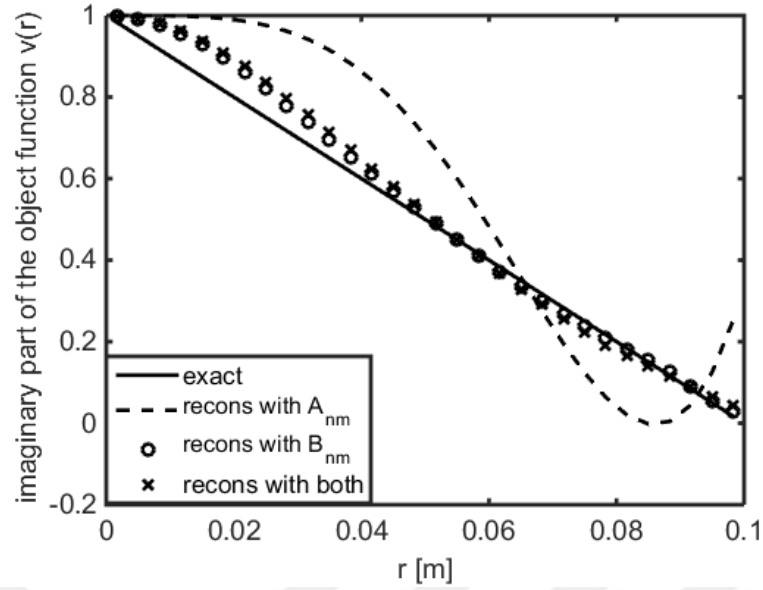
Figure 3.24 : The imaginary part of the exact and the reconstructed values of the object function for the linearly varying profile with three different update amounts.

3.3.2.3 Series expansion for the update amounts

In this sub-section, the alternative formulation using series expansion to represent the update amounts, outlined in (3.103)-(3.105), will be analysed. As explained in the section 3.3.1.1, the update amounts can be expressed in terms of some basis functions, and the linearized data equations can be solved to determine the coefficients of the series expansions. Note that two different series, although with the same basis functions, will be used to represent δv_α and $\delta v_{\beta\gamma}$ separately, and the final update will be done using the average value of δv_α and $\delta v_{\beta\gamma}$ as indicated in (3.106).Three different basis functions will be used for the analysis: the harmonic functions defined as

$$\Phi_p(r) = e^{-i2\pi p \frac{r}{a}}, \qquad p = 0, \pm 1, \pm 2... \tag{3.109}$$

the Bessel functions

$$\Phi_p(r) = j_p\left(k_0 \frac{r}{a}\right), \qquad p = 0, 1, 2... \tag{3.110}$$

and the Dini series

$$\Phi_p(r) = j_n\left(\lambda_p \frac{r}{a}\right), \qquad p = 0, 1, 2... \tag{3.111}$$

In (3.11), λ_p represents the p-th root of the equation

$$x\, j_n'(x) + t_n\, j_n(x) = 0 \tag{3.112}$$

where t_n being any real number. Similar to $N_{\max}$, the truncation number for the series expansion (3.103), denoted as $P_{\max}$, can be considered as an additional parameter. Numerical tests with different profiles suggest that the optimal value for this formulation is $N_{\max} = 5$, instead of $N_{\max} = 3$ which was used in the previous subsections. For the series with harmonic basis functions, the value of $P_{\max}$ is chosen as $P_{\max} = 5$. On the other hand for the Bessel functions and the Dini series, the value of $P_{\max} = 10$ will be used.

As the first example, the sinusoidally varying profile defined in (3.107) will be reconstructed using the basis functions (3.109)-(3.111). The initial guess for the object function is chosen as $v^{(0)}(r) = 1.5 + 1i$. The results presented in Fig. 3.25 and 3.26 demonstrate that the choice of basis functions strongly effects the performance of the method. The reconstruction via Dini series provided a major improvement compared to the previous results that was given in Fig. 3.18 and 3.19. The error metric is decreased from $e_{\ell^2} = 0.23$ to $e_{\ell^2} = 0.12$ by the use of these basis functions. On the other hand, the error is calculated as $e_{\ell^2} = 0.24$ for harmonic functions and $e_{\ell^2} = 0.30$ for the Bessel functions. The results demonstrate that the choice of appropriate basis functions determine the success of this formulation.

However, it should be noted that, for every type of profiles, different basis functions provide the best results. To show this, the three layered sphere, defined in (3.108), will be reconstructed using the same basis functions as the previous example. The initial value for the object function is chosen as $v^{(0)}(r) = 2 + 0.3i$ for this example. As seen in Fig. 3.27 and 3.28, the outcome does not parallel the results obtained for the sinusoidally varying profile. The highest error is obtained for the Dini series as

$e_{\ell^2} = 0.20$. On the other hand, the Bessel functions provided the best outcome with an erro rate of $e_{\ell^2} = 0.12$. Note that this value does not present a significant improvement from the results, obtained in the section 3.3.2.1, with an error of $e_{\ell^2} = 0.14$. The analysis demonstrates the difficulty of predicting the best basis function for specific configurations. The performance of this alternative formulation must be checked seperately for each profile.
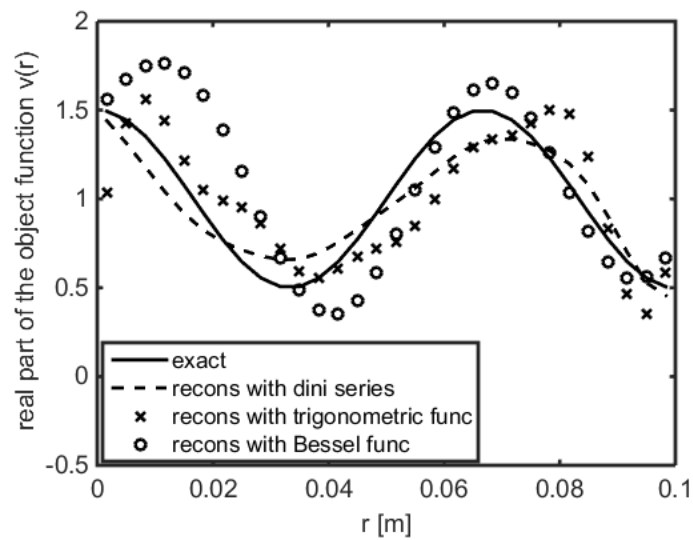
Figure 3.25 : The real part of the exact and the reconstructed values of the object function for the sinusoidally varying profile with three different basis functions.

Figure 3.26 : The imaginary part of the exact and the reconstructed values of the object function for the linearly varying profile with three different basis functions.
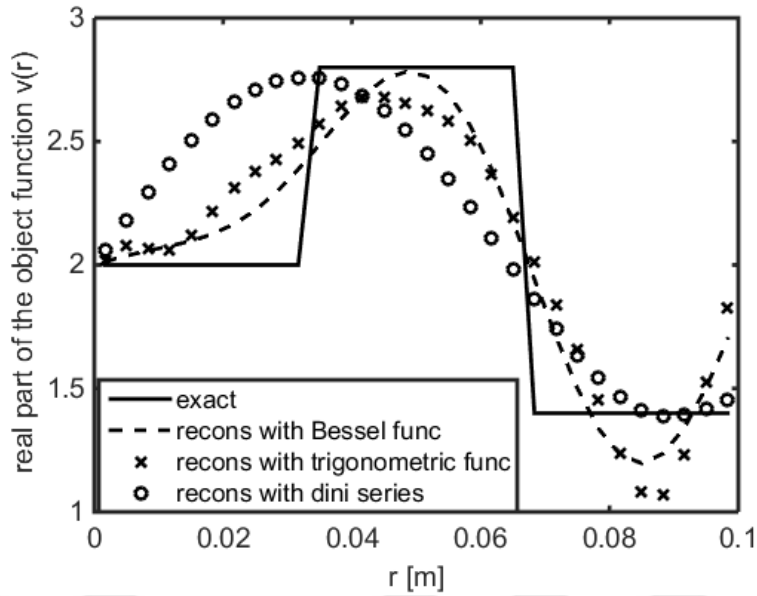
Figure 3.27 : The real part of the exact and the reconstructed values of the object function for the three layered sphere with three different basis functions.

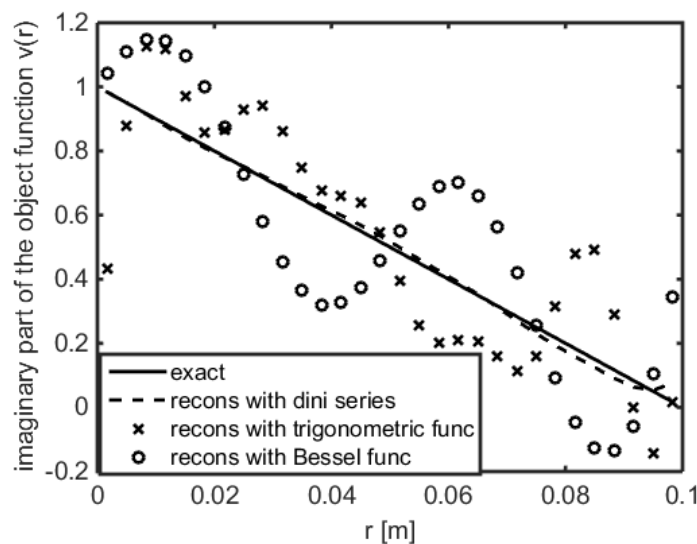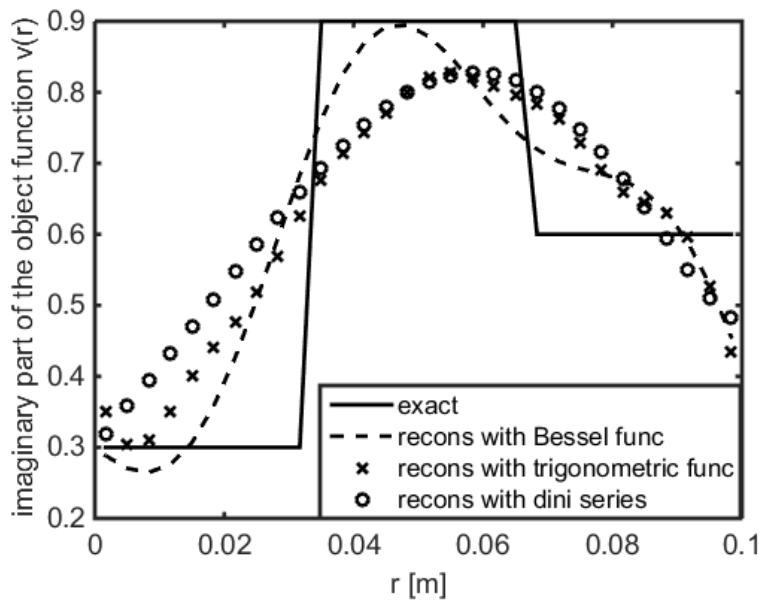**Figure 3.28 :** The imaginary part of the exact and the reconstructed values of the object function for the three layered sphere with three different basis functions.

4. CONCLUSIONS

Direct and inverse scattering problems related to the radially inhomogeneous spheres have been analysed. It has been demonstrated that the original 3-D problems can be transformed into 1-D forms by taking advantage of the spherical symmetry. First, under the assumption of constant density throughout the space, the acoustic problem has been expressed in terms of the scalar object and data equations having 3-D structures. For the acoustic case, the dimension reduction has been achieved by expressing the scalar acoustic field as a series expansion in terms of the scalar spherical harmonics. The angular terms are then eliminated using the orthogonality relation over the unit spherical surface. This approach enables one to formulate 1-D integral equations involving the coefficients of the series expansions only. The direct scattering problem can be solved by a simple discretization of these integrals along the radial direction. On the other hand, for the solution of the inverse problem, a Newton based iterative scheme has been constructed, and tested using various profiles.

The procedure for the electromagnetic problem is similar to the acoustic case. However, since it is a vectorial problem, the formulation of the 1-D equations is much more challenging. Therefore, instead of scalar harmonic functions, the vector spherical harmonics have been used to express the vectorial electric field inside the sphere. It has been proven that by using the orthogonality of these functions with the vector wave functions in the expanded form of the free space dyadic Green's function, it is possible to replace the 3-D electric field equation with a system of 1-D reduced integral equations. Similar to the acoustic case, these equations contain the scalar coefficients of the interior electric field, they can be solved simply by a discretization procedure. It can be concluded that although the mathematical operations, and the functions involved in the procedure are different, the resulting reduced integral equations have similar forms in the acoustic and electromagnetic cases. Therefore, a similar iterative scheme have been used in the solution of the electromagnetic inverse problem.

The numerical simulations for the direct scattering problem demonstrate that the method developed in this thesis is quite reliable for determining the interior and the

scattered field, for both acoustic and electromagnetic cases. The well-posedness and the simple mathematical structures of the reduced integral equations make the implementation of the method easier for different types of problems. Comparisons with alternative analytical techniques show that the method is compatible with the analytical solution and the dyadic Green's function for layered profiles, which proves its accuracy. Moreover, it has been demonstrated that its performance is superior to the alternative numerical techniques such as MoM, in terms of accuracy and required computational effort. Therefore, it can be concluded that, it can be used effectively in the cases involving complex scatterers such as head models, or metamaterial lenses. However, it should be noted here that the constant density assumption puts serious limitations on the use of the method in practical applications. Further research is needed to develop a method to solve the acoustic problem with variable density. On the other hand, no such limitation exists for the electromagnetic case; the method can be employed as it is in the research fields such as biomedical engineering.

For the inverse problem, the numerical simulations in general have produced quite satisfactory results. However, the typical limitations of the Newton based algorithms have been also observed. The performance of the method for layered profiles should be improved before implementing it in practical problems. Moreover, as the contrast between the scatterer and the surrounding medium increases, the linearization process inherent in the Newton method starts to fail, and produces divergent results. Therefore, the method can only be used effectively for profiles having relatively low contrast values. However, it should be noted here that, all the reconstructions in this thesis are performed with a single source and a single operating frequency to demonstrate the basic structure of the method. In practical applications, using multiple sources and frequencies could increase the quality of the reconstruction process. Another drawback of the method is the dependence of the outcome on the initial guess for the unknown profile. In this regard, techniques such as back propagation algorithm can be adapted to the inversion scheme in order to obtain a suitable initial value for the iterative process. In addition, for both acoustic and electromagnetic cases, other inversion techniques, such as contrast source inversion method, might be adapted to the reduced object and data equations obtained in this thesis. These methods could potentially perform better than the Newton based iterative technique, and thus increase the practical value of the inverse problem.

REFERENCES

[1] **Kress, R.**, "Newton's method for inverse obstacle scattering meets the method of least squares," *Inverse Problems*, vol. 19, pp. 91-104, Nov. 2003.

[2] **Colton, D. and Kress, R.**, *Inverse Acoustic and Electromagnetic Scattering Theory*, 3rd ed. New York: Springer Science+Business Media, 2013.

[3] **Tabbara, W**., "Reconstruction of permittivity profiles from a spectral analysis of the reflection coefficient," *IEEE Trans. Antennas Propag.*, vol. 27, no. 2, pp. 241-244, Mar. 1979.

[4] **Tijhuis, A. G.**, "Iterative determination of permittivity and conductivity profiles of a dielectric slab in the time domain," *IEEE Trans. Antennas Propag.*, vol. 29, no. 2, pp. 239-245, Mar. 1981.

[5] **Tijhuis, A. G.**, "Born-type reconstruction of material parameters of an inhomogeneous, lossy dielectric slab from reflected-field data," *Electromagn. Lab./The MIMICAD Res. Center*, Univ. Colorado, Boulder, CO, paper 115, Dec. 1987.

[6] **Roger, A**., "Newton-Kantorovitch algorithm applied to an electromagnetic inverse problem," *IEEE Trans. Antennas Propag.*, vol. 29, no. 2, pp. 232-238, Mar. 1981.

[7] **Hohage, T. and Schormann, C.**, "A Newton-type method for a transmission problem in inverse scattering," *Inverse Problems*, vol. 14, pp. 1207-1227, Apr. 1998.

[8] **Potthast, R.**, "On the convergence of a new Newton-type method in inverse scattering," *Inverse Problems*, vol. 17, pp. 1419-1434, Aug. 2001.

[9] **Kleinman, R. E. and van den Berg, P. M.,** "A modified gradient method for two-dimensional problems in tomography," *J. Comput. Appl. Math.*, vol. 42, pp. 17-35, 1992.

[10] **van den Berg, P. M. and Kleinman, R. E**., "A contrast source inversion method," *Inverse Problems*, vol. 13, pp. 1607-1620, July 1997.

[11] **Harrington, R. F.**, "*Field Computation by Moment Methods*," IEEE Press, New York, 1993.

[12] **Livesay, D. E., and Chen, K. M**., "Electromagnetic fields induced inside arbitrarily shaped biological bodies," *IEEE Trans. on Microwave Theory and Techniques.*, Vol. 22, No. 12, pp. 1273-1280, 1974.

[13] **Umashankar, K., Taflove, A. and Rao, S. M.,** "Electromagnetic scattering by arbitrary shaped three-dimensional homogeneous lossy dielectric objects," *IEEE Trans. Antennas Propag.*, Vol. 34, No. 6, pp. 758-766, 1986.

[14] **Gao, G. and Torres-Verdin, C.**, "Analytical techniques to evaluate the integrals of 3D and 2D spatial dyadic Green's functions," *Progress in Electrmagnetics Research.*, Vol. 52, pp. 47-80, 2005.

[15] **Paulsen, K. D., Lynch, D. R. and Strohbehn, J. W.**, "Three-dimensional finite, boundary, and hybrid element solutions of the Maxwell equations for lossy dielectric media," *IEEE Trans. on Microwave Theory and Techniques.*, Vol. 36, No. 4, pp. 682-693, 1988.

[16] **Yuan, X. C., Lynch, D. R. and Strohbehn, J. W.**, "Coupling of finite element and moment methods for electromagnetic scattering from inhomogeneous objects," *IEEE Trans. Antennas Propag.*, Vol. 38, No. 3, pp. 386-393, 1990.

[17] **Reyhani, S. M. S. and Ludwig, S. A.**, "A comparison of analytical and numerical implanted spherical head model," *Electromagnetics*, vol. 26, pp. 643-660, Feb. 2006.

[18] **Khodabakhshi, H. and Cheldavi, A.**, "Irradiation of a six-layered spherical model of human head in the near field of a half-wave dipole antenna," *IEEE Trans. Microw Theory Tech.*, vol. 58, no. 3, pp. 680-691, Mar. 2010.

[19] **Petrov, Y.,** "Anisotropic spherical head model and its application to imaging electrical activity of the brain," *Phys. Rev. E*, vol. 86, 011917, pp. 1-13, July 2012.

[20] **Ruoss, H. O. and Landstorfer, F. M.,** "Electromagnetic dyadic Green's function for a layered homogeneous lossy dielectric sphere as a head model for numerical emc investigation," *Electronics Letters*, vol. 32, pp. 1935-1937, 1996.

[21] **Okoniewski, M. and Stuchly, M. A.**, "A study of handset antenna and human body interaction," *IEEE Trans. Microw Theory Tech.*, vol. 44, no. 10, pp. 1855-1861, Oct. 1996.

[22] **Liu, F. And Crozier, S.**, "Electromagnetic fields inside a lossy multilayered spherical head phantom excited by MRI coils: models and methods," *Phys. Med. Biol.*, vol. 49, no. 10, pp. 1835-1851, May 2004.

[23] **Li, Y., Rao, L., He, R., Xu, G., Wu, K., Yan, W., Dong G. and Yang, Q**., "A novel combination method of electrical impedance tomography inverse problem for brain imaging," *IEEE Trans. Magn.*, vol. 41, no. 5, pp. 1848-1857, May 2005.

[24] **Karanasiou, I. S., Uzunoglu, N. K. and Papageorgiou, C.,** "Towards functional noninvasive imaging of excitable tissues inside the human body using focused microwave radiometry," *IEEE Trans. Microw Theory Tech.*, vol. 52, no. 8, pp. 1898-1999, Aug. 2004.

[25] **Ellenrieder, N., Muravchik, C. H., Wagner, M. and Nehorai, A.,** "Effect of head shape variations among individuals on the eeg/meg forward and inverse problems," *IEEE Trans. Biomed. Eng.*, vol. 56, no. 3, pp. 587-598, Mar. 2009.

[26] **Scapaticci, R., Di Donato, L., Catapano I. and Crocco, L.**, A feasibility study on microwave imaging for brain stroke monitoring," *Progr. Electromagn.Res B.*, Vol. 40, pp. 305-324, 2012.

[27] **Semenov, S. Y. and Corfield, D. R.**, "Microwave tomography for brain imaging: feasibility assessment for stroke detection," *Intl. J. Antennas Propag.*, Vol. 2008, pp. 1-8, 2008.

[28] **Greenleaf, A., Kurilev, Y., Lassas, M. And Uhlmann, G.**, "Invisibility and inverse problems," *Bull. Amer. Math. Soc.*, vol. 46, no. 1, pp. 55-97, Oct. 2009.

[29] **Geng, Y. L. And He, S.**, "Spherical vector wave functions solution to scattering of a plane wave by a spherical shell of uniaxial anisotropic left-handed material," *Microw. Opt. Techn. Let.*, vol. 50, no. 8, pp. 2142-2146, May 2008.

[30] **Lock, J. A.** "Scattering of an electromagnetic plane wave by a Luneburg lens: III. finely stratified model," *J. Opt. Soc. Am.*, vol. 25, no: 12, pp. 2991-3002, Dec. 2008.

[31] **Kumar P., Altunc, S., Baum, C. E., Buchenauer, C. J. And Schamiloglu, E**., "Radially inhomogeneous spherical dielectric lens for matching 100-ps pulses into biological targets," *IEEE Trans. Plasma Sci.,* vol. 38, pp. 1915-1927, 2010.

[32] **Greenwood, A. D. And Jin, J. M.**, "A field picture of wave propagation in inhomogeneous dielectric lenses," *IEEE Antennas Propagat. Mag.,* vol. 41, pp. 9-18, 1999.

[33] **Martin, P. A.**, "Acoustic scattering by inhomogeneous obstacles," *SIAM J. Appl. Math.,* vol. 64, pp. 297-308, 2003.

[34] **Bleszynski, E., Bleszynski, M. And Jaroszewicz, T**., "Fast volumetric integral-equation solver for acoustic wave propagation through inhomogeneous media," *J. Acoust. Soc. Am.,* vol. 124, pp. 396-408, 2008.

[35] **Kokkorakis, G. C., Fikioris, J. G. And Fikioris, G.**, "Field induced in inhomogeneous spheres by external sources. I. The scalar case," *J. Acoust. Soc. Am.,* vol. 112, pp. 1297-1306, 2002.

[36] **Harrington R.F.**, *Time-harmonic electromagnetic fields,* McGraw-Hill Book Company, 1961.

[37] **Kokkorakis, G. C. And Fikioris, J. G.**, "Acoustic field induced in spheres with inhomogeneous density by external sources," *J. Acoust. Soc. Am.* vol. 115, pp. 478-487, 2004.

[38] **Zouros, G. And Kokkorakis, G. C.,** "Green's function of radial inhomogeneous spheres excited by internal sources," *J. Acoust. Soc. Am.* vol. 129, pp. 24-31, 2011.

[39] **Li Y. L., Liu, C. H., and Franke, S. J.,** "Three-dimensional Green's function for wave propagation in a linearly inhomogeneous medium-the exact analytic solution," *J. Acoust. Soc. Am.* vol. 87, pp. 2285-2291, 1990.

[40] **Raz, S.**, "Direct reconstruction of velocity and density profiles from scattered field data", *Geophysics,* vol. 46, pp. 832-836, 1981.

[41] **Adamyan, V. M. And Fishkov, F. A**., "A one-dimensional inverse problem for a radially inhomogeneous sphere," *Sov. Phys. Acoust.,* vol. 34, pp. 459-463, 1987.

[42] **Williams, E. G., Valdivia, N., Herdic, P. C. And Klos J**., "Volumetric acoustic vector intensity imager," *J. Acoust. Soc. Am.* vol. 120, pp. 1887-1897, 2006.

[43] **van Dongen, K. W. A. And Wright, W. M. D.**, "A full vectorial contrast source inversion scheme for three-dimensional acoustic imaging of both compressibility and density profiles," *J. Acoust. Soc. Am.* vol. 121, pp. 1538-1549, 2007.

[44] **Wu, S. F.**, "Methods for reconstructing acoustic quantities based on acoustic pressure measurements," *J. Acoust. Soc. Am.* vol. 124, pp. 2680-2697, 2008.

[45] **Li, L. W., Kooi, P. S., Leong, M. S., and Yeo, T. S.**, "Electromagnetic dyadic Green's function in spherically multilayered media," *IEEE Trans. Microw Theory Tech.*, vol. 42, no. 12, pp. 2302-2310, Dec. 1994.

[46] **Li, L. W., Kooi, P. S., Leong, M. S., and Yeo, T. S.**, "A general expression of dyadic Green's functions in radially multilayered chiral media," *IEEE Trans. Antennas Propag.*, vol. 43, no. 3, pp. 232-238, Mar. 1995.

[47] **Tan E. L. and Tan, S. Y**., "On the eigenfunction expansions of the dyadic Green's functions for bianisotropic media," *Progr. Electromagn. Res.*, pp. 227-247, 1998, PIER 20.

[48] **Yeh, C.**, "Dyadic Green's function for a radially inhomogeneous spherical medium," *Phys. Rev.*, vol. 131, no. 5, pp. 2350-2353, Sept. 1963.

[49] **Wait, J. R.,** "Electromagnetic scattering from a radially inhomogeneous sphere," *Appl. Sci. Res.*, vol. **10**, pp. 441-450, 1963.

[50] **Kokkorakis, G. C. And Fikioris, J. G.**, "Em field induced in inhomogeneous dielectric spheres by external sources," *IEEE Trans. Antennas Propagat.*, vol. 55, pp. 3178-3190, 2007.

[51] **Stratton, J. A**., *Electromagnetic Theory,* New York: Mcgraw Hill, 1941.

[52] **Tai, C. T.,** *Dyadic Green's Functions in Electromagnetic Theory*. Intext Educational Publishers, 1971.

[53] **Chew, W. C.,** *Wave and Fields in Inhomogeneous Media*. New York: Van Nostrand Reinhold, 1990.

[54] **Kristensson, G.**, (2012, Jan. 20). *Spherical Vector Waves*. [Online]. Available: http://www.eit.lth.se/fileadmin/eit/courses/eit080f/Literature/book.pdf

[55] **Cui T. J. and Liang, C. H.**, "Reconstruction of the permittivity profile of an inhomogeneous medium using an equivalent network method," *IEEE Trans. Antennas Propag.*, vol. 41, no. 12, pp. 1719-1726, Dec. 1993.

[56] **Cui T. J. and Liang, C. H.**, "Novel applications of an approximate profile inversion for one-dimensional medium," *IEEE Trans. Antennas Propag.* vol. 43, no. 3, pp. 308-312, Mar. 1995.

[57] **Omar A. S. and Akhtar, M. J.,** "A generalized technique for the reconstruction of permittivity profiles with a controllable resolution in an arbitrary coordinate system," *IEEE Trans. Antennas Propag.* vol. 53, no. 1, pp. 294-304, Jan. 2005.

[58] **Pierri, R., Brancaccio, A. and De Blasio, F.**, "Multifrequency dielectric profile inversion for a cylindrically stratified medium," *IEEE Trans. Geosci. Remote Sens.*, vol. 38, no. 4, pp. 1716-1724, July 2000.

[59] **Xia, J. J., Habashy, T. M. and Kong, J. A.**, "Profile inversion in a cylindrically stratified lossy medium," *Radio Science*, vol. 29, no. 4, pp. 1131-1141, Aug. 1994.

[60] **Habashy, T. M., Chew, W. C. and Chow, E. Y.**, "Simultaneous reconstruction of permittivity and conductivity profiles in a radially inhomogeneous slab," *Radio Science*, vol. 21, no. 4, pp. 635-645, Aug. 1986.

[61] **Yapar, A.**, "A regularized Newton method for one-dimensional profile inversion of a lossy cylinder," *Int. J. Electron. Commun.*, vol. 60, pp. 590-595, 2006.

[62] **Akhtar M. J. and Omar, A. S.**, "An analytical approach for the inverse scattering solution of radially inhomogeneous spherical bodies using higher order TE and TM illuminations," *IEEE Trans. Geosci. Remote Sens.*, vol. 42, no. 7, pp. 1450-1455, July 2004.

[63] **Tsitsas N. L. And Athanasiadis, C.**, "On spherical wave scattering by an electrically small layered sphere and a related inverse scattering problem," *Int. Conf. on Mathematical Methods in Electromagnetic Theory*, Kharkiv, UA, 2006, pp. 144-146.

[64] **Groetsch C. W.**, *The Theory of Tikhonov Regularization for Fredholm Equations of the First Kind*. White Plains, NY: Longman, 1984.

[65] **Bilgin, E., Yapar A. and Yelkenci, T.**, "An acoustic inverse scattering problem for spheres with radially inhomogeneous compressibility," *J. Acoust. Soc. Am.*, vol. 133, no. 4, pp. 2097-2104, Apr. 2013.

[66] **Hadamard, J.**, *Lectures on Cauchy's Problem in Linear Partial Differential Equations*. Yale University Press, New Haven 1923.

[67] **Bilgin, E. and Yapar A.**, "Electromagnetic scattering by radially inhomogeneous dielectric spheres," *IEEE Trans. Antennas Propag.*, vol. 63, no. 6, pp. 2677-2985, June 2015.

[68] **Richie, J.**, (2011, June 27). *Vector spherical wave functions: library and test codes.* [Online], Technical Report #46.

[69] **Bilgin, E. and Yapar A.**, "A Newton type 1-D profile reconstruction method for radially inhomogeneous dielectric spheres," *Inverse Problems,* (Under Review).

[70] **Ishimaru, A.,** *Electromagnetic Wave Propagation, Radiation and Scattering.* Prentice Hall Inc., Englewood Cliff, New Jersey, 1991.

APPENDICES

APPENDIX A: The discretization procedure for the reduced integral equations of the acoustic case

APPENDIX B: The analytical expression of the acoustic field for two layered piecewise homogeneous sphere

APPENDIX C: Method of moments solution for the scattered acoustic field

APPENDIX D: The dyadic Green's function for a two layered sphere illuminated by an infinitesimal horizontal electric dipole.

APPENDIX E: Method of moments solution for the scattered electromagnetic field

APPENDIX A: The discretization procedure for the reduced integral equations of the acoustic case

As stated in the section 2.2.2.2, one can determine the coefficients of the series expansion for the interior acoustic field by solving the reduced object equation (2.51) via a discretization of the interval $r \in [0, a]$. After obtaining the coefficients of the interior field, the reduced data equation (2.52) can be solved in a similar manner, in order to determine the scattered field coefficients. Here, the details of discretization procedure, and the final discretized forms of the equations will be presented.

Let us assume that the interval $r \in [0, a]$ discretized into P sub-intervals of equal length $\Delta \ell$. For each sub-interval represented by the indice j, $j = 1, 2, .., P$; r_j denotes the center, and d_j, d_{j+1} denote the lower and the upper limits of the sub-interval respectively. Then, the discretized form of (2.51) can be written for any cell center r_j as

$$\hat{u}_{nm}(r_j) - ik_0^3 \sum_{p=1}^{P} \int_{d_p}^{d_{p+1}} j_n(k_0 r_<) h_n^{(1)}(k_0 r_>) v(r') \hat{u}_{nm}(r') r'^2 dr' = \hat{u}_{nm}^i(r_j) \tag{A.1}$$

Here, $r_<$ and $r_>$ stand for the smaller and larger term of the pair r_j, r' respectively. Since for any $p < j$, $r_p < r_j$ and for any $p > j$, $r_p > r_j$; (A.1) can be expressed in a more open form as

$$\hat{u}_{nm}(r_j) - ik_0^3 h_n^{(1)}(k_0 r_j) \sum_{p=1}^{j-1} \int_{d_p}^{d_{p+1}} j_n(k_0 r') v(r') \hat{u}_{nm}(r') r'^2 dr'$$

$$-ik_0^3 j_n(k_0 r_j) \sum_{p=j+1}^{P} \int_{d_p}^{d_{p+1}} h_n^{(1)}(k_0 r') v(r') \hat{u}_{nm}(r') r'^2 dr' \tag{A.2}$$

$$-ik_0^3 \int_{d_j}^{d_{j+1}} j_n(k_0 r_<) h_n^{(1)}(k_0 r_>) v(r') \hat{u}_{nm}(r') r'^2 dr' = \hat{u}_{nm}^i(r_j)$$

The last integral on the left hand side of (A.2) represents the self-contribution of the sub-interval j, and this term should be analysed independently. For all integrals, if the length $\Delta\ell$ of the sub-intervals are small enough, the variation of the spherical Bessel functions, and that of the object function $v(r)$ within the sub-interval can be considered negligible. Under this assumption the integration becomes straightforward, and letting $I_\Delta(\ell_1, \ell_2)$ denotes the operator

$$I_\Delta(\ell_1, \ell_2) = \int_{\ell_1}^{\ell_2} r'^2 dr' = \frac{\ell_2^3 - \ell_1^3}{3} \tag{A.3}$$

(A.2) becomes

$$
\begin{aligned}
&\hat{u}_{nm}(r_j) - ik_0^3 h_n^{(1)}(k_0 r_j) \sum_{p=1}^{j-1} j_n(k_0 r_p) v(r_p) \hat{u}_{nm}(r_p) I_\Delta(d_p, d_{p+1}) \\
&- ik_0^3 j_n(k_0 r_j) \sum_{p=j+1}^{P} h_n^{(1)}(k_0 r_p) v(r_p) \hat{u}_{nm}(r_p) I_\Delta(d_p, d_{p+1}) \\
&- ik_0^3 v(r_j) \hat{u}_{nm}(r_j) \int_{d_j}^{d_{j+1}} j_n(k_0 r_<) h_n^{(1)}(k_0 r_>) r'^2 dr' = \hat{u}_{nm}^i(r_j)
\end{aligned}
\tag{A.4}
$$

The integral in the term representing self-contribution can be evaluated in a similar manner by further discretizing the sub-interval into two halves. In this case, the integral can be aproximated by

$$
\begin{aligned}
&\int_{d_j}^{d_{j+1}} j_n(k_0 r_<) h_n^{(1)}(k_0 r_>) r'^2 dr' \cong h_n^{(1)}(k_0 r_j) \int_{d_j}^{r_j} j_n(k_0 r') r'^2 dr' \\
&+ j_n(k_0 r_j) \int_{r_j}^{d_{j+1}} h_n^{(1)}(k_0 r') r'^2 dr'
\end{aligned}
\tag{A.5}
$$

Once again, under the assumption of negligible variation, the integrals can be removed:

$$\int_{d_j}^{d_{j+1}} j_n(k_0 r_<) h_n^{(1)}(k_0 r_>) r'^2 dr' \cong h_n^{(1)}(k_0 r_j) j_n \left[k_0 \left(r_j - \frac{\Delta \ell}{2} \right) \right] I_\Delta(d_j, r_j)$$

$$+ j_n(k_0 r_j) h_n^{(1)} \left[k_0 \left(r_j + \frac{\Delta \ell}{2} \right) \right] I_\Delta(r_j, d_{j+1})$$

(A.6)

Substituting (A.6) into (A.4) yields the final discretized form of (2.51) as

$$\hat{u}_{nm}(r_j) - i k_0^3 h_n^{(1)}(k_0 r_j) \sum_{p=1}^{j-1} j_n(k_0 r_p) v(r_p) \hat{u}_{nm}(r_p) I_\Delta(d_p, d_{p+1})$$

$$- i k_0^3 j_n(k_0 r_j) \sum_{p=j+1}^{P} h_n^{(1)}(k_0 r_p) v(r_p) \hat{u}_{nm}(r_p) I_\Delta(d_p, d_{p+1})$$

$$- i k_0^3 v(r_j) \hat{u}_{nm}(r_j) \left\{ h_n^{(1)}(k_0 r_j) j_n \left[k_0 \left(r_j - \frac{\Delta \ell}{2} \right) \right] I_\Delta(d_j, r_j) \right.$$

$$\left. + j_n(k_0 r_j) h_n^{(1)} \left[k_0 \left(r_j + \frac{\Delta \ell}{2} \right) \right] I_\Delta(r_j, d_{j+1}) \right\} = \hat{u}_{nm}^i(r_j)$$

(A.7)

(A.7) can easily be converted into a matrix form. The procedure is similar to the MoM application with point matching technique. Considering that the values $\hat{u}_{nm}^i(r_j)$ are known, after forming the $P \times P$ coefficient matrix, one can obtain the values of the coefficients $\hat{u}_{nm}(r_j)$ at the center of each sub-interval by a matrix inversion operation. (The reader should refer to Appendix C for a more detailed demonstration of the technique applied to a similar problem.) The elements of the coefficient matrix K can be stated as

$$K_{jp} = \begin{cases} i k_0^3 h_n^{(1)}(k_0 r_j) j_n(k_0 r_p) v(r_p) I_\Delta(d_p, d_{p+1}) & j > p \\ i k_0^3 j_n(k_0 r_j) h_n^{(1)}(k_0 r_p) v(r_p) I_\Delta(d_p, d_{p+1}) & j < p \end{cases}$$

(A.8)

and

$$K_{jp} = ik_0^3 v(r_j) \left\{ h_n^{(1)}(k_0 r_j) j_n \left[k_0 \left(r_j - \frac{\Delta \ell}{2} \right) \right] I_\Delta(d_j, r_j) \right.$$

$$\left. + j_n(k_0 r_j) h_n^{(1)} \left[k_0 \left(r_j + \frac{\Delta \ell}{2} \right) \right] I_\Delta(r_j, d_{j+1}) \right\} \qquad j = p \tag{A.9}$$

The unknown coefficients $\hat{u}_{nm}(r_j)$ can be determined in a $P \times 1$ matrix form, denoted as $\hat{U}_{nm}$, by the following matrix operation

$$(I - K)^{-1} \hat{U}_{nm}^i = \hat{U}_{nm} \tag{A.10}$$

where $\hat{U}_{nm}^i$ represents the $P \times 1$ matrix form of the coefficients $\hat{u}_{nm}^i(r_j)$, and I denotes the identity matrix.

The discretization procedure for the reduced data equation (2.52) is similar. Since for any $r > a$, $r > r'$; there is no self-contribution, and the resulting discretized form can be obtained as

$$\hat{u}_{nm}^s(r) = ik_0^3 h_n^{(1)}(k_0 r) \sum_{p=1}^{P} j_n(k_0 r_p) v(r_p) \hat{u}_{nm}(r_p) I_\Delta(d_p, d_{p+1}) \tag{A.11}$$

It should be noted that the coefficients $\hat{u}_{nm}(r_p)$ appearing in (A.11) are the coefficients of the interior electric field determined by solving the discretized object equation (A.10). It is clear from (A.11) that no matrix operation is necessary for calculating the coefficients $\hat{u}_{nm}^s(r)$ of the scattered field.

APPENDIX B: The analytical expression of the acoustic field for two layered piecewise homogeneous sphere

Consider the geometry for the two layered sphere presented in Fig. B.1. The acoustic field in each region, described by the wave numbers k_0, k_1 and k_2, can be expressed analytically as series expansions in terms of elementary wave functions. To this end, we first formulate the total field

$$u(r,\theta,\phi) = \begin{cases} u^i(r,\theta,\phi) + u_1(r,\theta,\phi) & r > b \\ u_2(r,\theta,\phi) & a < r > b \\ u_3(r,\theta,\phi) & r < a \end{cases} \tag{B.1}$$

where $u^i(r,\theta,\phi)$ is the incoming field defined in (2.53).

Expectedly, the series expansions for the remaining field terms in (B.1) will be of similar nature:

$$u_1(r,\theta,\phi) = \frac{ik_0 P_0}{4\pi} \sum_{n=0}^{\infty} \sum_{m=-n}^{n} \frac{(2n+1)(n-|m|)!}{(n+|m|)!} a_{nm} h_n^{(1)}(k_0 r) P_n^{|m|}(\cos\theta) e^{im\phi} \tag{B.2}$$

$$u_2(r,\theta,\phi) = \frac{ik_0 P_0}{4\pi} \sum_{n=0}^{\infty} \sum_{m=-n}^{n} \frac{(2n+1)(n-|m|)!}{(n+|m|)!} \left(b_{nm} h_n^{(1)}(k_1 r) + c_{nm} j_n(k_1 r) \right)$$
$$\times P_n^{|m|}(\cos\theta) e^{im\phi} \tag{B.3}$$

$$u_3(r,\theta,\phi) = \frac{ik_0 P_0}{4\pi} \sum_{n=0}^{\infty} \sum_{m=-n}^{n} \frac{(2n+1)(n-|m|)!}{(n+|m|)!} d_{nm} j_n(k_2 r) P_n^{|m|}(\cos\theta) e^{im\phi} \tag{B.4}$$

In these equations, a_{nm}, b_{nm}, c_{nm}, d_{nm} are scalar coefficients that will be determined using the boundary conditions. Note that, the main difference in the series expansions are the radial dependence of the wave functions. The radial dependence of $u_1(r,\theta,\phi)$ must be expressed by Hankel functions of the first kind to satisfy the radiation condition. On the other hand, for $u_3(r,\theta,\phi)$, the Bessel functions must be chosed to avoid singularity at $r = 0$.
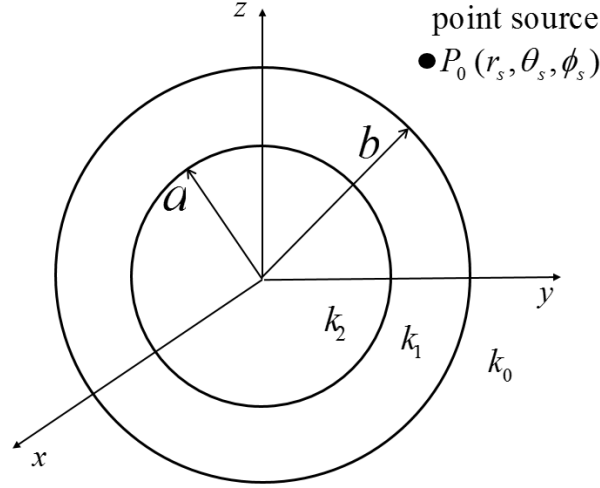
Figure B.1 : The geometry for the two-layered sphere with a point source.

An acoustic field must satisfy two boundary conditions at an interface between two media [70]. First, the pressure, that is the acoustic field u, must be continuous; and secondly, the normal component of the particle velocity, that is $(1/\rho)(\partial u/\partial n)$, must be continuous. Here, ρ is the density of the medium, and $\partial/\partial n$ stands for the normal derivative. For the interfaces $r=a$ and $r=b$, these boundary conditions are stated as

$$u^i(b,\theta,\phi)+u_1(b,\theta,\phi)=u_2(b,\theta,\phi) \tag{B.5}$$

$$u_2(a,\theta,\phi)=u_3(a,\theta,\phi) \tag{B.6}$$

$$\frac{1}{\rho_0}\frac{\partial}{\partial r}\Big[u^i+u_1\Big]\bigg|_{r=b}=\frac{1}{\rho_1}\frac{\partial}{\partial r}\Big[u_2\Big]\bigg|_{r=b} \tag{B.7}$$

$$\frac{1}{\rho_1}\frac{\partial}{\partial r}\Big[u_2\Big]\bigg|_{r=a}=\frac{1}{\rho_2}\frac{\partial}{\partial r}\Big[u_3\Big]\bigg|_{r=a} \tag{B.8}$$

Through these equations, one can form the necessary linear equation system to determine the coefficients a_{nm}, b_{nm}, c_{nm}, d_{nm}. Considering the angular terms are identical for all series expansion of the field values, the equations (B.5)-(B.8) can be written in open form as

$$j_n(k_0b)h_n^{(1)}(k_0r_s)P_n^{|m|}(\cos\theta_s)e^{-im\phi_s}+a_{nm}h_n^{(1)}(k_0b)=b_{nm}h_n^{(1)}(k_1b)+c_{nm}j_n(k_1b) \tag{B.9}$$

$$b_{nm}h_n^{(1)}(k_1 a) + c_{nm}j_n(k_1 a) = d_{nm}j_n(k_2 a) \tag{B.10}$$

$$\frac{1}{\rho_0}\Big[j_n'(k_0 b)h_n^{(1)}(k_0 r_s)P_n^{|m|}(\cos\theta_s)e^{-im\phi_s}$$
$$+a_{nm}h_n^{(1)\prime}(k_0 b)\Big] = \frac{1}{\rho_1}\Big[b_{nm}h_n^{(1)\prime}(k_1 b) + c_{nm}j_n'(k_1 b)\Big] \tag{B.11}$$

$$\frac{1}{\rho_1}\Big[b_{nm}h_n^{(1)\prime}(k_1 a) + c_{nm}j_n'(k_1 a)\Big] = \frac{1}{\rho_2}d_{nm}j_n'(k_2 a) \tag{B.12}$$

It is clear that the coefficients can be obtained via (B.9)-(B.12) by basic algebraic operations. The final forms are

$$b_{nm} = \frac{\alpha_2\beta_3}{\alpha_2\alpha_3 - \alpha_1\alpha_4} \tag{B.13}$$

$$c_{nm} = -\frac{\alpha_1\beta_3}{\alpha_2\alpha_3 - \alpha_1\alpha_4} \tag{B.14}$$

$$a_{nm} = \frac{1}{h_n^{(1)}(k_0 b)}\Big[b_{nm}h_n^{(1)}(k_1 b) + c_{nm}j_n(k_1 b) - \beta_1\Big] \tag{B.15}$$

$$d_{nm} = \frac{1}{j_n(k_2 a)}\Big[b_{nm}h_n^{(1)}(k_1 a) + c_{nm}j_n(k_1 a)\Big] \tag{B.16}$$

where

$$\beta_1 = j_n(k_0 b)h_n^{(1)}(k_0 r_s)P_n^{|m|}(\cos\theta_s)e^{-im\phi_s} \tag{B.17}$$

$$\beta_2 = \frac{1}{\rho_0}\Big[j_n'(k_0 b)h_n^{(1)}(k_0 r_s)P_n^{|m|}(\cos\theta_s)e^{-im\phi_s}\Big] \tag{B.18}$$

$$\beta_3 = -\frac{1}{\rho_0}\beta_1 h_n^{(1)\prime}(k_0 b) + \beta_2 h_n^{(1)}(k_0 b) \tag{B.19}$$

$$\alpha_1 = \frac{1}{\rho_2} j_n'(k_2 a) h_n^{(1)}(k_1 a) - \frac{1}{\rho_1} j_n(k_2 a) h_n^{(1)'}(k_1 a)$$

(B.20)

$$\alpha_2 = \frac{1}{\rho_2} j_n'(k_2 a) j_n(k_1 a) - \frac{1}{\rho_1} j_n(k_2 a) j_n'(k_1 a)$$

(B.21)

$$\alpha_3 = -\frac{1}{\rho_0} h_n^{(1)'}(k_0 b) h_n^{(1)}(k_1 b) + \frac{1}{\rho_1} h_n^{(1)'}(k_1 b) h_n^{(1)}(k_0 b)$$

(B.22)

$$\alpha_4 = -\frac{1}{\rho_0} j_n(k_1 b) h_n^{(1)'}(k_0 b) + \frac{1}{\rho_1} j_n'(k_1 b) h_n^{(1)}(k_0 b)$$

(B.23)

APPENDIX C: Method of moments solution for the scattered acoustic field

The MoM solution for the electromagnetic field scattered by a 3-D inhomogeneous object can be found in [14]. Here, a brief explanation of the solution for the acoustic scattered field, which is a scalar version of the electromagnetic solution, will be presented. For the detailed derivation of the mathematical formulation, the reader should refer to [14].

The method aims to solve the 3-D object equation given in (2.40) by discretizing the scatterer into N cubic cells. If the sizes of the cells are small enough compared to the operating wavelength, the field and the object function $v(r)$ inside each cell can be considered constant. By this assumption, u_m, the field value at the center of the cell denoted by m $(1 < m < N)$, can be determined by

$$u_m = u_m^i + \sum_{n=1}^{N} k_0^2 v(r_n) u_n \int_{\tau_n} g(\mathbf{r},\mathbf{r}')dv' \bigg|_{\mathbf{r}=r_m,\mathbf{r}'=r_n} \tag{C.1}$$

Here, u_m^i is the value of the incoming field at the center of cell m, and the pair $\mathbf{r}_m, \mathbf{r}_n$ denotes the centers of the cells m, n. Also, for the integral of the Green's function in (C.1), the integration region τ_n is the volume of the source cell n. It is clear that, a linear equation system, consisting of N equations with scalar coefficients, can be formed via (B.1), and the field values at the center of each cell can be determined by a matrix inversion operation involving the known values of the incoming field:

$$\left(I - K\right)^{-1} U^i = U \tag{C.2}$$

Here, U^i and U are $N \times 1$ matrices, whose elements are the values of the incoming field and the total field at the cell centers respectively. I is the identity matrix, and K is the $N \times N$ coefficient matrix, whose elements are given by

$$K_{mn} = k_0^2 v(r_n) \int_{\tau_n} g(\mathbf{r},\mathbf{r}')dv' \bigg|_{\mathbf{r}=r_m,\mathbf{r}'=r_n} \tag{C.3}$$

Once the interior field is determined using (C.2), the scattered field at any point $\mathbf{r}_f$ outside the sphere can be easily obtained by evaluating

$$u(\mathbf{r}_f) = \sum_{n=1}^{N} k_0^2 v(r_n) u_n \int_{\tau_n} g(\mathbf{r}, \mathbf{r}') dv' \bigg|_{\mathbf{r}=r_f, \mathbf{r}'=r_n} \tag{C.4}$$

in a similar manner to (C.1). Therefore, the main challenge is to integrate the Green's function over the region τ_n to determine the coefficients K_{mn}. Although the discretization is made using cubic cells in order to better represent the shape of the scatterer, a spherical cell allows one to evaluate the integration analytically. To this end, the integration volume τ_n is assumed to be a sphere with radius a_{eq}. Here, a_{eq} is the radius of the sphere having equivalent volume to the cubic cell with side length a

$$a_{eq} = \left(\frac{3}{4\pi}\right)^{\frac{1}{3}} a \tag{C.5}$$

We will first evaluate the integral for the case of a singular cell, that is $m = n$. This case is called singular because $\mathbf{r}$ and $\mathbf{r}'$ are in the same cell, and the Green's function has a singularity at $\mathbf{r} = \mathbf{r}'$. By using the expression for the Green's function given in (2.44), and considering the mathematical properties of the spherical harmonics the integral can be formulated as

$$\int_{\tau_n} g(\mathbf{r}, \mathbf{r}') dv' = i k_0 j_0(k_0 r) \int_{r}^{a_{eq}} h_0^{(1)}(k_0 r') r'^2 dr'$$
$$+ i k_0 h_0^{(1)}(k_0 r) \int_{0}^{r} j_0(k_0 r') r'^2 dr' \tag{C.6}$$

Using the asymptotic formulas

$$h_0^{(1)}(k_0 r) = -\frac{i}{k_0 r} e^{ik_0 r} \tag{C.7}$$

and

$$j_0\left(k_0 r\right) = \frac{\sin k_0 r}{k_0 r} \tag{C.8}$$

one can obtain the final form of the integral for the singular cell:

$$\int_{\tau_n} g(\mathbf{r},\mathbf{r}')dv' = \frac{1}{k_0^2}\left[\left(1-ik_0 a_{eq}\right)e^{ik_0 a_{eq}} - 1\right] \tag{C.9}$$

For the non-singular cells, that is for the case of $m \neq n$, $\mathbf{r}$ is outside of the integration region, and r is always greater than r'. Therefore, the integration becomes

$$\int_{\tau_n} g(\mathbf{r},\mathbf{r}')dv' = ik_0 h_0^{(1)}(k_0 r)\int_0^r j_0(k_0 r')r'^2 dr' \tag{C.10}$$

Again, considering the asymptotic formulas (C.7)-(C.8), the result of the integration for non-singular cells can be written as

$$\int_{\tau_n} g(\mathbf{r},\mathbf{r}')dv' = \frac{4\pi a_{eq}}{k_0^2}\left[\frac{\sin k_0 a_{eq}}{k_0 a_{eq}} - \cos k_0 a_{eq}\right]\frac{e^{ik_0|\mathbf{r}_m-\mathbf{r}_n|}}{4\pi|\mathbf{r}_m-\mathbf{r}_n|} \tag{C.11}$$

where $|\mathbf{r}_m - \mathbf{r}_n|$ is the Euclidean distance between the centers of the cells m, n. Thus, the elements of the coefficient matrix K has been determined:

$$K_{mn} = \begin{cases} v(r_n)\left[\left(1-ik_0 a_{eq}\right)e^{ik_0 a_{eq}} - 1\right] & m = n \\ a_{eq}v(r_n)\left[\dfrac{\sin k_0 a_{eq}}{k_0 a_{eq}} - \cos k_0 a_{eq}\right]\dfrac{e^{ik_0|\mathbf{r}_m-\mathbf{r}_n|}}{|\mathbf{r}_m-\mathbf{r}_n|} & m \neq n \end{cases} \tag{C.12}$$

Note that, for scattering field, measurement point $\mathbf{r}_f$ is always outside the sphere. Therefore, the integral in (C.4) should be evaluated according to the formulation obtained for non-singular cells in (C.11). Thus, the open form of (C.4) can be expressed as

$$u(\mathbf{r}_f) = \sum_{n=1}^{N} v(r_n) a_{eq} u_n \left[\frac{\sin k_0 a_{eq}}{k_0 a_{eq}} - \cos k_0 a_{eq} \right] \frac{e^{ik_0 |\mathbf{r}_f - \mathbf{r}_n|}}{|\mathbf{r}_f - \mathbf{r}_n|} \tag{C.13}$$

where u_n is the total field at the center of the cell denoted by n, which is obtained by solving (C.2). Similar to (C.11), $|\mathbf{r}_f - \mathbf{r}_n|$ denotes the Euclidean distance between the measurement point and the center of the cell n.

APPENDIX D: The dyadic Green's function for a two layered sphere illuminated by an infinitesimal horizontal electric dipole

Consider the geometry for the two layered sphere presented in Fig. D.1. The entire space consists of three piecewise homogeneous regions, which are characterized by the wave numbers k_1, k_2 and k_3. The dyadic Green's function can be constructed in each layer using the even and odd vector wave functions defined in (3.29)-(3.30). The details of the derivation procedure can be found in [52]. Here, a brief outline of the formulation and the resulting functions will be presented. Let us first define the dyadic Green's functions for each layer as

$$\bar{\bar{\mathbf{G}}}_3^{(11)}(\mathbf{r},\mathbf{r}') = \bar{\bar{\mathbf{G}}}_0^{eo}(\mathbf{r},\mathbf{r}') + \bar{\bar{\mathbf{G}}}_{3s}^{(11)}(\mathbf{r},\mathbf{r}') \qquad r \geq a \tag{D.1}$$

$$\bar{\bar{\mathbf{G}}}_3^{(21)}(\mathbf{r},\mathbf{r}') = \bar{\bar{\mathbf{G}}}_{3s}^{(21)}(\mathbf{r},\mathbf{r}') + \bar{\bar{\mathbf{G}}}_{3s}^{(22)}(\mathbf{r},\mathbf{r}') \qquad a \geq r \geq b \tag{D.2}$$

$$\bar{\bar{\mathbf{G}}}_3^{(31)}(\mathbf{r},\mathbf{r}') = \bar{\bar{\mathbf{G}}}_{3s}^{(31)}(\mathbf{r},\mathbf{r}') \qquad r \leq b \tag{D.3}$$
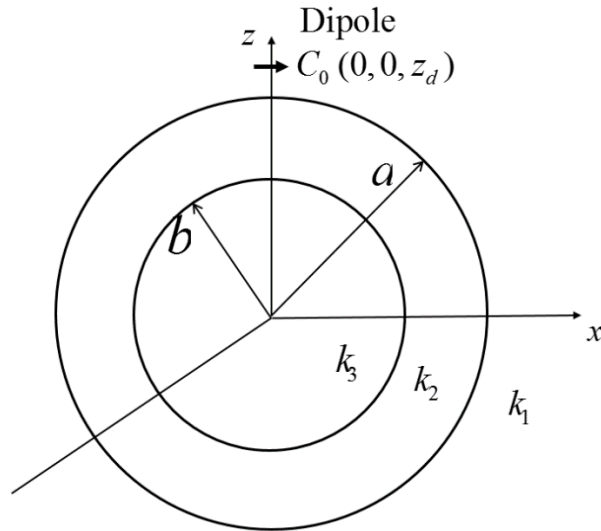
Figure D.1 : The geometry for the two-layered sphere with an x-oriented dipole situated along the z-axis.

The function $\bar{\bar{\mathbf{G}}}_0^{eo}(\mathbf{r},\mathbf{r}')$ in (D.1) represents the free space dyadic Green's function that was defined in (3.31) in terms of the even and odd vector wave functions. Note that the definitions of the dyadic Green's functions, given in (D.1)-(D.3), indicates that the source is located in the region outside the sphere, since the term $\bar{\bar{\mathbf{G}}}_0^{eo}(\mathbf{r},\mathbf{r}')$ is included

in the expression of $\bar{\bar{\mathbf{G}}}_3^{(11)}(\mathbf{r},\mathbf{r}')$, i.e. the function that represents the field in the region $r \geq a$. $\bar{\bar{\mathbf{G}}}_0^{eo}(\mathbf{r},\mathbf{r}')$ represents the field created by the source in the case of homogeneous space, and it is only term that has a singularity. The open expressions of the remaining functions in (D.1)-(D.3) can also be formulated in terms of the even and odd vector wave functions:

$$
\begin{aligned}
\bar{\bar{\mathbf{G}}}_{3s}^{(11)}(\mathbf{r},\mathbf{r}') = {} & \frac{ik_1}{4\pi}\sum_{n=1}^{\infty}\sum_{m=0}^{n}(2-\delta_0)\frac{2n+1}{n(n+1)}\frac{(n-m)!}{(n+m)!} \\
& \times \left[A_n \mathbf{M}_{\substack{e\\o}nm}^{(1)}(k_1\mathbf{r})\mathbf{M}_{\substack{e\\o}nm}^{(1)}(k_1\mathbf{r}') + B_n \mathbf{N}_{\substack{e\\o}nm}^{(1)}(k_1\mathbf{r})\mathbf{N}_{\substack{e\\o}nm}^{(1)}(k_1\mathbf{r}') \right]
\end{aligned}
\tag{D.4}
$$

$$
\begin{aligned}
\bar{\bar{\mathbf{G}}}_{3s}^{(21)}(\mathbf{r},\mathbf{r}') = {} & \frac{ik_1}{4\pi}\sum_{n=1}^{\infty}\sum_{m=0}^{n}(2-\delta_0)\frac{2n+1}{n(n+1)}\frac{(n-m)!}{(n+m)!} \\
& \times \left[C_n \mathbf{M}_{\substack{e\\o}nm}(k_2\mathbf{r})\mathbf{M}_{\substack{e\\o}nm}^{(1)}(k_1\mathbf{r}') + D_n \mathbf{N}_{\substack{e\\o}nm}(k_2\mathbf{r})\mathbf{N}_{\substack{e\\o}nm}^{(1)}(k_1\mathbf{r}') \right]
\end{aligned}
\tag{D.5}
$$

$$
\begin{aligned}
\bar{\bar{\mathbf{G}}}_{3s}^{(11)}(\mathbf{r},\mathbf{r}') = {} & \frac{ik_1}{4\pi}\sum_{n=1}^{\infty}\sum_{m=0}^{n}(2-\delta_0)\frac{2n+1}{n(n+1)}\frac{(n-m)!}{(n+m)!} \\
& \times \left[E_n \mathbf{M}_{\substack{e\\o}nm}^{(1)}(k_2\mathbf{r})\mathbf{M}_{\substack{e\\o}nm}^{(1)}(k_1\mathbf{r}') + F_n \mathbf{N}_{\substack{e\\o}nm}^{(1)}(k_2\mathbf{r})\mathbf{N}_{\substack{e\\o}nm}^{(1)}(k_1\mathbf{r}') \right]
\end{aligned}
\tag{D.6}
$$

$$
\begin{aligned}
\bar{\bar{\mathbf{G}}}_{3s}^{(31)}(\mathbf{r},\mathbf{r}') = {} & \frac{ik_1}{4\pi}\sum_{n=1}^{\infty}\sum_{m=0}^{n}(2-\delta_0)\frac{2n+1}{n(n+1)}\frac{(n-m)!}{(n+m)!} \\
& \times \left[K_n \mathbf{M}_{\substack{e\\o}nm}(k_1\mathbf{r})\mathbf{M}_{\substack{e\\o}nm}^{(1)}(k_3\mathbf{r}') + L_n \mathbf{N}_{\substack{e\\o}nm}(k_3\mathbf{r})\mathbf{N}_{\substack{e\\o}nm}^{(1)}(k_1\mathbf{r}') \right]
\end{aligned}
\tag{D.7}
$$

Note that in all equations, the radial dependence of $\mathbf{r}'$ is expressed in terms of spherical Hankel functions because the source is located in the outmost layer. On the other hand, the radial functions involving $\mathbf{r}$ should be chosen appropriately for each layer. For $\bar{\bar{\mathbf{G}}}_{3s}^{(11)}(\mathbf{r},\mathbf{r}')$, which represents the scattered field, the spherical Hankel functions have

been used to satisfy the radiation condition; whereas for $\bar{\bar{\mathbf{G}}}_{3s}^{(31)}(\mathbf{r},\mathbf{r}')$ the spherical Bessel functions must be chosen to avoid having singularity in the origin. The eight scalar coefficients (A_n, B_n, C_n, D_n, E_n, F_n, K_n, L_n)appearing in (D.4)-(D.7) can be determined using the boundary conditions on the surfaces $r=a$ and $r=b$. The well-known boundary conditions

$$\hat{n}\times\mathbf{E}_1 = \hat{n}\times\mathbf{E}_2 \tag{D.8}$$

and

$$\hat{n}\times\mathbf{H}_1 = \hat{n}\times\mathbf{H}_2 \Rightarrow \frac{1}{\mu_1}\hat{n}\times\nabla\times\mathbf{E}_1 = \frac{1}{\mu_2}\hat{n}\times\nabla\times\mathbf{E}_2 \tag{D.9}$$

can be expressed in terms of the dyadic Green's functions as

$$\hat{r}\times\bar{\bar{\mathbf{G}}}_3^{(11)}(\mathbf{r},\mathbf{r}') = \hat{r}\times\bar{\bar{\mathbf{G}}}_3^{(21)}(\mathbf{r},\mathbf{r}') \qquad r=a \tag{D.10}$$

$$\frac{1}{\mu_1}\hat{r}\times\nabla\times\bar{\bar{\mathbf{G}}}_3^{(11)}(\mathbf{r},\mathbf{r}') = \frac{1}{\mu_2}\hat{r}\times\nabla\times\bar{\bar{\mathbf{G}}}_3^{(21)}(\mathbf{r},\mathbf{r}') \qquad r=a \tag{D.11}$$

$$\hat{r}\times\bar{\bar{\mathbf{G}}}_3^{(21)}(\mathbf{r},\mathbf{r}') = \hat{r}\times\bar{\bar{\mathbf{G}}}_3^{(31)}(\mathbf{r},\mathbf{r}') \qquad r=b \tag{D.12}$$

$$\frac{1}{\mu_2}\hat{r}\times\nabla\times\bar{\bar{\mathbf{G}}}_3^{(21)}(\mathbf{r},\mathbf{r}') = \frac{1}{\mu_3}\hat{r}\times\nabla\times\bar{\bar{\mathbf{G}}}_3^{(31)}(\mathbf{r},\mathbf{r}') \qquad r=b \tag{D.13}$$

From these equations eight algebraic equations can be formed in order to determine the eight unknown coefficients:

$$j_n(k_1a) + A_n h_n^{(1)}(k_1a) = C_n j_n(k_2a) + E_n h_n^{(1)}(k_2a) \tag{D.14}$$

$$\frac{k_1}{\mu_1}\left\{ \frac{1}{k_1a}\frac{\partial}{\partial r}\left[rj_n(k_1r)\right]\bigg|_{r=a} + \frac{A_n}{k_1a}\frac{\partial}{\partial r}\left[rh_n^{(1)}(k_1r)\right]\bigg|_{r=a} \right\} = $$
$$\frac{k_2}{\mu_2}\left\{ \frac{C_n}{k_2a}\frac{\partial}{\partial r}\left[rj_n(k_2r)\right]\bigg|_{r=a} + \frac{E_n}{k_2a}\frac{\partial}{\partial r}\left[rh_n^{(1)}(k_2r)\right]\bigg|_{r=a} \right\} \tag{D.15}$$

$$\left\{ \frac{1}{k_1 a} \frac{\partial}{\partial r} \left[r j_n(k_1 r) \right] \Big|_{r=a} + \frac{B_n}{k_1 a} \frac{\partial}{\partial r} \left[r h_n^{(1)}(k_1 r) \right] \Big|_{r=a} \right\} =$$

$$\left\{ \frac{D_n}{k_2 a} \frac{\partial}{\partial r} \left[r j_n(k_2 r) \right] \Big|_{r=a} + \frac{F_n}{k_2 a} \frac{\partial}{\partial r} \left[r h_n^{(1)}(k_2 r) \right] \Big|_{r=a} \right\}$$

(D.16)

$$\frac{k_1}{\mu_1} \left[j_n(k_1 a) + B_n h_n^{(1)}(k_1 a) \right] = \frac{k_1}{\mu_1} \left[D_n j_n(k_2 a) + F_n h_n^{(1)}(k_2 a) \right]$$

(D.17)

$$C_n j_n(k_2 b) + E_n h_n^{(1)}(k_2 b) = K_n j_n(k_3 b)$$

(D.18)

$$\frac{k_2}{\mu_2} \left\{ \frac{C_n}{k_2 b} \frac{\partial}{\partial r} \left[r j_n(k_2 r) \right] \Big|_{r=b} + \frac{E_n}{k_2 b} \frac{\partial}{\partial r} \left[r h_n^{(1)}(k_2 r) \right] \Big|_{r=b} \right\} = \frac{k_3}{\mu_3} \frac{K_n}{k_3 b} \frac{\partial}{\partial r} \left[r j_n(k_3 r) \right] \Big|_{r=b}$$

(D.19)

$$\frac{D_n}{k_2 b} \frac{\partial}{\partial r} \left[r j_n(k_2 r) \right] \Big|_{r=b} + \frac{F_n}{k_2 b} \frac{\partial}{\partial r} \left[r h_n^{(1)}(k_2 r) \right] \Big|_{r=b} = \frac{L_n}{k_3 b} \frac{\partial}{\partial r} \left[r j_n(k_3 r) \right] \Big|_{r=b}$$

(D.20)

$$\frac{k_2}{\mu_2} \left[D_n j_n(k_2 b) + F_n h_n^{(1)}(k_2 b) \right] = \frac{k_3}{\mu_3} L_n j_n(k_3 b)$$

(D.21)

The coefficients can be determined by solving the linear equation system of (D.14)-(D.21). After formulating the dyadic Green's functions, one can easily obtain the electric field in each layer, by following the procedure outlined in (3.39)-(3.44) in a straightforward manner. First, replacing $\bar{\bar{\mathbf{G}}}_0^{eo}(\mathbf{r},\mathbf{r}')$ with $\bar{\bar{\mathbf{G}}}_{3s}^{(11)}(\mathbf{r},\mathbf{r}')$ in the integral defined in (3.40) yields the scattered field outside the sphere as

$$\mathbf{E}^s(\mathbf{r}) = \frac{-k_1 \omega \mu_1 C_0}{4\pi} \sum_{n=1}^{\infty} \frac{2n+1}{n(n+1)} \left\{ A_n h_n^{(1)}(k_1 z_d) \mathbf{M}_{on1}^{(1)}(k_1 \mathbf{r}) \right.$$

$$\left. + \frac{B_n}{k_1 z_d} \frac{d}{dr'} \left(r' h_n^{(1)}(k_1 r') \right) \Big|_{r'=z_d} \mathbf{N}_{en1}^{(1)}(k_1 \mathbf{r}) \right\} \qquad r > a$$

(C.22)

Note that the expression has a similar form to $\mathbf{E}^i(\mathbf{r})$ defined in (3.44). The main difference is the form of radial functions, which are necessarily altered to satisfy the radiation condition at infinity. The field expressions in the remaining layers can be

obtained in a similar manner. For the inner layer of the sphere, the final form of the total electric field is determined as sphere as

$$
\begin{aligned}
\mathbf{E}(\mathbf{r}) = \frac{-k_1 \omega \mu_1 C_0}{4\pi} \sum_{n=1}^{\infty} \frac{2n+1}{n(n+1)} \Big\{ & K_n h_n^{(1)}(k_1 z_d) \mathbf{M}_{on1}(k_3 \mathbf{r}) \\
& + \frac{L_n}{k_1 z_d} \frac{d}{dr'} \Big(r' h_n^{(1)}(k_1 r') \Big) \Big|_{r'=z_d} \mathbf{N}_{en1}(k_3 \mathbf{r}) \Big\} \qquad r < b
\end{aligned}
\tag{D.23}
$$

Finally, the total electric field in the outer layer of the sphere:

$$
\begin{aligned}
\mathbf{E}(\mathbf{r}) = \frac{-k_1 \omega \mu_1 C_0}{4\pi} \sum_{n=1}^{\infty} \frac{2n+1}{n(n+1)} \Big\{ & C_n h_n^{(1)}(k_1 z_d) \mathbf{M}_{on1}(k_2 \mathbf{r}) + E_n h_n^{(1)}(k_1 z_d) \mathbf{M}_{on1}^{(1)}(k_2 \mathbf{r}) \\
& + \frac{D_n}{k_1 z_d} \frac{d}{dr'} \Big(r' h_n^{(1)}(k_1 r') \Big) \Big|_{r'=z_d} \mathbf{N}_{en1}(k_2 \mathbf{r}) + \frac{F_n}{k_1 z_d} \frac{d}{dr'} \Big(r' h_n^{(1)}(k_1 r') \Big) \Big|_{r'=z_d} \mathbf{N}_{en1}^{(1)}(k_2 \mathbf{r}) \Big\}
\end{aligned}
\tag{D.24}
$$

APPENDIX E: Method of moments solution for the scattered electromagnetic field

The MoM solution for 3-D electromagnetic scattering problem is developed and presented in [14]. In Appendix B, the same solution was adapted to the acoustic case. Here, we will present the formulation for the electromagnetic problem without explaining the derivation procedure. The detailed demonstration of the method and the derivation of the equations can be found in [14].

Unlike the acoustic case, the electromagnetic problem is a vectorial one. Therefore, for a scatterer which is discretized into N cubic cells, the number of knowns, namely the vectorial components ($3N \times 1$) of the interior electric field, is $3N$. Accordingly, the principal equation of the MoM solution, (C.2) in the acoustic case, becomes

$$\left(I - K\right)^{-1} E^i = E \tag{E.1}$$

where E^i and E are $3N \times 1$ matrices, whose elements are the vectorial components (E_x, E_y, E_z) of the incident electric field and the total electric field at the cell centers respectively. Accordingly, the coefficient matrix K becomes a $3N \times 3N$ matrix for the electromagnetic case.

The derivation of the elements of the coefficient matrix is based on the results presented in Appendix C for the acoustic case. Since the free space dyadic Green's function is defined in term of the scalar Green's function as

$$\bar{\bar{\mathbf{G}}}_0(\mathbf{r}, \mathbf{r}') = \left[\bar{\bar{I}} + \frac{1}{k^2} \nabla\nabla\right] g(\mathbf{r}, \mathbf{r}'), \tag{E.2}$$

the expressions of its nine scalar components can be formed using $g(\mathbf{r}, \mathbf{r}')$:

$$\bar{\bar{\mathbf{G}}}_o^{pq}(\mathbf{r}, \mathbf{r}') = i\omega\mu_0 (\delta_{pq} + \frac{1}{k_0^2} \frac{\partial^2}{\partial'_p \partial'_q}) g(\mathbf{r}, \mathbf{r}') \qquad p, q = 1, 2, 3. \tag{E.3}$$

Similar to (C.3), the elements of the matrix K are formulated as

$$K_{mn}^{pq} = k_0^2 v(r_n) \int_{\tau_n} \bar{\bar{\mathbf{G}}}_o^{pq}(\mathbf{r},\mathbf{r}') \, dv' \bigg|_{\mathbf{r}=r_m, \mathbf{r}'=r_n}$$

(E.4)

Taking (E.3) into account, it is clear that the result of the integral in (E.4) can be derived via the integration of $g(\mathbf{r},\mathbf{r}')$, given in (C.9) and (C.11) for singular cells and non-singular cells respectively. Therefore, the elements of the coefficient matrix K can be stated for the singular cells:

$$K_{mn}^{pq} = \begin{cases} 0 & m=n, p \neq q \\ k_0^2 v(r_n)\left(\dfrac{1}{3}\left[2(1-ik_0 a)e^{ik_0 a}-3\right]\right) & m=n, p=q \end{cases}$$

(E.5)

and for non-singular cells:

$$\begin{aligned} K_{mn}^{pq} = k_0^2 v(r_n) C^3 \bigg\{ &\frac{1}{k_0^2}\frac{e^{ikr}}{4\pi}\frac{-k^2 R^2 - 3ikR + 3}{R^5} \\ &\times (x_p^m - x_p^n)(x_q^m - x_q^n) + \frac{e^{ikR}}{4\pi R} \bigg\} \qquad m \neq n, p \neq q \end{aligned}$$

(E.6)

$$\begin{aligned} K_{mn}^{pq} = k_0^2 v(r_n) C^3 \bigg\{ &\frac{1}{k_0^2}\frac{e^{ikr}}{4\pi}\frac{ikR-1}{R^3} - (x_p^m - x_p^n)^2 \\ &\times \left[\frac{-3ik}{R^4} + \frac{3}{R^5} - \frac{k^2}{R^3}\right] + \frac{e^{ikR}}{4\pi R} \bigg\} \qquad m \neq n, p = q \end{aligned}$$

(E.7)

where C^3 is a scalar coefficient defined as

$$C^3 = \frac{4\pi a_{eq}}{k_0^2}\left[\frac{\sin k_0 a_{eq}}{k_0 a_{eq}} - \cos k_0 a_{eq}\right]$$

(E.8)

and R is the the Euclidean distance between the centers of the cells m,n:

$$R = [(x_m - x_n)^2 + (y_m - y_n)^2 + (z_m - z_n)^2]^{1/2}$$

(E.9)

CURRICULUM VITAE

Name Surname: Egemen Bilgin

Place and Date of Birth: Istanbul - 29.07.1984

E-Mail: bilgineg@itu.edu.tr

EDUCATION:

B.Sc.: Istanbul Technical University – Electronics and Communications Eng. (2008)

M.Sc.: Istanbul Technical University – Electronics and Communications Eng. (2010)

PUBLICATIONS, PRESENTATIONS AND PATENTS ON THE THESIS:

▪ **Bilgin, E.,** Yapar A. and Yelkenci, T., "An acoustic inverse scattering problem for spheres with radially inhomogeneous compressibility," *J. Acoust. Soc. Am.*, vol. 133, no. 4, pp. 2097-2104, Apr. 2013.

▪ **Bilgin, E.** and Yapar A., "Electromagnetic scattering by radially inhomogeneous dielectric spheres," *IEEE Trans. Antennas Propag.*, vol. 63, no. 6, pp. 2677-2985, June 2015.

▪ **Bilgin, E.** and Yapar A., "A Newton type 1-D profile reconstruction method for radially inhomogeneous dielectric spheres," *Inverse Problems in Science and Engineering*, (Under Review).

OTHER PUBLICATIONS, PRESENTATIONS AND PATENTS :

▪ **Bilgin E.,** Yapar A.: Detection of Three Dimensional Objects Buried in a Half-space by the Use of Surface Impedance. *PIERS Proceedings 1852-1855, August 18-21, Moscow 2009*

▪ **Bilgin E.,** Yapar A.: An Acoustic Inverse Scattering Problem for Spherical Coating Materials with Radially Inhomogeneous Profile. *PIERS Proceedings 725-729, August 12-15, Stockholm 2013*

▪ **Bilgin E.,** Aygün A., Yapar A., Akduman İ.: Analysis of Matching Media Effect on Microwave Brain Stroke Imaging via a Spherically Symmetrical Head Model. *PIERS Proceedings 452-456, July 6-9, Prague 2015*